

**DESIGN OF A PIEZORESISTIVE PRESSURE SENSOR USING  
TOPOLOGY OPTIMIZATION**

by  
ECE NAZ ERÜLKER

Submitted to the Graduate School of Engineering and Natural Sciences  
in partial fulfilment of  
the requirements for the degree of Master of Science

Sabancı University  
July 2024

**DESIGN OF A PIEZORESISTIVE PRESSURE SENSOR USING  
TOPOLOGY OPTIMIZATION**

Approved by:

Assoc. Prof. Dr. Güllü Kızıldağ Şendur .....  
(Thesis Supervisor)

Assoc. Prof. Dr. Bekir Bediz .....

Prof. Dr. Çetin Yılmaz .....

Date of Approval: July 24, 2024

ECE NAZ ERÜLKER 2024 ©

All Rights Reserved

## ABSTRACT

### DESIGN OF A PIEZORESISTIVE PRESSURE SENSOR USING TOPOLOGY OPTIMIZATION

ECE NAZ ERÜLKER

MECHATRONICS ENGINEERING M.A. THESIS, JULY 2024

Thesis Supervisor: Assoc. Prof. Dr. Güllü Kızıldağ Şendur

Keywords: Homogenization, modified SIMP, piezoresistive pressure sensor,  
topology optimization, TPMS

Flexible pressure sensors are used commonly in applications ranging from smart personal equipment to medical devices. Different applications require sensors designed specific to the application. In this thesis, a piezoresistive pressure sensor is designed via topology optimization for bedsores prevention (most sensitive at 4.6 kPa). The main objective is to develop a TO design framework for designing a sensor with maximum sensitivity, i.e. change in relative resistance over pressure. TO has been applied to many applications including mechanical, thermal, electromagnetic and piezoelectric devices. Although conductive material topologies have been designed for thermal or electric applications including use of TPMS structures, piezoresistive material design based TO has not been much explored. Here, we develop a TO framework based on modified SIMP material models constructed using numerical homogenization of piezoresistive gyroid unit cells. These material models are used during optimization and are needed during the reconstruction phase of the tapered gyroid sensor topology. The sensor design was envisioned as a PDMS-Polypyrrole composite material and its properties were taken from earlier measurements. A sheet type gyroid geometry is chosen due to its advantages such as volume fraction tunability that is easily linked to density based TO and its manufacturability using additive manufacturing. Simulation models were built and analyzed using FEM in COMSOL Multiphysics 6.2 and the TO framework was applied to three different design categories targeting: 1) mechanical performance, 2) electrical performance, and 3), both criteria simultaneously via multi-criteria design studies. CAD models were generated by a MATLAB script.

## ÖZET

### TOPOLOJİ OPTİMİZASYONU İLE PİEZOREZİSTİF BASINÇ SENSÖRÜ TASARIMI

ECE NAZ ERÜLKER

MEKATRONİK MÜHENDİSLİĞİ YÜKSEK LİSANS TEZİ, TEMMUZ 2024

Tez Danışmanı: Doç. Dr. Güllü Kızıldağ Şendur

Anahtar Kelimeler: homogenizasyon, modifiye SIMP, piezorezistif basınç sensörü,  
topoloji optimizasyonu, TPMS

Esnek basınç sensörleri, akıllı kişisel ekipmanlardan tıbbi cihazlara kadar çeşitli uygulamalarda yaygın olarak kullanılmaktadır. Farklı uygulamalar, uygulamaya özel tasarlanmış sensörler gerektirir. Bu tezde, bası yaralarının önlenmesi için topoloji optimizasyonu (TO) yoluyla bir piezorezistif basınç sensörü tasarlanmıştır (4,6 kPa basınç değerinde). Temel amaç, azami hassasiyete, yani azami basınç üzerindeki bağıl dirençteki değişime sahip bir sensör tasarlamak üzere bir TO tasarım çerçevesi geliştirmektir. Topoloji optimizasyonu, mekanik, termal, elektromanyetik ve piezoelektrik cihazların tasarımına uygulanmıştır. İletken malzeme odaklı tasarımlar, TPMS geometrileri de dahil olmak üzere farklı termal ve elektrik uygulamalara yönelik çalışılmış olsa da, piezorezistif malzeme tasarımına dayalı TO problemi çok fazla araştırılmamıştır. Bu çalışmada, piezorezistif jiroid birim hücrelerinin sayısal homojenizasyonu kullanılarak oluşturulan modifiye SIMP malzeme modelleri kullanılarak bir TO çerçevesi geliştirilmektedir. Geliştirilen malzeme modelleri, hem optimizasyon sırasında hem de değişken jiroid sensör topolojisinin yeniden yapılandırılması aşamasında gereklidir. Sensör tasarımının malzeme yapısı PDMS-PPy kompozit olarak öngörülmüş ve gerekli özellikleri önceki bir çalışmadan alınmıştır. Tezde kabuk tipi bir jiroid geometrisi, hacim oranının kolay ayarlanabilirliği sayesinde yoğunluğa dayalı TO ile uyumludur ve 3 boyutlu basım teknikleri kullanılarak üretilebilirliği gibi avantajları nedeniyle seçilmiştir. Simülasyon modelleri COMSOL Multiphysics 6.2'de sonlu elemanlar yöntemi kullanılarak analiz edilmiş ve TO çerçevesi üç farklı hedefe yönelik tasarım kategorisin-

deki problemlere uygulanmıştır. Bunlar 1) mekanik performans, 2) elektriksel performans ve 3) çok kriterli tasarım modeli yoluyla her iki kriteri aynı anda hedefleyen tasarım problemleridir. Uygulama sırasında CAD modelleri bir MATLAB komut dosyası tarafından oluşturulmuştur.

## ACKNOWLEDGEMENTS

Firstly, I would like to sincerely thank Assoc. Prof. Dr. Güllü Kızıldaş Şendur, my thesis supervisor, for her invaluable guidance and support throughout the course of my M.Sc. research. I'm grateful that I worked with a supervisor who recognized my achievements more than I did. I also would like to extend my appreciation to my friends in our research group. I am thankful to Işıl for being a great lab partner, to Ata for tirelessly answering all the questions I send on his way, and especially to Mervenaz for her unwavering support and willingness to assist whenever help was needed. I also extend my appreciation to the rest of the group for their contributions.

I am profoundly grateful to TÜBİTAK for the financial support through the 2210-A BİDEB scholarship during my studies.

A special thanks to my partner Arca for always being there for me and trying to listen to me get excited about my "blocks" even if the topic wasn't particularly interesting to them. I appreciate all the times you picked me up, and all the color and fun you brought into my life.

I want to thank my family for their unconditional love and support, for their interest in what I do, and being patient with me. I feel grateful everyday that I have the best family I could hope for.

Finally, I would like to thank all my dear friends who supported me along the way.

This study was funded by the Scientific and Technological Research Council of Turkey (TÜBİTAK) 1004 research project LIGNONANO *Lignin Bazlı Tıbbi Etkin Maddeler ve Formülasyonlar Geliştirilmesi* support program (Project #:22AG04).

*Dedicated to my family*

## TABLE OF CONTENTS

<b>LIST OF TABLES</b> .....	<b>xi</b>
<b>LIST OF FIGURES</b> .....	<b>xiii</b>
<b>LIST OF ABBREVIATIONS</b> .....	<b>xvii</b>
<b>LIST OF SYMBOLS</b> .....	<b>xvii</b>
<b>1. INTRODUCTION</b> .....	<b>1</b>
1.1. Motivation .....	1
1.2. Literature Review .....	3
1.2.1. Piezoresistive Sensors .....	3
1.2.2. Sensor Design and Topology Optimization.....	6
1.3. Goals and Contributions .....	9
<b>2. Background</b> .....	<b>11</b>
2.1. Piezoresistive Pressure Sensors .....	11
2.2. Lattices and the modified SIMP Law .....	14
2.3. Homogenization of Elasticity, Initial Conductivity and Elastoresistivity	15
2.3.1. Elasticity and Initial Conductivity Homogenization .....	16
2.3.2. Elastoresistivity Homogenization .....	20
2.4. Fabrication of Piezoresistive Pressure Sensors .....	22
2.5. Topology Optimization and SIMP Models.....	23
2.6. Geometric Modeling of the Gyroid Unit Cell .....	25
<b>3. METHODOLOGY</b> .....	<b>28</b>
3.1. Derivation of modified SIMP Models using Homogenization .....	29
3.1.1. Homogenization of Effective Young's Modulus and its Validation	30
3.1.2. Homogenization of Initial Conductivity and its Validation ....	34
3.1.3. Homogenization of Elastoresistivity Component and Its Vali- dation .....	36

3.2. Topology Optimization .....	39
3.2.1. Common Properties of the Optimization Models .....	40
3.2.2. Design Framework for Solid Mechanics Based Topology Optimization .....	41
3.2.3. Design Framework for Electrical Conductivity Based Topology Optimization .....	43
3.2.4. Design Framework for Piezoresistivity based Multi-Criteria Topology Optimization .....	46
<b>4. Results and Discussion .....</b>	<b>50</b>
4.1. Results of Homogenization Models and Validations .....	51
4.1.1. SIMP Model and Validation of Young's Modulus .....	51
4.1.2. SIMP Model and Validation of Initial Conductivity .....	54
4.1.3. SIMP Model and Validation of Elastoresistivity .....	58
4.2. Solid Mechanics Based TO: Minimum Compliance of a Compression Cube .....	61
4.3. Electrical Conductivity Based TO Targeting Maximum Sensitivity ..	64
4.3.1. Case Study 1 With Objective: Minimum Potential Difference .	65
4.3.2. Case Study 2 and Case Study 3 with Objective of Relative Resistivity Change - Effect of BC .....	67
4.4. Piezoresistivity Based TO Targeting Maximum Sensitivity and Compliance: Multi-Criteria Optimization .....	71
4.5. Discussion.....	77
<b>5. CONCLUSION AND FUTURE WORK.....</b>	<b>79</b>
<b>BIBLIOGRAPHY.....</b>	<b>81</b>
<b>Appendices.....</b>	<b>85</b>
.1. Gyroid Implementation in COMSOL .....	85
.2. Comparison of Multi-Criteria Functions with Different Weights.....	88
.3. Simulation Statistics .....	89
.4. COMSOL Implementation of Material Properties and How They Relate to the Physics Interface .....	89

## LIST OF TABLES

Table 2.1. Form of the modified SIMP functions used for respective material properties .....	25
Table 3.1. Gyroid material properties: Young’s modulus homogenization .	31
Table 3.2. Homogenized cube material properties: Validation of Young’s modulus modified SIMP fit. ....	33
Table 3.3. Gyroid material properties: Initial conductivity homogenization	35
Table 3.4. Homogenized cube material properties: Validation of initial conductivity modified SIMP fit. ....	36
Table 3.5. Gyroid material properties: Elastoresistivity homogenization...	38
Table 3.6. Properties and objective functions of electrical conductivity based TO cases targeting maximum sensitivity.....	45
Table 3.7. Boundary conditions and objective functions of piezoresistivity based multi-criteria TO cases .....	47
Table 4.1. Homogenized Young’s modulus results of fitted modified SIMP function and comparison with calculated FE model value of gyroid unit cell .....	51
Table 4.2. Top surface z-displacement values of 3x3x3 gyroid unit cell (gyroid) vs. its equivalent homogenized cube model under 1 N load. .	53
Table 4.3. Homogenized initial conductivity results of fitted modified SIMP function and comparison with calculated FE model value of gyroid unit cell under 1V electrical load .....	55
Table 4.4. Top surface potential values $\Phi(V)$ of 3x3x3 gyroid unit cell (gyroid) vs. its equivalent homogenized cube model under $1A/m^2$ current density load.....	57
Table 4.5. Homogenized elastoresistivity results: Effective normalized elastoresistivity, $m^*$ , unscaled elastoresistivity, $m$ , calculated based on related electrical response parameters: initial conductivity under no loading $\sigma_{latt,0}$ and under unit strain, $\sigma_{latt,F}$ for different volume fractions, VF .....	59

Table 4.6. Effective current density $J^*$ on the bottom plane of single gyroid unit cell with symmetry vs. its equivalent homogenized cube model under 1V potential and 4666 Pa loading .....	60
Table 4.7. Properties and results of electrical conductivity based TO cases targeting maximum sensitivity.....	65
Table 4.8. Properties and results of PR based TO cases targeting maximum sensitivity and compliance via multi-criteria optimization.....	71
Table 1. Optimization with respect to electrical objective function .....	88
Table 2. Simulation statistics for 1x1x1 sheet gyroid.....	89
Table 3. Simulation statistics for 3x3x3 sheet gyroid.....	89

## LIST OF FIGURES

Figure 1.1. Types of flexible pressure sensors (Tang, Lu, Liu, Yan, Du, Zhang, Zhou & Fu, 2021) .....	4
Figure 2.1. Working mechanism of different types of nanocomposite pressure sensors: (A) Piezoresistivity (B) Capacitive (C) Piezoelectricity (D) Triboelectricity (Tang et al., 2021) .....	12
Figure 2.2. Boundary conditions and area definitions properties used in numerical homogenization models and validation studies.....	18
Figure 2.3. Fabrication steps of a TPMS sensor using lost mold technique based on (Erulker, Ece, Ekicioglu, Can, Kiziltas Sendur & Ince, 2022)	24
Figure 3.1. Developed design scheme for design optimization of functionally graded cellular structures (FGCS) applied to PR sensors .....	28
Figure 3.2. Boundary Conditions applied for the Young’s Modulus homogenization of a gyroid shown for a unit cell with 0.5 relative density	30
Figure 3.3. Mesh used for numerical homogenization of a gyroid unit cell and its homogeneous cubic counterpart model used for the validation of homogenization .....	32
Figure 3.4. Boundary conditions of repeated gyroid (left) and cube (right) models used for Homogenized Young’s Modulus validation .....	33
Figure 3.5. Boundary Conditions applied for the initial conductivity homogenization of a gyroid shown for a unit cell with 0.5 relative density	34
Figure 3.6. Boundary conditions of repeated gyroid (left) and cube (right) models used for Homogenized initial conductivity validation .....	36
Figure 3.7. Boundary loading conditions of repeated gyroid (left) and cube (right) models used for homogenized elastoresistivity, $m$ , validation...	38
Figure 3.8. Expression and surface used in COMSOL for the effective final conductivity $\sigma_f$ extraction of a gyroid unit cell model used for validation of the homogenized elastoresistivity, $m$ . .....	39
Figure 3.9. Mesh used in all Topology optimization case studies.....	41

Figure 3.10. Design Flowchart of Solid Mechanics Based Topology Optimization .....	42
Figure 3.11. Boundary conditions applied on design domain used for solid mechanics based TO case study targeting minimum compliance .....	43
Figure 3.12. Design Flowchart used for Electrical Conductivity based Topology Optimization Studies .....	44
Figure 3.13. Boundary Conditions applied on design domain used for electrical conductivity based TO case study 1 and 3 (left) and case study 2 (right).....	45
Figure 3.14. Design Flowchart for Piezoresistivity Based Multi-Criteria Topology Optimization Studies .....	46
Figure 3.15. Boundary conditions applied on the design domain used for multi-criteria based TO case study 4 (left) and case study 5 (right) ..	47
Figure 3.16. Screenshot of objective function definitions in the multi-criteria based TO case studies using global objective feature of the general optimization module in COMSOL. ....	48
Figure 3.17. Screenshot of optimization Settings used in the multi-criteria based TO case studies using global objective feature of the general optimization module in COMSOL. ....	48
Figure 3.18. Screenshot of the weighted multi-criteria function definition in the multi-criteria based TO case studies using the integral objective feature of the general optimization module in COMSOL. ....	49
Figure 4.1. Fitted modified SIMP function for Young’s modulus: normalized effective Young’s modulus vs. relative density under 1% strain. . .	52
Figure 4.2. Validation results of homogenized Young’s modulus: Displacement (y axis) of 3x3x3 gyroid unit cell with different relative density (x axis) vs. homogenized cube with fitted Young’s modulus value under 1 N load. ....	53
Figure 4.3. Validation of homogenized Young’s modulus: displacement distribution (mm) response of 3x3x3 gyroid unit cell (left) and its equivalent homogenized cube (right) under 1N load . ....	54
Figure 4.4. Screenshot of the MATLAB’s curve fitting application used for the construction of the modified SIMP model, shown for conductivity $\sigma$	55
Figure 4.5. Fitted modified SIMP function for initial conductivity: normalized effective initial conductivity (y-axis) vs. relative density (x-axis).....	56

Figure 4.6. Validation of homogenized initial conductivity: Average potential (y axis) of repeated gyroid model with different relative density (x axis) vs. homogenized cube with fitted initial conductivity value...	57
Figure 4.7. Validation of homogenized initial conductivity:electric potential (V) response of 3x3x3 gyroid unit cell (left) and its equivalent homogenized cube under $1A/m^2$ current density load(right). ....	58
Figure 4.8. Fitted modified SIMP function for elastoresistivity component: effective elastoresistivity component magnitude (y-axis) vs. relative density (x-axis) .....	60
Figure 4.9. Validation of homogenized elastoresistivity component: Current density (y axis) of repeated gyroid model with different relative density (x axis) vs. homogenized cube with fitted elastoresistivity component value. ....	61
Figure 4.10. Design results given by Saadlaoui, Milan, Rossi & Chabrand (2017) for the minimization of compliance problem of a compression cube.....	62
Figure 4.11. Design results obtained for the minimization of compliance problem of a compression cube: displacement (top left), Young's modulus (top right), strain energy density (lower left) and resistivity change in z direction (lower right). Units are shown in corresponding colour bars .....	63
Figure 4.12. Density distribution obtained for the minimization of compliance problem of a compression cube: volumetric distribution (left) vs. cross sectional plot (right) .....	63
Figure 4.13. Solid based TO case studies 2 and 3 targeting maximum sensitivity: Convergence of objective value (blue), average volume constraint (green).....	64
Figure 4.14. Design results obtained for TO design case study 1: relative density (top left), displacement (top center), electrical potential (top right), current density (bottom left), initial conductivity (bottom center), and change in resistivity (bottom right). Units are shown in corresponding colour bars .....	66
Figure 4.15. Convergence history of objective function and VF constraint of TO case study 1.....	67
Figure 4.16. Electrical based TO case studies 2 and 3 targeting maximum sensitivity: Convergence of objective value (blue), average volume constraint (green). ....	68

Figure 4.17. Design results obtained for electrical TO design case 2: relative density (top left), displacement (top center), electrical potential (top right), current density (bottom left), initial conductivity (bottom center), and change in resistivity (bottom right). Units are shown in corresponding colour bars.....	69
Figure 4.18. Density distribution obtained for the minimization of electrical TO design case 2: volumetric distribution (left) vs. cross sectional plot on xy plane (center) and cross sectional plot on xz plane (right)	69
Figure 4.19. Design results obtained for electrical TO design case 3: relative density (top left), displacement (top center), electrical potential (top right), current density (bottom left), initial conductivity (bottom center), and change in resistivity (bottom right). Units are shown in corresponding colour bars. ....	70
Figure 4.20. Density distribution obtained for the the minimization of electrical TO design case 3: volumetric distribution (left) vs. cross sectional plot on xy plane (center) and cross sectional plot on xz plane (right).....	70
Figure 4.21. Design results obtained for PR based TO design case 4: relative density (top left), displacement (top center), electrical potential (top right), current density (bottom left), initial conductivity (bottom center), and change in resistivity (bottom right). Units are shown in corresponding colour bars. ....	72
Figure 4.22. PR based TO case number 4 targeting maximum sensitivity and minimum compliance: Convergence of objective value (blue) and average volume constraint (green). ....	73
Figure 4.23. Design results obtained for PR based TO design case 5: relative density (top left), displacement (top center), electrical potential (top right), current density (bottom left), initial conductivity (bottom center), and change in resistivity (bottom right). Units are shown in corresponding colour bars. ....	74
Figure 4.24. Density distribution obtained for PR based TO case number 5 targeting maximum sensitivity and compliance (Case 5): volumetric distribution (left) vs. cross sectional plot on xy plane (center) and cross sectional plot on xz plane (right) s.....	75
Figure 4.25. PR based TO case number 5 targeting maximum sensitivity and minimum compliance: Convergence of multi-criteria objective value (blue), average volume constraint (green), compliance (red), and Total inverse relative change in resistivity (cyan). ....	75
Figure 4.26. Denser mesh with 8000 elements .....	76

Figure 4.27. Density distribution obtained for PR based TO case number 5 with a denser mesh targeting maximum sensitivity and compliance (Case 5): volumetric distribution (left) vs. cross sectional plot on xy plane (center) and cross sectional plot on xz plane (right) .....	77
Figure 1. Creating the CAD file in MATLAB in .STL format .....	85
Figure 2. Importing the STL file to COMSOL form Mesh Parts .....	85
Figure 3. Importing geometry under Geometry tab of Component and build .....	86
Figure 4. Defining the values to be extracted .....	86
Figure 5. Defining governing physics and boundary conditions .....	86
Figure 6. Tetrahedral meshing the geometry .....	87
Figure 7. Enabling the active physics and running the study .....	87
Figure 8. 0.5 weight on electrical and 0.5 weight on mechanical objective function .....	87
Figure 9. 0.6 weight on electrical and 0.4 weight on mechanical objective function .....	88
Figure 10. Linearelastic Material definition in COMSOL .....	90
Figure 11. Current Conservations, Piezoresistive definition in COMSOL .	90
Figure 12. Material Properties in COMSOL which are refereed in physics modules in Fig. 10 and Fig. 11 .....	91
Figure 13. Variables in COMSOL: Modified SIMP Formulas .....	91

## LIST OF ABBREVIATIONS

TO: Topology Optimization .....	1
TPMS: Triply Periodic Minimal Surface .....	1
AM: Additive Manufacturing .....	2
PR: Piezoresistive .....	2
FG: Functionally Graded .....	2
SIMP: Solid Isotropic Material with Penalization .....	2
FEM: Finite Element Method .....	2
PDMS: Polydimethylsiloxane .....	4
PPy: Polypyrrole .....	6
PDMS-PPy: Polydimethylsiloxane-Polypyrrole .....	6
FEA: Finite Element Analysis .....	7
PUCs: Periodic Unit Cells .....	15
AH: Asymptotic Homogenization .....	15
EBHM: Energy-based Homogenization Method .....	16
MMC: Moving Morphable component .....	24
HMTO: Homogenization-based TO .....	28
MMA: Method of Moving Asymptotes .....	41

## LIST OF SYMBOLS

<b>S</b>	Stress tensor (Pa)
<b>C</b>	Stiffness matrix
$\varepsilon$	Strain
<b>J</b>	Current density vector ( $J/m^2$ )
$\sigma$	Conductivity matrix ( $S/m$ )
<b>E</b>	Electric field vector ( $V/m$ )
$\Delta\rho$	Change in resistivity ( $\Omega m$ )
$\Pi$	Piezoresistance tensor ( $\Omega m/Pa$ )
<b>M</b>	Elastoresistance tensor ( $\Omega m$ )
$\rho_r$	Resistivity ( $\Omega m$ )
<b>R</b>	Resistance ( $\Omega$ )
$E^*$	Effective Young's modulus
$E_{latt}$	Young's modulus of the lattice structure (Pa)
$E_{sol}$	Young's modulus of the solid material (Pa)
$\rho$	Relative density, i.e. volume fraction
$\rho_{latt}$	Density of the lattice structure (Pa)
$\rho_{sol}$	Density of the solid material (Pa)
$E$	Young's modulus (Pa)
$F_{reac}$	Total Reaction force on a surface (N)

$A_{surf}$	Cross section area of the design space ( $m^2$ )
$\sigma_0$	Initial conductivity (S/m)
$(\sigma_0)_{sol}$	Initial conductivity of solid material ( $\Omega m$ )
$L$	Length of an edge of the design space (mm)
$m^*$	Normalized effective elastoresistivity component
$\Phi$	Electric potential (V)

# 1. INTRODUCTION

## 1.1 Motivation

Sensors have been around for many years since the popularity of semiconductors with a rapid growing interest in recent years as new applications and material technologies emerged with frequent use in our everyday life (Tang et al., 2021). As technology matured and the quest for miniature products increased, a particular class of sensors, namely flexible or conformal sensor design became an active research area. Flexible sensors are used for robotics, wearable accessories and clothes, and patient treatment in hospitals and houses including bedsores detection (Tang et al., 2021). Flexible pressure sensors in particular, are studied frequently since they constitute the basic unit used for applications ranging from pulse to body weight detection.

Different applications require the sensor to be optimized specifically for that application to increase their sensitivity. Hence, there is a need for flexible design methods to suit these applications. The design process doesn't only rely on the choice of the sensing mechanism and material, but also the structure and geometry of the sensor is important. An efficient way to incorporate the geometry or material distribution into the design process is to use topology optimization (TO). In TO, the structure is initially divided into design cells, and the density of the design cells are changed with respect to the objective function and constraints representing the design requirements of the device such as a sensor to mainly increase their sensitivity. Hence, there is a need for flexible and effective design methods to suit different design requirements for a wide range of applications. Towards this need, this thesis aims to develop a TO framework to optimize a 3D piezoresistive pressure sensor using graded triply periodic minimal surface (TPMS) structured unit cells, and apply this framework for bedsores prevention requirements.

TPMS unit cells have become popular due to their desired geometric features (Feng, Fu, Yao & He, 2022), suitability for homogenization-based TO designs and easy manufacturability using additive manufacturing (AM) (Modrek, Viswanath, Khan, Hassan Ali & Abu Al-Rub, 2023).

As regards the pressure sensing mechanism, most popular choices are piezoresistive, capacitive, piezoelectric and triboelectric (Tang et al., 2021). In this thesis, we present a design framework that concentrates on the design of a piezoresistive (PR) pressure sensor because of their advantages such as easy read-out mechanism and large working pressure range (Zang, Zhang, Di & Zhu, 2015) in addition to being scalable and their continuous input measuring abilities.

Out of the various sensor properties, its structural configuration stands out while designing the sensor. Moreover, many options ranging from 2D membranes (Chen, Zhu, Ma & Yuan, 2008; Rubio, Silva & Nishiwaki, 2008; Yamada, Hayamizu, Yamamoto, Yomogida, Izadi-Najafabadi, Futaba & Hata, 2011) to 3D complex lattice structures (Li, Dai, Tang, Dong & Zhao, 2019; Oh, Kim, Kim, Choi, Yang, Lee, Pyatykh, Kim, Sim & Park, 2019; Simsek, Gayir, Kiziltas & Sendur, 2020) have been proposed. Lattices are interconnected structures which makes them available for more accessible methods such as additive manufacturing. Among lattice structures, TPMS structures are a popular lattice type in the research community at the moment. TPMS structures are lattice structures with zero mean curvature, and as the name suggests, these structures are formed via a repetition of a unit cell. This means that it can be precisely defined by mathematical functions, replicated, and easily scaled (Feng et al., 2022).

In terms of the material property, controlling the amount of void in a unit cell, the user can manipulate the effective material properties of that cell, enabling a composite-like behavior possible within the same structure. Functionally graded (FG) lattice structures mapped to TO design results are an example of this (Simsek et al., 2020). In this study, we extend for the first time TO design using FG TPMS topologies to the design of PR sensors. An optimal density distribution is obtained via modified Solid Isotropic Material with Penalization (SIMP) models based on piezoresistive material homogenization and then mapped to a final graded TPMS topology that displays optimal sensor performance.

While there is extensive literature on the manufacturing of piezoresistive transducers, finite element modeling (FEM) specifically related to PR materials has been under investigation for only the last decade. Design via TO using FEM in very basic terms is to calculate the optimal arrangement of material within a given spatial domain to achieve the best response for an objective. In this thesis our main

objective is to optimize the sensor to increase its sensitivity.

It is fair to state that although there are studies on optimizing PR sensors, there aren't any that focus on their 3D designs. Most of the optimization models for PR materials are for 2D strain sensors.

In this thesis, we propose a TO framework based on numerical homogenization of PR gyroid unit cells. Since thermal and electrical conduction are analogical to each other, we relied on existing thermal 3D optimization studies focusing on planar PR optimization to build the backbone of the 3D piezoresistive topology optimization model. To the best of our knowledge, the design of 3D PR sensors using TO based on TPMS homogenization does not exist. More specifically, a PR pressure sensor is designed by using TO with modified SIMP material models for bedsores applications (most sensitive at 4666 Pa (Misaki, Imanishi, Takasugi, Wada, Fukagawa & Furue, 2014)).

## 1.2 Literature Review

### 1.2.1 Piezoresistive Sensors

Flexible pressure sensors can be classified with respect to their working mechanism, material and manufacturing methods (Tang et al., 2021). These classes are inherently correlated with each other such as for instance a certain mechanism requiring a certain type of material and fabrication method.

Also, these features are directly mapped to the three design criteria for a flexible pressure sensor that include: (1) working mechanism, (2) material choice, and (3) structural configuration and geometry.

As regards the pressure sensing mechanism, most popular choices are capacitive, piezoelectric and PR. Piezoelectric sensors can self-power but can only sense dynamic pressure while capacitive and PR can provide continuous monitoring while depending on a current source (Cui, Huang, Zhang, Song, Zheng, Chevali, Wang & Xu, 2022). Additionally, PR sensors are known to have an easy read-out mechanism, and large pressure range (Zang et al., 2015). In this thesis, for the chosen applica-

tion of bedsores detection, to supply a current source is expected to not constitute a problem, and the pressure is expected to be monitored continuously, therefore, a PR pressure sensing mechanism is chosen to be designed.

Figure 1.1 Types of flexible pressure sensors (Tang et al., 2021)



Regarding the material choice of the sensor, as it is earlier stated, it is interrelated to the other two design criteria, i.e. the mechanism and geometry. Earlier well known examples of PR pressure sensors are silicon-based MEMS sensors. Although still often preferred for planar applications, due to their brittle nature, Silicon is not widely used in flexible sensor applications (Chen et al., 2008).

With advances in composite materials, their use resulted in improved performance of flexible PR sensors significantly (Mitrakos, 2014). Composites are materials consisting of multiple components with differing physical and chemical properties, such as a nonconductive material via doping becoming conductive to display both flexibility and conductivity. This class of materials are called conductive filler-polymer nanocomposites. Yamada et al. (2011)'s work is an example using composite materials for PR sensors. Their sensor is a Polydimethylsiloxane(PDMS)-carbon nanotube composite designed to detect different types of human motion, including breathing and speech, movement, and typing.

The one-millimeter-thick sensor performs well as the gauge factor was calculated to be 0.82 (0 to 40% strain) while metal gauges have a factor of 2.0 (5% maximum strain) (Yamada et al., 2011). Thin sensors are usually more suitable for detecting tension. It can be seen in Yamada et al. (2011)'s paper that sensors are placed such that they are in-line with the stretched muscle. Hence it can be argued that 3D structures are more suitable for pressure detecting application. Additionally, 3D sensors create more surface for the conductive material, hence better sensitivity. In this thesis specifically, the sensor will be under body weight to detect bedsores, therefore the sensor should be designed to be under constant pressure.

Out of the three sensor design criteria, the structural configuration and in particular geometry of the sensor gives the user the most freedom in designing the sensor. As earlier stated, various geometrical configurations have been proposed mainly ranging from 2D membranes to 3D complex lattice structures (Chen et al., 2008; Li et al., 2019; Oh et al., 2019; Rubio et al., 2008; Simsek et al., 2020; Yamada et al., 2011).

More specifically, among 3D sensor geometries, some well known ones are spherical pores (Oh et al., 2019), pyramids (Khalili, Shen & Naguib, 2018), micro-domes (Zhang, Han, Hu, Xiong, Gu, Zhang, Zhu, Sun & Wong, 2020) and lattice structure (Modrek et al., 2023; Ye, Lin, Xiong, Wu, Zhao & Fang, 2019). Common purpose of the mentioned structures is to increase surface to volume ratio for better sensitivity. Out of these options, lattice structures stand out due to their repeatability and easier fabrication opportunities (Davoodi, Montazerian, Haghniaz, Rashidi, Ahadian, Sheikhi, Chen, Khademhosseini, Milani, Hoorfar & Toyserkani, 2020; Oh et al., 2019). Oh et al. (2019) studied the effect of uniform and random sized pores and showed uniformity is superior. In this study the pores are formed by microfluidic emulsion droplet self-assembly technique which is a complicated procedure. Lattices on the other hand, are interconnected structures which makes them available for more accessible methods such as additive manufacturing.

TPMS structures as earlier defined are lattice structures with zero mean curvature, and are formed via a repetition of a unit cell microstructures such as gyroid, diamond, Schwarz-P and IWP microstructures. They are favorable as their complex geometries can be precisely defined by mathematical functions, replicated, and easily scaled (Feng et al., 2022). Additionally, TPMS are known for high surface to volume ratio and highly interconnected porous architectures which makes them advantageous structures to use in sensor applications such as in this thesis. Studies such as those by Imanian, Kardan-Halvaei, Nasrollahi, Imanian, Montazerian & Nasrollahi (2023) and Davoodi et al. (2020) introduce 3D piezoresistive pressure sensors that utilize TPMS geometries where the geometries are of constant volume function

and are not a result of an optimization study. The sensor is a silicone rubber sensor with graphene nanoplatelet coating, therefore conduction occurs on the surfaces of the sensors. The ability to change the overall volume fraction throughout the volumetric space the sensor can occupy is shown to give the designer an additional dimension to tune the sensor performance leading to Functionally Graded (lattice) structures (FG(L)S). This ability is particularly suitable to be implemented using a TO formulation. In terms of the material property, controlling the amount of void in a unit cell, the user can manipulate the effective material properties of that cell, mathematically known as homogenization, enabling a composite-like behavior possible within the same structure. FG lattice structures mapped to TO design results exist for several applications including mechanical bandgap structures (Simsek et al., 2020), mechanical and thermal applications (Li et al., 2019; Modrek et al., 2023). In this thesis, we extend for the first time TO design using FG TPMS topologies to the design of piezoresistive pressure sensors. An optimal density distribution is obtained via modified SIMP models based on piezoresistive material homogenization and then mapped to a final graded TPMS topology that displays optimal sensor performance. Related studies on optimal design of PR pressure sensors and in particular the use of TO in PR sensor design is discussed in the next section.

### 1.2.2 Sensor Design and Topology Optimization

Design of a flexible sensor is divided into 3 parts:

- 1.1 Choice of mechanism
- 1.2 Choice of material
- 1.3 Choice of geometry

This thesis mainly concentrates on the third aspect by searching for the optimal geometry of the sensor formulated as a material distribution of a coated flexible material, to be solved via topology optimization. Nonetheless, the first two should not go unmentioned. As mentioned previously the sensor studied in this thesis uses PR to sense the change in pressure. Together with PR, choice of material is Polydimethylsiloxane-Polypyrrole (PDMS-PPy) composite. PDMS is the main bulk that provides elasticity for the sensor, while the PPy particles in the PDMS create paths to conduct electricity. There are several examples of composite polymer-conductor sensors in literature. but Oh et al. (2019)'s study of a highly uniform 3D porous pressure sensor presents a PDMS coated with PPy and demonstrates the

effectiveness of this material combination. Although the materials are the same, in this project a mixture of PDMS-PPy is studied while Oh et al. (2019) coats PDMS bulk with PPy. Choice of the geometry as explained in the previous section is a TPMS lattice, in particular a lattice with a sheet type gyroid unit cell geometry. In this subsection, state of art for optimization of piezoresistive pressure sensors will be provided after summarizing modeling efforts of sensors.

While there is extensive literature on the manufacturing of PR transducers, FEM specifically related to PR materials has been under investigation for only the last decade. Before FEM, researchers relied mostly on analytical techniques (Gridchin & Gridchin, 1997). Lumped circuit model and analytical formulation for modeling conducting polymers also exist (Kalantari, Dargahi, Kövecses, Mardasi & Nouri, 2012). Given that a material's piezoresistance coefficients can be either positive or negative, maximizing sensitivity involves increasing stress in certain directions while reducing it in others. This task is too complex for simple models with a limited number of degrees of freedom. Therefore, numerical studies using finite element analysis (FEA) have been conducted to determine optimal PR designs (Zhuang, Minami, Shiba & Yoshikawa, 2023).

Membrane and cantilever applications of PR sensors have existed longer than 3D applications, therefore most studies on design optimization including TO of sensors are based on 2D or cantilever beam models (Giusti, Mello & Silva, 2014; Mello, Takezawa & Silva, 2012; Pedersen, 2004). Pedersen (2004)'s cantilever bio-probe model with TO is one of the very first design examples of PR sensors. In this model, a PR area is attached to the fixed end of a cantilever. The cantilever itself is not piezoresistive but still, using TO on the cantilever beam will change the strain applied on the piezoresistive part and affect its sensitivity. This study is followed by Rubio et al. (2008) where again the PR material itself is not optimized but it introduces a generic TO formulation by using 2D FEM. Both of these studies use analytical methods to calculate and optimize sensitivity of a PR sensor using TO. Later Mello et al. (2012) implements a TO scheme for the design of plate-based or membrane based PR sensor, in which the PR material distribution is also optimized (Mello et al., 2012). They use a multiobjective optimization model with a weighted sum of sensitivity and mechanical compliance. Davoodi et al. (2020) have a follow-up study where they optimize a 3D flexible pressure sensor, but they apply shape optimization rather than TO which is known to limit design degrees of freedom and hence the resulting device performance. Design via TO in very basic terms is to calculate the optimal arrangement of material within a given spatial domain to achieve the best response for an objective. In this thesis, our main objective is to optimize the sensor to increase its sensitivity focusing on a 3D material distribution

problem.

It can be concluded that although there are studies on optimizing PR sensors, there aren't any that exploit the use of geometry and material in full 3D using TO for pressure sensors. As outlined above most of the optimization models for PR materials are for 2D strain sensors. An example of 3D PR sensor is Sixt, Davoodi, Salehian & Toyserkani (2023)'s study in which a Schwarz-P type piezoresistive vibration sensor is designed. For this design, size optimization is used, i.e. parameters that dictate the object's size are determined. Moreover, the most desired metric of sensitivity of a PR sensor requires the model to be optimized in both mechanical and electrical aspects hence a multi-criteria optimization based on a multi-physics model needs to be considered for practical sensing applications. There are many examples of multi-criteria optimization problems based on 3D TPMS models, mostly applied to heat sink design problems (Das & Sutradhar, 2020; Modrek et al., 2023). In Das & Sutradhar (2020), the final objective function is a weighted combination of mechanical and thermal compliance. The model is tested on different numerical examples and was shown to be effective. Modrek et al. (2023) also follow a similar approach and add TPMS unit cells into the material model formulation. The materials are homogenized and modeled using a modified SIMP model from the homogenization of TPMS unit cell geometries. They also test the objective function with different weights. Similarly, Li et al. (2019) introduced the generic optimization scheme for FG TPMS structures and applied this method to structural and thermal problems separately (Li et al., 2019). In many examples applied to mechanical, thermal and biological application (Li et al., 2019; Modrek et al., 2023; Simsek et al., 2020), the main design scheme is similar. Essentially, a single unit cell is defined by TPMS geometries with different thicknesses and therefore the intermediate densities are also mapped to geometries suitable for fabrication. Relative density of the cells and material properties are connected by a modified SIMP based on numerical homogenization which therefore preserves the output of the TO algorithm hence resulting in better performance by being manufacturable at the same time. As mentioned before, the resulting interconnected nature of graded or uniform TPMS structures, allows to realize these designs using AM. During AM, the geometry is sliced into many cross-sections which gives the user a very precise control of geometry and geometrical features such as porosity. With the increasing options of materials for AM and simplicity of the production process, it is the preferred fabrication method for 3D structures such as porous sensors.

In this thesis we propose a TO framework based on numerical homogenization of PR gyroid unit cells. Since thermal and electrical conduction are analogical to each other, we relied on a systematic procedure to apply the framework to three classes

of TO problems by first considering the mechanical or electrical performance individually build the backbone of the 3D PR TO model. Finally, the design scheme is applied to PR material based multi-criteria design of the sensor targeting both mechanical and electrical performance simultaneously. To the best of our knowledge, the design of 3D PR sensors using TO based on TPMS homogenization does not exist. More specifically, a PR pressure sensor is designed by using TO with modified SIMP material models for bedsores prevention (occurring at 4666 Pa). The simulation model was built and analyzed using FEM in COMSOL Multiphysics 6.2 and the TO framework was developed considering different design case studies. For the optimization, key material properties for the sensor, Young's modulus, initial conductivity, and elastoresistivity properties are homogenized and used to construct modified SIMP models to be used in the design studies. Homogenization of the piezoresistance properties using gyroid unit cells is one of the main contributions of this study. The topology optimization framework based on their modified SIMP models to deliver optimal graded TPMS topologies is another novel outcome. It is also important to note that this study is based on a coupled solid mechanical-electrical response models of the PR sensor.

### 1.3 Goals and Contributions

The objective of this thesis is to develop a TO framework based on numerical homogenization of PR gyroid unit cells suitable for the design of pressure sensors with 3D graded optimal topologies. Since thermal and electrical conduction are analogical to each other, we relied on existing thermal 3D optimization studies focusing on planar PR optimization to build the backbone of the 3D PR TO model. To the best of our knowledge, the design of 3D PR sensors using TO based on TPMS homogenization does not exist. More specifically, in this thesis, a PR pressure sensor is designed by using TO with modified SIMP material models for bedsores applications (most sensitive at 4666 Pa). The simulation model was built and analyzed using FEM in COMSOL Multiphysics 6.2 and the TO framework was developed and applied to different design case studies based on different criteria and optimization models. For the optimization, key material properties for the sensor, Young's modulus, initial conductivity, and piezoresistivity matrix are homogenized and used to construct modified SIMP models to be used in these design studies. Homogenization of the material properties such as elasticity, initial conductivity and piezoresistiv-

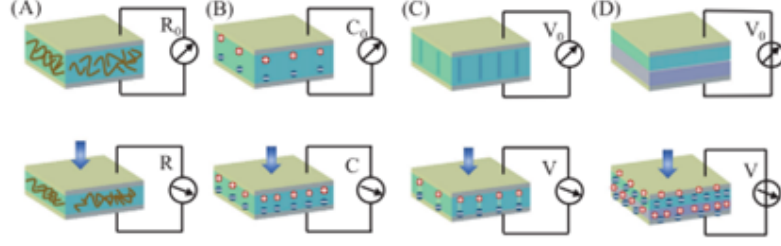
ity/elastoresistivity using TPMS gyroid unit cells is one of the main contributions of this thesis. The topology optimization framework based on their modified SIMP models to deliver optimal graded 3D TPMS topologies with optimal sensitivity performance for bedsores prevention is another novel outcome. It is also important to note that this study relies on a coupled solid mechanical-electrical response based multiphysics model for predicting the PR sensor performance. The outline of the thesis is as follows: Chapter 2 builds more on the background of piezoresistivity and modeling steps. Methodology of the analysis and optimization procedure are provided in Chapter 3, and the results of the simulations are given in Chapter 4. Finally, conclusions and future work are presented in Chapter 5.

## 2. Background

### 2.1 Piezoresistive Pressure Sensors

Flexible pressure sensors utilize mechanisms such as piezoelectricity, capacitance and piezoresistivity to measure pressure. Piezoresistivity originates from materials with changing resistances under deformation. This effect can be due to changing geometric properties, intrinsic resistivity or both. OR pressure sensors can be made of metal, semiconductors, and conductive polymer composites. Metal sensors depend on macroscale geometric deformation. In semiconductors, the effect is tied to changes in the band structure, which significantly impact both carrier mobility and number density—far more than applied stress would affect the resistance of a comparable metal. Conductive polymer composites' main working mechanism depends on tunneling resistance (Duan, D'hooge & Cardon, 2020). Fig. 2.1 shows the working mechanism of different types of nanocomposite sensors (Tang et al., 2021). The composite sensor is composed of conductive particles diffused in a flexible polymer. The filler material creates a conductive network. When pressure is applied on the material, distance between the conductive nanoparticles decreases, creating paths for electrons to cross over with less energy, hence resistance is lowered (Seesaard & Wongchoosuk, 2023). This effect is called the tunneling effect.

Figure 2.1 Working mechanism of different types of nanocomposite pressure sensors: (A) Piezoresistivity (B) Capacitive (C) Piezoelectricity (D) Triboelectricity (Tang et al., 2021)



The related concept of elastoresistance links the material's strain to changes in resistivity. It's important to note that the relationship between the material's structural mechanics and its electrical properties is one-way, meaning that applied currents do not affect the material's stress or strain, provided that other factors, such as heating, are negligible (Definition, 2013). Governing equations for modeling the PR sensors can be summarized in the form of Hooke's Law, Ohm's Law and piezoresistance constitutive relationship as follows:

$$\mathbf{S} = \mathbf{C} \cdot \boldsymbol{\varepsilon} \quad (2.1)$$

$$\mathbf{J} = \boldsymbol{\sigma} \cdot \mathbf{E} \quad (2.2)$$

$$\Delta\rho = \boldsymbol{\Pi} \cdot \mathbf{S} + \mathbf{M} \cdot \boldsymbol{\varepsilon} \quad (2.3)$$

The third equation relates stress or strain load to change in resistivity  $\Delta\rho$ . Here,  $\mathbf{S}$  is the second-order stress tensor,  $\mathbf{C}$  is the fourth-order stiffness tensor,  $\boldsymbol{\varepsilon}$  is the second-order strain tensor,  $\mathbf{J}$  is the current density vector,  $\boldsymbol{\sigma}$  is electrical conductivity matrix,  $\mathbf{E}$  is the electric field tensor,  $\Delta\rho$  is the second-order change in resistivity tensor,  $\boldsymbol{\Pi}$  is the fourth-order piezoresistance tensor, and  $\mathbf{M}$  represents the fourth-order elastoresistance tensor (Definition, 2013). Eq. 2.2 can be rewritten as

$$\mathbf{E} = \rho_r \mathbf{J} + \Delta\rho \mathbf{J} \quad (2.4)$$

This expansion clearly shows the effect of change in resistivity on the final electrical performance. As Eq. 2.3 dictates, the change of resistivity is a cumulative contribution of a PR response to the stress tensor  $\mathbf{S}$  or strain tensor  $\boldsymbol{\varepsilon}$ . These two contributions are used interchangeably, in other words when one part is active under given strain input or stress input, the other part is deactivated. Put in other words, to map the relationship between stress and change in resistivity the first part is used

and to map the relationship between strain and change in resistivity the second part is used.  $\Pi$  and  $M$  are material properties with units  $Pa^{-1}\Omega m$  and  $\Omega m$ , respectively. In this thesis, we used the strain activated resistivity change elastoresistance form, namely  $\Delta\rho = M \cdot \varepsilon$ , which depends on the elastoresistivity  $M$ .

It's important to note that in COMSOL Multiphysics, rather than applying a scalar factor outside of  $m$  which is only feasible for materials with isotropic conductivity, the definition of  $m$  incorporates the resistivity directly into each element of the tensor (Definition, 2013). Both  $M$  or  $\Pi$ , are tensors of rank 4, which consist of 21 independent components in the most general case, but for cubic symmetric structures such as the sheet based gyroid unit cell used in this thesis, they can be reduced to three components, which for  $m$  implies  $m_{11}$ ,  $m_{12}$ , and  $m_{44}$  (Wymysłowski, Santo-Zarnik, Friedel & Belavič, 2004). Throughout the thesis direction  $z$  will be referred as "1" in subscripts, since the geometry is cubic symmetric numeration of  $x$  and  $y$  do not differ. Using the Voigt notation (also used in COMSOL) for Eq. 2.3, the resistivity change can be redefined as:

$$\begin{bmatrix} \Delta\rho_{11} \\ \Delta\rho_{22} \\ \Delta\rho_{33} \\ \Delta\rho_{12} \\ \Delta\rho_{13} \\ \Delta\rho_{23} \end{bmatrix} = \begin{bmatrix} m_{11} & m_{12} & m_{12} & 0 & 0 & 0 \\ m_{12} & m_{11} & m_{12} & 0 & 0 & 0 \\ m_{12} & m_{12} & m_{11} & 0 & 0 & 0 \\ 0 & 0 & 0 & m_{44} & 0 & 0 \\ 0 & 0 & 0 & 0 & m_{44} & 0 \\ 0 & 0 & 0 & 0 & 0 & m_{44} \end{bmatrix} \begin{bmatrix} \varepsilon_{11} \\ \varepsilon_{22} \\ \varepsilon_{33} \\ \varepsilon_{12} \\ \varepsilon_{13} \\ \varepsilon_{23} \end{bmatrix} \quad (2.5)$$

Furthermore, for an isotropic material, the material matrix properties can be defined by single scalar values. In this thesis, the material model employed within TO, namely SIMP model is based on both the mechanical and electrical material properties of the sensor which is mainly loaded along a single axis, i.e. uniaxial loading conditions apply and the materials throughout the study, unless otherwise stated were assumed to be isotropic.

Sensitivity of a PR sensor is measured by relative change in resistivity per strain or stress. Relative change in resistivity per stress is known as its sensitivity and per strain is defined as the pressure sensor's gauge factor (Eq. 2.6). In mathematical terms, these definitions can be expressed using following equations:

$$Sensitivity = \frac{\Delta R/R_0}{S} \quad GaugeFactor = \frac{\Delta R/R_0}{\varepsilon} \quad (2.6)$$

Sensitivity and gauge factor are considered as the most important design metrics of a

pressure sensor particularly for detecting structural damage or subtle displacements (Duan et al., 2020). As stated earlier, one of the goals in this thesis is to design a suitable pressure sensor for bedsores detection application where bedsores are known to develop in bedridden patients (Misaki et al., 2014). Based on studies in literature, skin cells start to die at a critical pressure value due to bedsores, which corresponds to the an applied pressure value of 4666 Pa. Therefore, in this thesis, the sensor is modeled and designed at this pressure with a target of maximizing its sensitivity.

In this thesis, material properties of the sensor that control its sensitivity constitute both the elastoresistivity (which requires the initial conductivity) as well as the elasticity of the sensor. These material properties are homogenized for sheet based gyroid unit cells and integrated to the design scheme using as modified SIMP models. Next, we present details on the extraction of the modified SIMP law, followed by the theoretical basis of numerical homogenization. In the first part of the next chapter, we provide implementation details and the corresponding numerical results regarding the homogenization models in COMSOL.

## 2.2 Lattices and the modified SIMP Law

Lattices, which are a subset of cellular solids, include both natural structures (like cancellous bone and honeycomb) and synthetic materials (such as polymer foams) (Maskery, Aremu, Parry, Wildman, Tuck & Ashcroft, 2018). Gibson and Ashby have provided insights on how the properties of cellular solids, like density and pore size, affect their physical attributes (Gibson & Ashby, 1997). Relationship of relative elastic modulus and the volume fraction of a cellular structure is one of the properties, and is defined as follows:

$$E^* = A\rho^n \tag{2.7}$$

where  $A$  and  $n$  are constant numbers for each lattice, where effective elastic modulus  $E^*$  and relative density  $\rho$  are defined as  $E^* = E_{latt}/E_{sol}$  and  $\rho = \rho_{latt}/\rho_{sol}$ , respectively. The subscript "latt" refers to the lattice property and "sol" is the solid material without any geometry effect.  $\rho$  is normalized and ranges between 0 and 1, this variable is referred to as both relative density and volume fraction in this thesis. The coefficient  $A$  in Eq. 2.7 was derived by Gibson & Ashby (1997), who

suggested a value between 0.1 and 4.0 (Maskery et al., 2018). The exponent  $n$  is approximately 2 when the deformation involves bending of the structure’s struts or walls. The values are adjusted with respect to the deformation and the lattice structure’s microstructure that is the unit cell geometry. In this thesis, we use a sheet based gyroid to model a unit cell and construct its effective material property, i.e. perform homogenization. In the next subsection, we show how each of the three material properties are homogenized for conducting design within a TO framework that will rely on the use of these modified SIMP laws.

## 2.3 Homogenization of Elasticity, Initial Conductivity and

### Elastoresistivity

The homogenization method is a widely recognized technique used to determine the effective material properties of composites. Homogenization theory is a mathematical approach which characterizes the average or effective behavior of microscopically heterogeneous materials at the macro scale. Developed in the 1970s, it was initially applied to periodic domains through two-scale asymptotic expansions by Babuška (Babuška, 1976). The heterogeneous material is assumed to consist of two scales: the micro-scale which the material is heterogeneous and periodic, the macro-scale which is the material is homogeneous and made of the periodic micro-scale building blocks, hence can be represented with the effective properties (Ozdilek, Ozcarar, Muhtaroglu, Simsek, Gulcan & Sendur, 2024).

Homogenization method aims to capture the effects of the micro-scale by representing the average behavior of the material in a homogeneous medium. Rather than modeling the entire macro-scale with all its complexities, which would be computationally overwhelming, a single periodic cell at the micro-scale is analyzed in detail. The results from this analysis are then used to predict the average behavior at the macro-scale, which is the core principle of homogenization. Some examples of homogenization techniques are surface or volume average approach, micro-polar theory, beam theory approach and asymptotic homogenization (AH) (Ozdilek et al., 2024).

Asymptotic expansion-based homogenization (AH) is a well-known and effective technique for determining the elastic properties of periodic unit cells (PUCs) (Hasani & Hinton, 1998). This approach allows the calculation of macroscopic charac-

teristics of heterogeneous materials by utilizing coefficients obtained from the state equations. These coefficients are derived through the asymptotic expansion of the solution and a parameter that defines the ratio of the unit cell period to the overall length (Wang, Cai, Zhou & Hu, 2021).

An alternative approach utilizes the energy-based homogenization method (EBHM) (Sigmund, 1994), which relies on the average stress and strain theorems to estimate the effective properties. Unlike the numerical homogenization of the AH method, EBHM applies periodic boundary conditions to the boundaries of PUCs, simplifying the initial elastic equilibrium equation in finite element analysis into a more concise form (Xia, Xia, Huang & Xie, 2018). Consequently, the numerical process of predicting effective properties using EBHM is more straightforward. Additionally, the simplified theoretical framework of the energy-based method makes it easier to integrate with design strategies like topology optimization.

### 2.3.1 Elasticity and Initial Conductivity Homogenization

The material modeling of TO based design framework is based on a repeated sheet based gyroid unit cell geometry, and therefore the numerical homogenization procedure results in modified SIMP laws for each relevant material properties. The fundamentals of this method rely on modeling the gyroid geometry with implicit Finite elements such as hexahedral elements as opposed to modeling the geometry in an explicit fashion (Şimşek et al.). The numerical homogenization scheme is well documented for linear elastic material's elasticity tensor. In this thesis, we mainly follow Li et al. (2019)'s numerical homogenization method to homogenize the material properties necessary to model piezoresistive effect of the pressure sensor that is designed in this thesis which comprise mainly the following material properties: the elasticity matrix, the initial conductivity and piezoresistivity material matrix.

Elasticity tensor  $C_{ijkl}$  relates strain tensor  $\varepsilon_{kl}$  to stress tensor  $S_{ij}$  by Hooke's Law for linear elastic materials,  $S_{ij} = C_{ijkl}\varepsilon_{kl}$ . Due to TPMS lattices belonging to lattices obeying threefold rotational symmetry, i.e. they are known to be cubic symmetric, and the elasticity matrix property itself obeys symmetry for linear elastic materials, elasticity tensor reduces to the use of 7 distinct elements in Eq. 2.8.

$$C_{ij} = \begin{bmatrix} C_{11} & C_{12} & C_{12} & C_{14} & C_{15} & C_{16} \\ C_{12} & C_{11} & C_{12} & C_{16} & C_{14} & C_{15} \\ C_{12} & C_{12} & C_{11} & C_{16} & C_{15} & C_{14} \\ C_{14} & C_{16} & C_{16} & C_{44} & C_{45} & C_{45} \\ C_{15} & C_{14} & C_{15} & C_{45} & C_{44} & C_{45} \\ C_{16} & C_{15} & C_{14} & C_{45} & C_{45} & C_{44} \end{bmatrix} \quad (2.8)$$

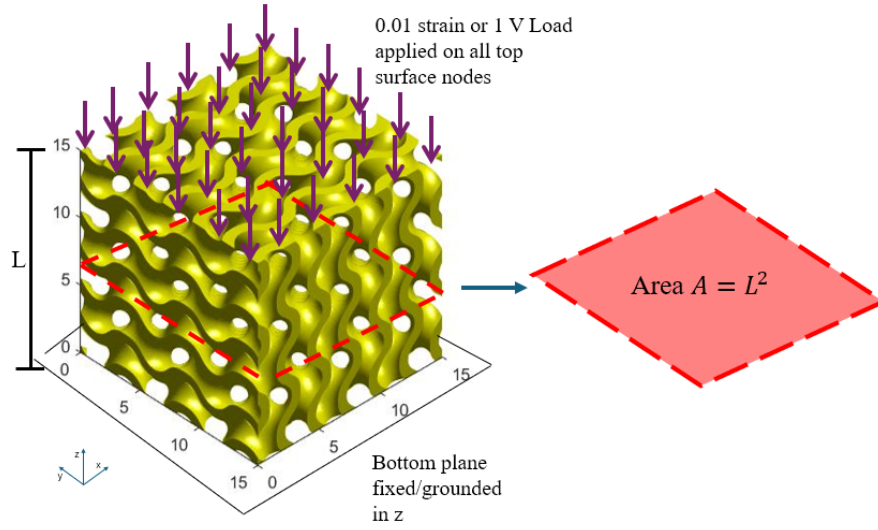
A cubic symmetric geometry such as gyroid and Schwarz-P lattice geometries belonging to the TPMS family allow for further matrix simplifications and the expression of the elasticity matrix using a total of only 3 independent matrix elements as shown in (Eq. 2.9).

$$\begin{bmatrix} S_{11} \\ S_{22} \\ S_{33} \\ S_{12} \\ S_{13} \\ S_{23} \end{bmatrix} = \begin{bmatrix} C_{11} & C_{12} & C_{12} & 0 & 0 & 0 \\ C_{12} & C_{11} & C_{12} & 0 & 0 & 0 \\ C_{12} & C_{12} & C_{11} & 0 & 0 & 0 \\ 0 & 0 & 0 & C_{44} & 0 & 0 \\ 0 & 0 & 0 & 0 & C_{44} & 0 \\ 0 & 0 & 0 & 0 & 0 & C_{44} \end{bmatrix} \begin{bmatrix} \varepsilon_{11} \\ \varepsilon_{22} \\ \varepsilon_{33} \\ \varepsilon_{12} \\ \varepsilon_{13} \\ \varepsilon_{23} \end{bmatrix} \quad (2.9)$$

Moreover, based on cubic symmetry, the homogenized Young's Modulus can be derived from the elasticity tensor components using Eq. 2.10 Li et al. (2019). The process of numerical homogenization (Bensoussan, Lions & Papanicolaou, 2011) refers to the computation of these effective material matrix elements with which a homogeneous cube of material would represent an equivalent response, such as displacement or voltage difference, to the response of the unit cell with a 3D microstructure if repeated periodically in three dimensions. As a result, if one can extract the necessary matrix components for unit cells with different volume fractions, these can be used to map the volume fraction to the desired material property using an interpolation function such as power law. The resulting interpolation function then is used in conducting TO and later in reconstruction of the resulting grey scale topologies to graded TPMS topologies.

$$E = \frac{C_{11}^2 + C_{11}C_{12} - 2C_{12}^2}{C_{11} + C_{12}} \quad (2.10)$$

Figure 2.2 Boundary conditions and area definitions properties used in numerical homogenization models and validation studies



To extract the effective elasticity tensor components, one strain component is set to one, and the remaining five are set to zero (Eq. 2.11) in each step as follows for the case of uniaxial strain in the 11, i.e.  $z$  direction. Fig 2.2 presents a visualization of the Boundary conditions when a strain is applied in a single direction to extract a property.

$$\begin{pmatrix} \varepsilon_{11} \\ \varepsilon_{22} \\ \varepsilon_{33} \\ \varepsilon_{23} \\ \varepsilon_{31} \\ \varepsilon_{12} \end{pmatrix} = \begin{pmatrix} 1 \\ 0 \\ 0 \\ 0 \\ 0 \\ 0 \end{pmatrix} \quad \begin{pmatrix} S_{11} \\ S_{22} \\ S_{33} \\ S_{23} \\ S_{31} \\ S_{12} \end{pmatrix} = \begin{pmatrix} C_{11} \\ C_{12} \\ C_{12} \\ C_{44} \\ C_{44} \\ C_{44} \end{pmatrix} \quad (2.11)$$

In the FEM model of the unit cell comprising a gyroid microstructure, strain is specified in the form of 1% displacement on the relevant boundary. The resulting stress will be calculated by extracting the reaction forces and dividing it to the cross sectional area of the entire unit cell per stress definition in Eq. 2.12.

$$S = \frac{F_{react}}{A_{surf}} \quad (2.12)$$

where  $F_{react}$  is the reaction force on a surface, and  $A_{surf}$  is the corresponding surface.

Per the Eq. 2.8 ,  $C_{11}$  and  $C_{12}$  can be extracted under the application of the same strain extension input but with corresponding surfaces where the reaction forces need to be computed for that particular elasticity matrix element. The reaction force for the  $C_{11}$  element computation, for instance, corresponds to the surface aligned along the uniaxial strain direction, i.e. 11, while  $C_{12}$  is based on the reaction force extracted on the surface perpendicular to the 11 direction, namely the 22 direction (Eq. 2.13).

$$\begin{aligned} C_{11} &= \frac{S_{11}}{\varepsilon_{11}} = \frac{F_{reac,1}}{A_{surf,1} \cdot \varepsilon_{11}} \\ C_{12} &= \frac{S_{22}}{\varepsilon_{11}} = \frac{F_{reac,2}}{A_{surf,2} \cdot \varepsilon_{11}} \end{aligned} \quad (2.13)$$

Further simplifications of Eq. 2.13 depends on the specific unit cell geometry that is used, therefore more details regarding the numerical implementation for the sheet based unit cell will be given in Chapter 3.

Since the constitutive law for conductivity is also based on a linear relationship like in the case of linear elasticity, homogenizing initial conductivity follows an analogues method to the extraction of the effective elasticity. This time, the constitutive law which involves the material property to be homogenized is Ohm's Law given in Eq. 2.14.

$$J_i = \sigma_{ij} \cdot E_j \quad (2.14)$$

Where  $J_i$  is current density tensor on a surface (or cross-section),  $\sigma_{ij}$  is conductivity matrix, and  $E_j$  is the electric field tensor on the same surface. More details regarding the implementation are given in Section 3.1 Fig. 3.5.  $\sigma$  is a 3 by 3 matrix, that can be reduced to an identity matrix given that the material is not subject to any loading or strain and is isotropic (Wymysłowski et al., 2004) (Eq. 2.15).

$$\sigma = \begin{bmatrix} \sigma_{11} & \sigma_{12} & \sigma_{13} \\ \sigma_{21} & \sigma_{22} & \sigma_{23} \\ \sigma_{31} & \sigma_{32} & \sigma_{33} \end{bmatrix} = \begin{bmatrix} \sigma_{11} & 0 & 0 \\ 0 & \sigma_{11} & 0 \\ 0 & 0 & \sigma_{11} \end{bmatrix} \quad (2.15)$$

Conductivity matrix elements can be extracted by applying electric field or rather voltage one at a time, just like strain in the elasticity tensor. For the numerical implementation in an FEM model, 1V potential is applied to a surface and the opposite surface is grounded to create an electric field. It is also noted that average electric field is the potential difference per length, i.e.  $E = \Phi/L$ . Then, using Ohm's

law and the unit cell cubic geometry which is of size  $5 \times 5 \times 5 \text{ mm}^3$ , the conductivity along the 11 direction, is calculated from the following equation:

$$\sigma_{11} = j_1 / \frac{1V}{L} \quad (2.16)$$

with  $L$  being the lengths of the unit cell in the  $x$  and  $y$  directions and  $L$  is the distance between the surfaces of the unit cell, that is its thickness,

The corresponding normal current density  $j_1$  (an element of the  $J$  vector) is calculated by dividing the total current on the respective surface to the value of the surface area of the design space (Fig. 2.2). In COMSOL we used the integration function to do the calculation, which will be explained in more detail in the following chapters.

The derivation of the modified SIMP law requires to repeat the above procedure described for the elasticity matrix and initial conductivity property for relative densities ranging from 0.1 to 0.7 of the gyroid unit cell. This lower and upper limits are chosen based on the modeling ability of the gyroid geometry with features without disconnections and discontinuities. More specifically, similar to existing literature (Al-Ketan, Lee, Rowshan & Abu Al-Rub, 2020; Panesar, Abdi, Hickman & Ashcroft, 2018), for values of volume fractions smaller than the given range, the geometry results in a disconnected structure since the walls become too thin, whereas for larger values of volume fractions, pores start to close-up and the geometry lacks the desired smooth surface behavior. The relationships between the material property and relative densities are then fitted to an interpolation function. Usually this fit is done using power laws as suggested by Gibson-Ashby equations (Eq. 2.7). In this thesis we increased the number of terms of the fitted function, i.e. in the Gibson-Ashby equations to improve the interpolation's accuracy (Table 2.1).

### 2.3.2 Elastoresistivity Homogenization

A piezoresistive sensor material response is inherently governed by Hooke's Law and Ohm's Law at the same time. In addition to these two, there is a third equation that connects the two constitutive laws to each other through the definition of piezoresistivity, Eq. 2.3 which was introduced in Section 2.1. As was pointed out in Section 2.1, for a cubic symmetric structure, the relevant material property refers to the elastoresistivity matrix that can be reduced to 3 elements. In addition to

this, Wymysłowski et al. (2004) states that in most cases  $m_{44}$  is equal to zero. Accordingly, the homogenization procedure in essence only requires the extraction of  $m_{11}$  and  $m_{12}$  by applying unit strain in one of the directions, say z axis indexed with 1 throughout the thesis, hence the applied strain refers to  $\varepsilon_{11}$ . The analysis of a single strain in a chosen direction should be sufficient for the solution of the necessary elastoresistance tensor elements. For  $\varepsilon = \begin{bmatrix} \varepsilon_{11} & 0 & 0 & 0 & 0 & 0 \end{bmatrix}$ , Eq. 2.5 will simplify to

$$\begin{aligned}\Delta\rho_{11} &= m_{11} \cdot \varepsilon_{11} \\ \Delta\rho_{22} &= m_{12} \cdot \varepsilon_{11} \\ \Delta\rho_{33} &= m_{12} \cdot \varepsilon_{11}\end{aligned}\tag{2.17}$$

where  $\Delta\rho_{22}$  and  $\Delta\rho_{33}$  are observed to be equal and will be treated as such in the remainder of the thesis. Therefore calculating  $\Delta\rho_{11}$  and  $\Delta\rho_{22}$  is sufficient to compute the effective or homogenized  $m$  matrix of a repeated unit cell using numerical homogenization (Wymysłowski et al., 2004). As mentioned before, the materials are assumed to be isotropic, therefore the elastoresistivity matrix can be defined by single scalar value,  $m$ . Accordingly,  $m$  is a material property that linearly connects strain to change in resistivity ( $\Delta\rho_{11} = m \cdot \varepsilon_{11}$ ). But change in resistivity, unlike stress or current response of a sensor when subject to strain and voltage input, is not a directly calculated or measured output in an experimental setup, hence one way of extracting it is to rely on Ohm's Law, i.e.  $\mathbf{J} = \sigma_c \mathbf{E}$ . Use of Ohm's law in connection to the change of resistivity definition under applied strain, yields the following matrix equation (Eq. 2.18) for the current density components  $j_1, j_2, j_3$  in terms of the change of resistivity components  $\Delta\rho_{11}, \Delta\rho_{22}$ , and  $\Delta\rho_{33}$  and the electric field vector  $\mathbf{E}$  with components  $E_1, E_2$ , and  $E_3$ .

$$\begin{bmatrix} j_1 \\ j_2 \\ j_3 \end{bmatrix} = \begin{bmatrix} \sigma_0 + \frac{1}{\Delta\rho_{11}} & 0 & 0 \\ 0 & \sigma_0 + \frac{1}{\Delta\rho_{22}} & 0 \\ 0 & 0 & \sigma_0 + \frac{1}{\Delta\rho_{33}} \end{bmatrix} \begin{bmatrix} E_1 \\ E_2 \\ E_3 \end{bmatrix}\tag{2.18}$$

Here,  $\sigma_0$  is the initial conductivity. As materials are assumed to be isotropic based on the earlier equality observation, the diagonal elements of the conductivity matrix are also treated to be equal. One row of the matrix equation can be rewritten in shorthand notation as

$$j_1 = (\sigma_0 + (\Delta\rho_{11})^{-1}) \cdot E_1.\tag{2.19}$$

$\Delta\rho$  is the difference between the inverse of final conductivity  $\sigma_f$  (i.e. final resistivity) and inverse of initial conductivity  $\sigma_0$  (Eq. 2.20), and therefore the current density and the electric field can be related to each other using the sum on the right hand side in Eq. 2.19.

$$\Delta\rho = \rho_f - \rho_0 = \sigma_f^{-1} - \sigma_0^{-1} \quad (2.20)$$

Keeping that in mind Eq. 2.20 and recalling that  $\Delta\rho = m \cdot \varepsilon$  (Eq. 2.3), the following equality is derived:

$$m \cdot \varepsilon_{11} = \sigma_f^{-1} - \sigma_0^{-1} \quad (2.21)$$

Since the aim is to define change in resistivity Eq. 2.20 can be rearranged as  $\Delta\rho = E_1/j_1$ . Then,  $m$  can be calculated as a post-processed quantity using the following final expression:

$$m = \frac{(E_1/j_1) - \sigma_0^{-1}}{\varepsilon_{11}} \quad (2.22)$$

During the FEM analysis, initial and final conductivities,  $\sigma_0$  and  $\sigma_f$ , are extracted from two different simulation models. In the former, there is no strain applied and a pure electrical response analysis under the application of voltage takes place. In the latter, electrical response is solved for under the application of strain. Equation 2.22 shows that to extract  $m$ , both electric field and strain must be applied to extract the final conductivity upon which  $m$  is based per definition as stated in 2.22. The boundary conditions as given in detail in Section 3.1, in the FEM model used for numerical homogenization of  $m$  is 1V potential difference and 0.01% strain applied along the same direction. It is basically a combination of the homogenization model inputs used for the calculation of effective Young's Modulus and initial conductivity properties.

## 2.4 Fabrication of Piezoresistive Pressure Sensors

Porous sensors including PR sensors, depending primarily on the materials used, are fabricated using various techniques including salt leaching or gas-foaming, phase-

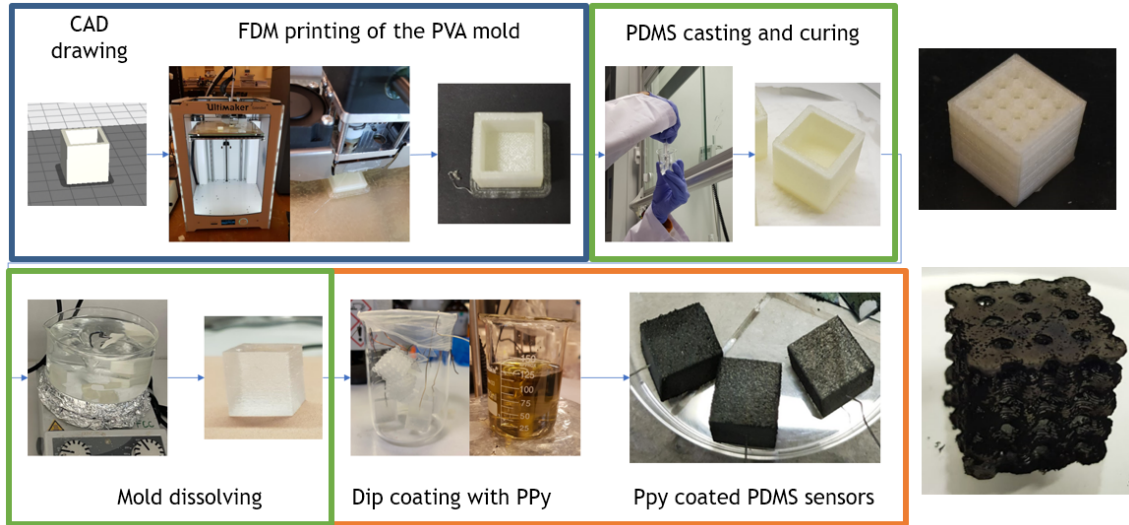
separation followed by freeze-drying and lately additive manufacturing (Feng et al., 2022). In most of the sensor design fabricated using traditional pore forming methods, to directly and precisely control the pore properties remains a challenge where additive manufacturing (AM) stands out. During AM, the geometry is sliced into many cross-sections which gives the user a very precise control of porosity. With the increasing options of materials for additive manufacturing and simplicity of the production process, it is the preferred fabrication method for 3D structures such as porous sensors. Main techniques of AM comprise liquid, solid and powder based methods. These divide into subcategories within themselves too. The most common used technique is fused deposition modelling using liquid-material processing (Rasiya, Shukla & Saran, 2020). The thin plastic filament is molten (hence the liquid-based name) at the printer head and extruded on the printer plate layer by layer. Filaments used for Fused Deposition Modeling (FDM) printing have high melting temperatures and cool down and solidify once it leaves the printer head.

Flexible materials such as Polydimethylsiloxane (PDMS) are not suitable for FDM printing. As a result, a mold is modeled to cure the flexible material inside. The mold must be a disposable material so that it could be eliminated after the curing process. Although in this thesis we did not present any fabrication related efforts, the feasibility of manufacturing TPMS based sensors was tested in our research group experimentally (Erulker et al., 2022) for which the basis steps are provided in Fig. 2.3. Here, Polyvinyl alcohol (PVA) was used to fabricate the mold which geometrically is in the complementary/negative form of the TPMS sensor geometry CAD model. PVA is commonly used as a support material during FDM printing because it is eco-friendly and can dissolve in water without need of any extra materials or post-processing. Here, the main idea relies on the lost-mold technique where the sensor made of PDMS and coated with a piezoresistive conducting polymer, Polypyrrole (PPy) was then filled into the PVA mold, cured and then the mold was dissolved in distilled water to deliver the TPMS geometry of the PDMS sensor.

## 2.5 Topology Optimization and SIMP Models

In the last three decades, topology optimization has experienced significant developments with a wide range of applications from traditional mechanics to fluid mechanics, heat transfer and electromagnetics, as well as multiphysics applications (Bendsøe & Sigmund, 2003). In very basic terms, it can be regarded as a numeri-

Figure 2.3 Fabrication steps of a TPMS sensor using lost mold technique based on (Erulker et al., 2022)



cal iterative procedure to find the best material distribution in the pre-defined design domain. Various topology optimization methods have been developed including the homogenization method (Bendsøe & Kikuchi, 1988), the Solid Isotropic Material with Penalization (SIMP) (Zhou & Rozvany, 1991), the Evolutionary Structural Optimization (ESO) (Xie & Steven, 1993) and the Level Set Method (LSM) (Wang, Wang & Guo, 2003) and more recent methods such as the phase field method (e.g., Takezawa, Nishiwaki & Kitamura (2010)), and the moving morphable component (MMC) method (e.g., Guo, Zhang & Zhong (2014)).

Designing through topology optimization (TO) is to calculate the optimal arrangement of a limited volume of material within a spatial domain to achieve the best response formulated in terms of a mathematical objective function, in the case of the study in this thesis, this is sensitivity of the PR pressure sensor. For the optimization process one must first define the objective function and the limiting conditions. For example, for the mechanical compliance case, the objective is to minimize strain energy density while there is an upper limit for the total volume of the material, and the governing physics is based on the continuity equation of linear elasticity subject to Hooke's Law and the definition of strain. The optimization process systematically and iteratively redistributes material throughout the domain to create the final structure. The amount of the material in every unit cell after the distribution is called relative density,  $\rho_e$ . Unlike size and shape optimization methods, TO can represent complex and arbitrary topologies without the need for remeshing or intricate shape functions (Simsek et al., 2020).

In a TO design framework based on SIMP, an explicit relationship between an

artificial density variable representative of relative density or volume fraction of the FE cell and the respective material property. Standard SIMP based models are exponential. Table 2.1 shows the interpolation function for each material property constructed via numerical homogenization procedure as described in this section. These are the so-called modified SIMP material models used in the TO framework developed in this thesis. The corresponding multi-physics model of the PR sensor rely on the solution of linear elasticity and electrostatics coupled via piezoresistivity of the material. The relevant screenshots of the implemented model are shown in Appendix 4. The PR sensor is envisioned as a volumetric design domain that is composed of PR material that shows both elastic and piezoresistive behavior according to prescribed modified SIMP models shown in Table 2.1 governing each physical material property.

Table 2.1 Form of the modified SIMP functions used for respective material properties

<b>Material Property</b>	<b>SIMP Function</b>
Young's Modulus	$E(\rho) = E_{sol} \cdot (a_1 \cdot \rho^{n_1} + b)$
Initial Conductivity	$\sigma_0(\rho) = (\sigma_0)_{sol} \cdot (a_2 \cdot \rho^{n_2} + b)$
Elastoresistivity matrix component	$m(\rho) = m_{sol} \cdot (a_3 \cdot \rho^{n_3} + b)$

Here  $E_0, \sigma_0$  and  $m_0$  are the three material properties of the pressure sensor, namely the Young's modulus, initial conductivity and elastoresistivity matrix, respectively. It is noted that the original solid mechanical material property matrix demands three material constants but the chosen sheet based gyroid unit cell is shown in literature to display negligible anisotropy and therefore is reduced to a single isotropic material constant of C11 which is directly related to the Young's modulus only. Additionally, the use of an isotropic material model i.e., SIMP is justified based on the isotropic behavior for sheet based gyroid TPMS lattices as documented and used in literature (Chatzigeorgiou, Piotrowski, Chemisky, Laheurte & Meraghni, 2022; Li et al., 2019; Lu, Zhao, Cui, Zhu & Wu, 2019).

## 2.6 Geometric Modeling of the Gyroid Unit Cell

The procedure of developing the SIMP functions for a material property, i.e. the numerical homogenization procedure is described in detail in the previous section,

and specific implementation details in the numerical simulation model will be given in Chapter 3.

The correct implementation of this procedure is based on the geometric modeling of the unit cell model used. The geometry chosen for this study is a sheet based gyroid, a type of TPMS. We summarize the necessary equations and procedure that was implemented using a MATLAB script code to generate gyroid unit cells. More details can be found in similar modeling efforts as in Simsek et al. (2020)'s.

Among various techniques used for modeling TPMS geometries, the common sheet phase modeling approach is based on an implicit function to generate the  $U = 0$  iso-surface of the generalized equation given below:

$$f_{TPMS}(k_x, k_y, k_z, x, y, z) = t \quad (2.23)$$

where the periodic properties of the surfaces are governed by:

$$k_i = 2\pi \frac{n_i}{L_i} \quad (i = x, y, z) \quad (2.24)$$

with  $k_i$  representing the periodicity of the TPMS function,  $n_i$  denoting the number of cells, and  $L_i$  being the total length of the structure in each respective direction. The parameter  $t$  controls the volume fraction of the generated structure which physically represents the thickness of the gyroid geometry within the unit cell. Previous studies have demonstrated that this relationship is linear for most unit cells within the manufacturable range of volume fractions. The matrix phase equations for the applicable TPMS can be easily derived by squaring both sides of Eq. 2.23.

In this thesis, since a sheet based gyroid structure is chosen in conducting all simulations including optimization the corresponding Gyroid iso-surface function can be represented in the following form and is encoded in MATLAB:

$$U = [\cos(k_x x) \cdot \sin(k_y y) + \cos(k_y y) \cdot \sin(k_z z) + \cos(k_z z) \cdot \sin(k_x x)]^2 - t^2 \quad (2.25)$$

With the explicit function definition of  $U$ , the surface of the unit cell geometry can be modeled and via the use of algorithms such as the marching cubes, extraction of a triangulated face from this implicit surface description is possible. This allows not only for the unit cell model creation necessary for numerical homogenization but also should be used for the reconstruction of graded TPMS topologies of TO based

design results as shown in literature (Simsek et al., 2020). The reconstruction phase is not performed in this thesis.

For the former objective, numerical homogenization conducted in this thesis, unit cells were modeled of size  $5 \times 5 \times 5 \text{ mm}^3$  and for conducting the latter, i.e. TO design, a model of  $15 \times 15 \times 15 \text{ mm}^3$  design volume was defined with a mesh size of  $1 \times 1 \times 1 \text{ mm}^3$  to search for the optimal relative densities occupying these finite elements. It is also noted that the validation of the homogenization procedure requiring repeated unit cell topologies, a model of a  $3 \times 3 \times 3$  unit cells was developed.

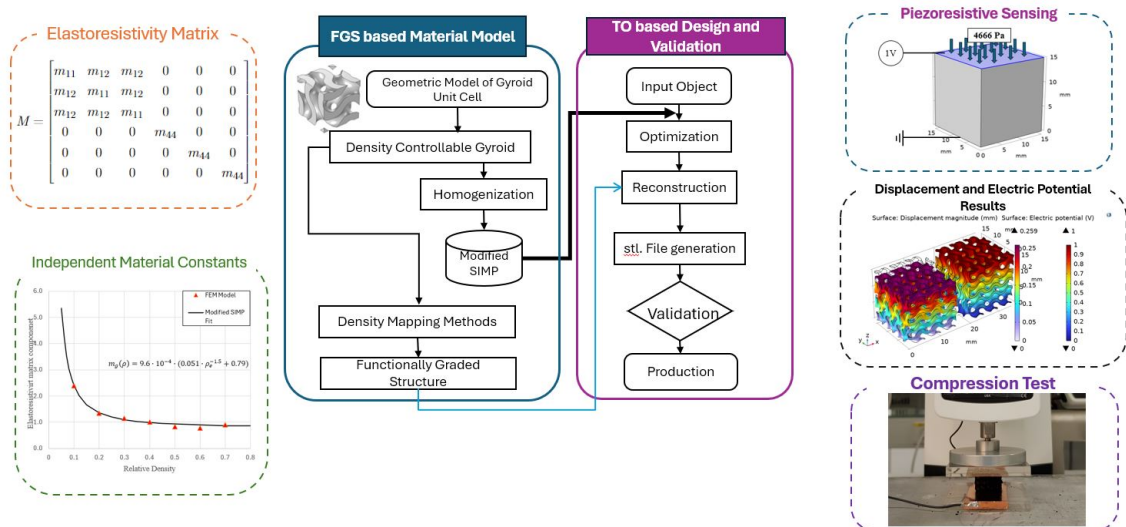
### 3. METHODOLOGY

In this chapter, information provided in Chapter 2 on the theoretical basis of the study presented in this thesis will be complemented with computational implementation details within the scope of this thesis.

First section of the chapter will give details about the implementation of the homogenization process within COMSOL Multiphysics, and the second section expands on the implementation details of the developed TO models presented in this thesis.

Proposed TO-based design scheme is mainly composed of two major modules as shown in Fig. 3.1 and is implemented to the design of PR pressure sensor targeting maximum sensitivity. The design scheme essentially is an integrated homogenization-based TO (HMTO), where in the first module, namely the FGS based material model serves two main purposes: to construct the modified SIMP models and to reconstruct the FGS using density mapping methods. As a first step towards both goals, sheet based gyroid unit cells are modeled with different relative densities using an implicit formula.

Figure 3.1 Developed design scheme for design optimization of functionally graded cellular structures (FGCS) applied to PR sensors



Next, a material model is established by interpolation based on a set of simulations performed to relate the three material properties of the gyroid lattice to its relative densities. In the last step towards the first output, the original SIMP formula is modified by the corresponding equations extracted from homogenization studies, and fed into the second module to perform TO. Towards the second output of FGS, density mapping reconstruction takes place to transform the resulting optimal material distribution into a graded gyroid lattice structure. More specifically, the procedure starts with mapping the optimal densities from the optimization analysis for each corner node of a solid element using an arithmetic averaging scheme. Next, grids are enriched via tri-linear interpolation using relative density information of the corner nodes to achieve a smoother FGS which is preferred by AM. The reconstruction process ends up with voxelization and the STL geometry generation utilizing the enriched relative density grid, implicit gyroid formula, and the marching cubes algorithm (Newman & Yi, 2006). All these steps including tri-linear interpolation and voxelization are exactly adopted from an earlier study carried out in (Simsek et al., 2020).

In the second module of the design scheme, namely the optimization, the modified SIMP models are used and a TO is conducted to find the optimal material distribution for given boundary conditions and loading of the pressure sensor to achieve optimal performance such as maximum sensitivity.

Throughout the implementation of the design scheme, for numerical analysis FEM is used in COMSOL Multiphysics software which starts with the first step of the geometrical modeling. Here, the gyroid unit cell model was created as an .stl file via an in-house developed code in MATLAB and imported to COMSOL where it is solidified and meshed using a tetrahedral mesh for homogenization and a hexahedral mesh within the TO studies. Screenshots of the step-by-step implementation of the modeling scheme is shown in Appendix .1.

The remainder of the chapter is structured to provide details on each step of the design scheme shown in Fig. 3.1.

### **3.1 Derivation of modified SIMP Models using Homogenization**

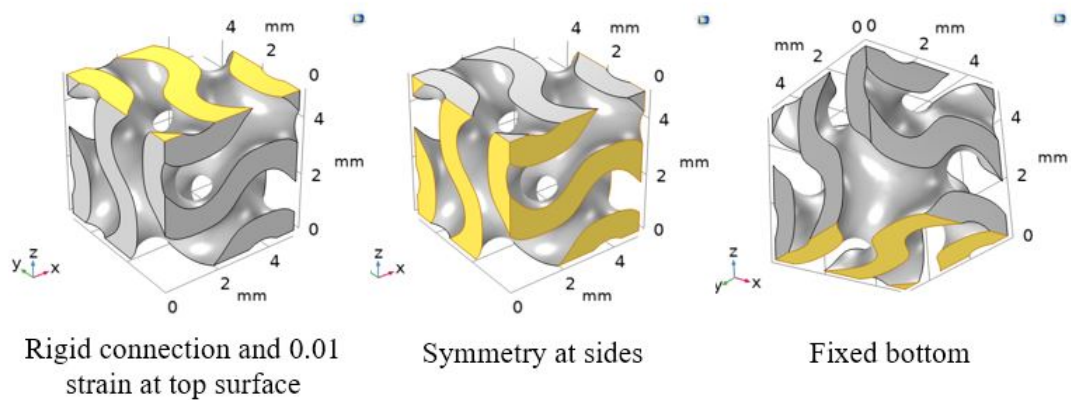
Three homogenization models were constructed to set up the optimization problem's SIMP modified material models for the following material properties: (1) the

mechanical property of the sensor, i.e. Young’s modulus, (2) initial conductivity, and (3) elastoresistivity material property to characterize the piezoresistive matrix property. The materials are assumed to be isotropic, hence the homogenized material models are fitted to a modified SIMP function using single scalar properties although all of the used material properties in their general form are tensors as explained in Chapter 2. A set of static analysis simulations were performed on the gyroid unit cell imported to COMSOL with different volume fractions ranging from 0.1 to 0.7. Properties of the analyzed unit cell models and simulation settings are explained for each of the respective material property’s homogenization scheme in the next sections. Also, their validations against the response of a homogeneous cubic model is described.

### 3.1.1 Homogenization of Effective Young’s Modulus and its Validation

A single unit cell gyroid model is used for Young’s Modulus homogenization. The unit cell size is 5 mm in every direction. A single unit cell is used to reduce computational requirement. *Symmetry Conditions* are used at the sides as shown in (Fig. 3.2) to represent the repetition condition of gyroid unit cells, a basic assumption for the mathematical homogenization theory to hold.

Figure 3.2 Boundary Conditions applied for the Young’s Modulus homogenization of a gyroid shown for a unit cell with 0.5 relative density



Referring back to Chapter 2, to find the effective Young’s Modulus, we use Eq. 2.10. Hence  $C_{11}$  and  $C_{12}$  should be extracted. These are extracted under the same loading condition per the matrix system equation. A 1% stain in  $z$  direction ( $\epsilon_{11}$ ) is applied from the top surface, and movement in  $x$  and  $y$  directions of the top surface

are restricted using the *Rigid Connector* node available in COMSOL. The bottom surface is fixed in every direction and the side surfaces are free to move. Since the rest of the strain values are zero, we are left with  $S_{11} = C_{11} \cdot \varepsilon_{11}$  and  $S_{22} = C_{12} \cdot \varepsilon_{11}$ . Reaction force is measured from the bottom surface. The total reaction force is calculated using *intop()* nonlocal coupling built-in function available in COMSOL at the bottom surface. *intop()* option is set to "summation over nodes". The calculated value is divided to the top surface area of the unit cell cube that the gyroid fits into. This implies that for the extraction of the effective property, rather than the surface area of the gyroid itself, the cross sectional area  $A_{surf}$  of the unit cell cube should be taken. A representative model and the relevant area definition is shown in Figure 2.2. This will give an "effective" material property value of the gyroid with prescribed relative density that a homogenized cube has to be assigned to yield the same effective mechanical response. Since the design space is cubic, length of all sides are of size  $L$ . Also uni-axial strain can be defined via  $L/\Delta L$  and substituted to Eq. 2.13 to extract  $C_{11}$  and  $C_{12}$  as follows:

$$C_{11} = \frac{F_{reac,1}}{L \cdot \Delta L} \quad C_{12} = \frac{F_{reac,2}}{L \cdot \Delta L} \quad (3.1)$$

In summary, the simulation for the numerical homogenization steps conducted for the gyroid unit cell in COMSOL are as follows:

1. Input of solid material properties which are chosen as shown in Table 3.1
2. Definition and extraction of  $C_{11}$  and  $C_{12}$  as variables (Fig. 3.14).
3. Rigid Connector boundary condition assignment at the top surface
4. Fixed Constraint assignment at the bottom surface
5. Conducting a stationary study run

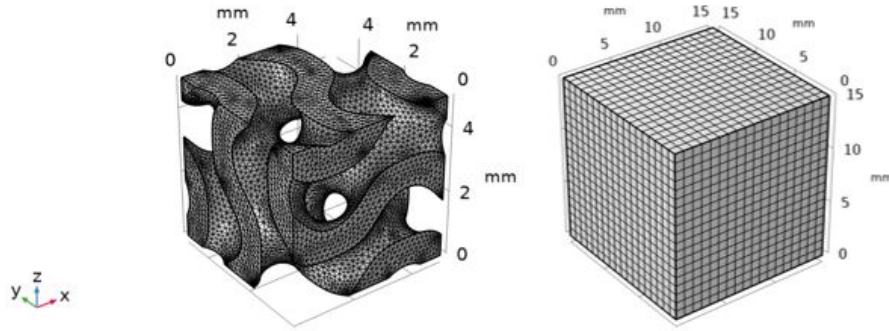
Table 3.1 Gyroid material properties: Young's modulus homogenization

<b>Material Property</b>	<b>Value</b>	<b>Unit</b>
Young's Modulus	2	MPa
Poisson's Ratio	0.49	
Density	980	kg/m <sup>3</sup>

It is noted that the solid material properties are chosen based on PDMS sensor material properties from literature (Moučka, Sedlačík, Osička & Pata, 2021). Free tetrahedral mesh is used to mesh the gyroid (Fig. 3.3). The exact meshing parameters change depending on the volume fraction of the gyroid unit cell since thinner

wall thicknesses will requires as a rule of thumb at least two-three finite elements per thickness for an acceptable modeling accuracy. The above step-by-step procedure for the numerical homogenization is repeated for all gyroid unit cell models created with different relative density values.

Figure 3.3 Mesh used for numerical homogenization of a gyroid unit cell and its homogeneous cubic counterpart model used for the validation of homogenization



After the repeated simulations for each volume fraction, the resulting values are fitted to an interpolation function,  $(E^*(\rho) = E_{sol}(a_1 \cdot \rho_1^n + b_1))$ , using Curve Fitting application of MATLAB (Fig. 4.4). The application uses Trust-Region algorithm with nonlinear least squares method to fit data sets. Power Law with one or two terms is one of the presented fit options. After the extraction of the modified SIMP model, the homogenization results are validated by comparing the responses of the gyroid unit cell and its homogeneous cube counterpart at each relative density. For validation purposes, this time a gyroid unit cell with 3 repetitions of size 5 mm unit cells was modeled in order to satisfy the periodic/repeated unit cell assumption for the theory of homogenization to hold. Higher number of unit cell repetitions are expected to yield a higher match with the response of the homogeneous material cube but is computationally prohibitive. The repeated gyroid model and its corresponding homogenized cube's dimensions are set to  $15 \times 15 \times 15 \text{ mm}^3$ . In the validation model, constant force is applied at the top surface of the repeated gyroid at the chosen relative density. One of the important steps in performing the comparison is to assign the homogenized material property evaluated with the fitted interpolation function to the cube model. That is the homogenized Young's Modulus value per the homogenization scheme of the gyroid at the specific relative density is used to test its validity. Bottom surfaces of both models used for comparison are fixed (Fig. 3.4), and their average top surface displacement is compared. In the validation model of the homogeneous cube, first step of the homogenization procedure is updated

with the earlier extracted homogenized data at the relative density chosen for the comparison. To do that, Young's modulus is replaced with the modified SIMP function's value, density is linearly dependent on relative density, and Poisson's ratio stays the same as summarized in (Table 3.2).

Figure 3.4 Boundary conditions of repeated gyroid (left) and cube (right) models used for Homogenized Young's Modulus validation

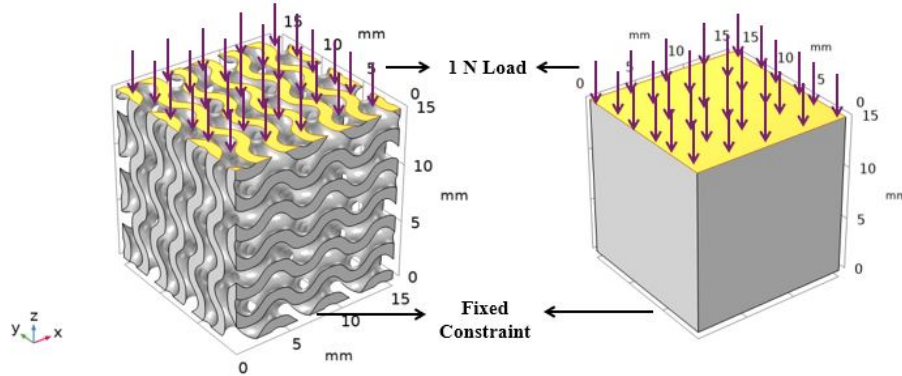


Table 3.2 Homogenized cube material properties: Validation of Young's modulus modified SIMP fit.

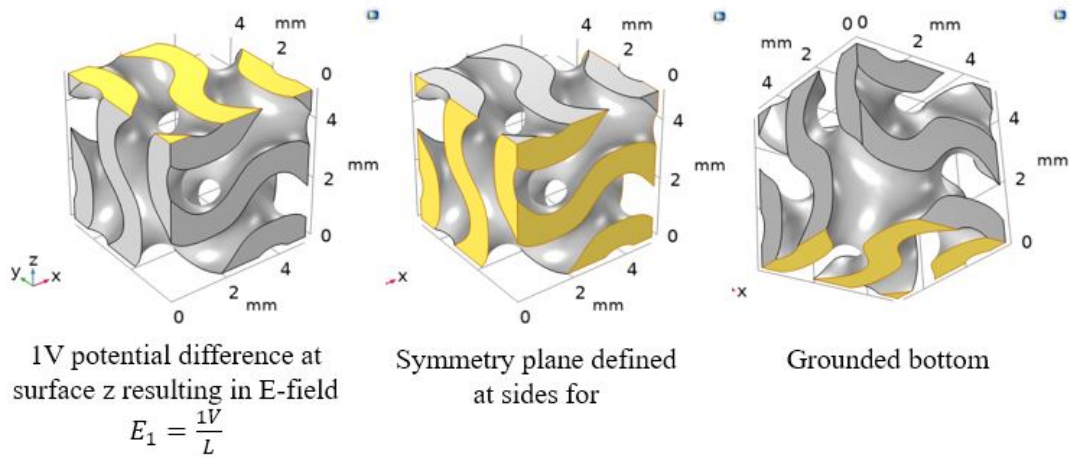
Material Property	Value	Unit
Young's Modulus	$E(\rho) = 2(0.8321 \cdot \rho^{1.784})$	MPa
Poisson's Ratio	0.49	
Density	$980\rho$	$\text{kg}/\text{m}^3$

As a second step, for the validation, earlier homogenization steps are basically followed but the prescribed displacement in the z direction is unchecked and instead the *Applied Load* function is added to apply a compressive Force at the top surface of 0.1 N magnitude to both models. A small value is used to ensure that strain is within the linear elasticity range even for smaller relative densities with less stiffness. A hexahedral mesh is used for the homogeneous cube with 0.75 mm edge length of each FE for every unit cell edge (Fig. 3.3).

### 3.1.2 Homogenization of Initial Conductivity and its Validation

In Chapter 2, the derivation of the effective initial conductivity was derived and shown to be equal to the current density on a cross-section ratio to the electric field perpendicular to the surface (Eq. 2.16). If we compare Hooke's Law to Ohm's Law, strain would be analogous to potential difference ( $\Phi$ ), and stress would be analogous to current density following a simple input-output relationship. We used this analogy to develop and compute the homogenized initial conductivity implementing the numerical homogenization procedure in COMSOL software. Another way of approaching the problem is to realize that the governing equations of electrostatics and the constitutive laws are directly analogous with heat conduction in solids characterized with thermal conductivity instead of electrical conductivity.

Figure 3.5 Boundary Conditions applied for the initial conductivity homogenization of a gyroid shown for a unit cell with 0.5 relative density



For the numerical homogenization simulation model construction in COMSOL, *Electric Currents* physics module is imported to impose the electrical governing equations and relevant boundary conditions. 1 V potential difference is applied at the top surface ( $z+$ ) using *Electric Potential* node and the bottom surface ( $z-$ ) is grounded as illustrated in (Fig. 3.5). Similar to Young's Modulus homogenization, a single unit cell with symmetry conditions on the sides is used in the model to reduce the computational load but simulate the repetition condition of numerical homogenization theory. The *intop()* function was used to calculate the total current on the surface, which is then divided to the cross-section of the unit cell cube to calculate the average current density (Eq. 3.2). Then this value is multiplied with the thickness of the unit cell, i.e. distance between the top and bottom surface, namely  $L$ . Therefore, the COMSOL equivalent of the calculation of Eq. 3.2 corresponds to

$intop(ec.Jz)/A_{surf} * L$ . Extracted values from the corresponding simulation model in COMSOL are shown in Table 4.3 in Chapter 4.

$$\sigma = \frac{intop(J_z)}{A_{surf}} \cdot \frac{\Phi}{L} \quad (3.2)$$

Same mesh of the model used for the Young's Modulus homogenization is used in the models used for the calculation of the effective conductivity (Fig.3.3). Electrical material properties of the solid material that are assigned to the model are as given in Table 3.3. Number density is driven from the electrical conductivity value of  $0.0001S/m$  based on earlier measurements (Erulker et al., 2022). The resulting effective conductivity values are fitted to a second modified SIMP function as given in Table 2.1, and imported to the homogenized cube model for its validation. Resulting values are fitted to an interpolation function,  $(\sigma(\rho) = \sigma_{0sol}(a_2 \cdot \rho_2^n + b_2))$ , using Curve Fitting application of MATLAB (Fig. 4.4

Table 3.3 Gyroid material properties: Initial conductivity homogenization

<b>Material Property</b>	<b>Value</b>	<b>Unit</b>
Electrical Conductivity	0.0001	$S/m$
Number Density	$1.3021 \cdot 10^{16}$	$1/m^3$
Relative permittivity	2.75	

Performances of 1x1x1 unit cell gyroid with 5 mm size and homogenized cube of  $5 \times 5 \times 5 \text{ mm}^3$  dimensions are compared for validation. Both have symmetry condition present for the side surfaces. First a conductive plate with 0.1 mm thickness is added to the geometry at the top. From the top of this geometry  $1A/m^2$  current is applied (Fig. 3.6). The plate is applied both to the gyroid and the homogenized cube. Bottom of the geometry is grounded, and the output voltage is measured from the top of the design space. SIMP material properties are inserted in the homogenized cube model and a parametric sweep of relative density is performed. The results will be discussed in the following chapter.

Figure 3.6 Boundary conditions of repeated gyroid (left) and cube (right) models used for Homogenized initial conductivity validation

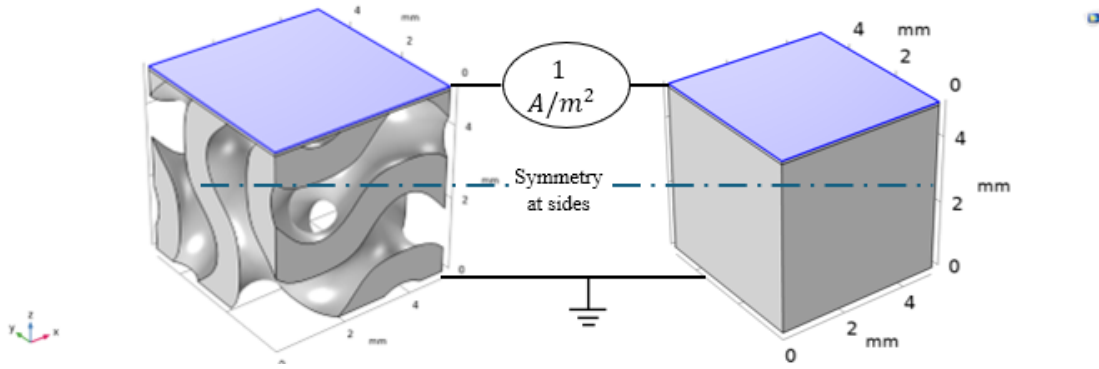


Table 3.4 Homogenized cube material properties: Validation of initial conductivity modified SIMP fit.

Material Property	Value	Unit
Electrical Conductivity	$0.0001 \cdot (0.877\rho^{1.487} + 0.65)$	$S/m$
Number Density	$1.3021 \cdot 10^{16} \cdot (0.877\rho^{1.487} + 0.65)$	$1/m^3$
Relative permittivity	2.75	

### 3.1.3 Homogenization of Elastoresistivity Component and Its Validation

To compute the homogenized elastoresistivity implementing the numerical homogenization procedure in COMSOL, we apply the combined set of the same boundary conditions applied when conducting the numerical homogenization for each property individually as discussed for the mechanical Young’s modulus and initial conductivity homogenization cases. Extraction of this material property based on a combined multi-physics model requires special care as it presents its differences from the previous homogenization calculations mainly because it cannot be formulated and therefore extracted as a model output directly but rather needs to be post-processed. Similar to initial conductivity, here we start by calculating the effective final conductivity of the model (Section 3.1.2, but unlike the effective initial conductivity that was calculated under no-strain condition, the final effective conductivity is calculated under the application of 1% strain of the single unit cell gyroid model as shown in Fig. 3.8) . Then, the change in resistivity is calculated from the difference of the initial and final conductivity values. Change in resistivity is defined as the

product of elastoresistivity component and strain (Eq. 2.21) and the equation used to extract  $m$  is given in Eq. 2.22.

For the numerical homogenization simulation model construction in COMSOL , we use *Solid Mechanics*, *Electric Currents* and *Piezoresistive Domains*, *Boundary Currents* physics altogether. The third one introduces the piezoresistivity nature displayed by a PR sensor via the coupling constitutive equation relating the former two physics. Also, under *Electric Currents*, the gyroid unit cell domain is defined as a elastoresistive material under *Current Conservation*, *Piezoresistive* node. Boundary conditions require both a 1 V potential difference and a 1% strain to be applied in the  $z$  direction from the top surface of the gyroid while keeping the bottom surface nodes fixed, i.e. a combination of the solid mechanics homogenization boundary conditions shown in Fig. 3.2 and that of the the electrical conductivity homogenization (Fig. 4.9) are applied. Similar to the initial conductivity homogenization FE model, a single unit cell gyroid model with symmetry condition on the sides is used in the model.

Results of the aforementioned model are exported to an Excel file and are used as input to a post-processing scheme to extract the desired final effective elastoresistivity values for the particular volume fraction of the simulated gyroid unit cell. The calculations necessary for the extraction of  $m$  follow mainly a 4-step procedure as follows:

1. Computation of initial conductivity  $\sigma_0$  (no-strain) and final conductivity  $\sigma_f$  (under strain loading) values for a gyroid unit cell model
2. Calculation of the absolute relative resistivity change using  $\Delta\rho = |\sigma_f^{-1} - \sigma_0^{-1}|$
3. Calculation of the absolute value of effective elastoresistivity,  $m_{latt}$ , using  $m_{latt} = \Delta\rho/\varepsilon_{11}$  with the strain value,  $\varepsilon_{11}$ , calculated as a response to the 1% strain and 1 V electric potential applied loading.
4. Calculation of the final normalized effective elastoresistivity  $m^* = m_{latt}/m_{sol}$

where  $m_{sol}$  is the elastoresistivity component of the solid material. The value for  $m_{sol}$  was taken from COMSOL's material library and corresponds to the  $m_{11}$  value for lightly doped single crystal p-silicon which is  $96 \text{ k}\Omega \cdot m$ .

Table 3.5 Gyroid material properties: Elastoresistivity homogenization

Material Property	Value	Unit
Young's Modulus	2	MPa
Poisson's Ratio	0.49	
Density	980	$\text{kg}/\text{m}^3$
Electrical Conductivity	0.0001	$\text{S}/\text{m}$
Number Density	$1.3021 \cdot 10^{16}$	$1/\text{m}^3$
Relative permittivity	2.75	
Elastoresistivity Component	96	$\text{k}\Omega \cdot \text{m}$

Performances of  $1 \times 1 \times 1$  unit cell gyroid with 5 mm size and homogenized cube of  $5 \times 5 \times 5 \text{ mm}^3$  dimensions are compared for validation. Both models includes a plate at the top to apply equal pressure on the corresponding unit cell models (Fig. 3.7). 1V is applied to the top of both unit cell models while all other boundary conditions are the as same as applied while performing the homogenization of the elastoresistivity material property. For the validation model, effective current density at the bottom of the design space is compared between gyroid unit cell and same sized homogenized cube. Mesh of the homogenized cube is the same as was used for the initial conductivity and elasticity validation studies (Fig. 3.3).

Figure 3.7 Boundary loading conditions of repeated gyroid (left) and cube (right) models used for homogenized elastoresistivity,  $m$ , validation.

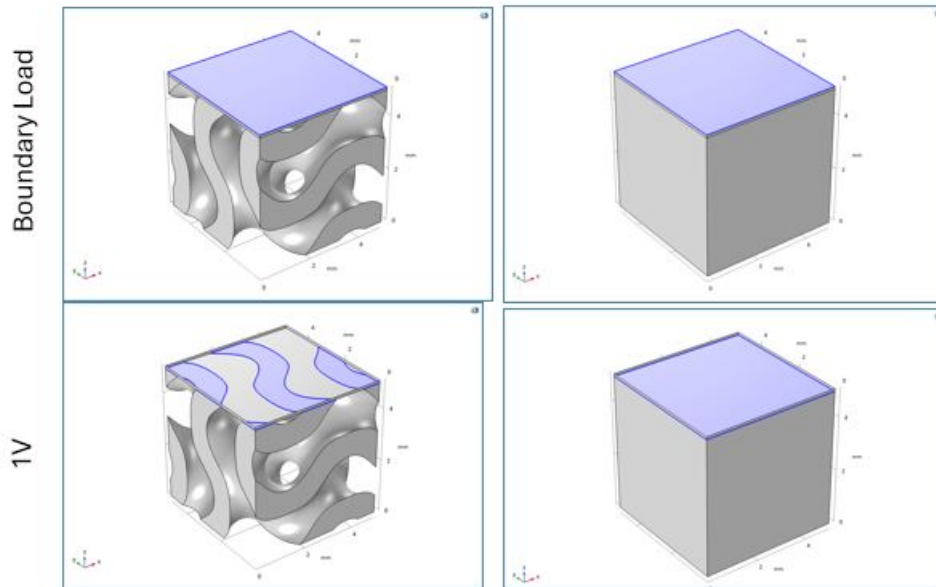
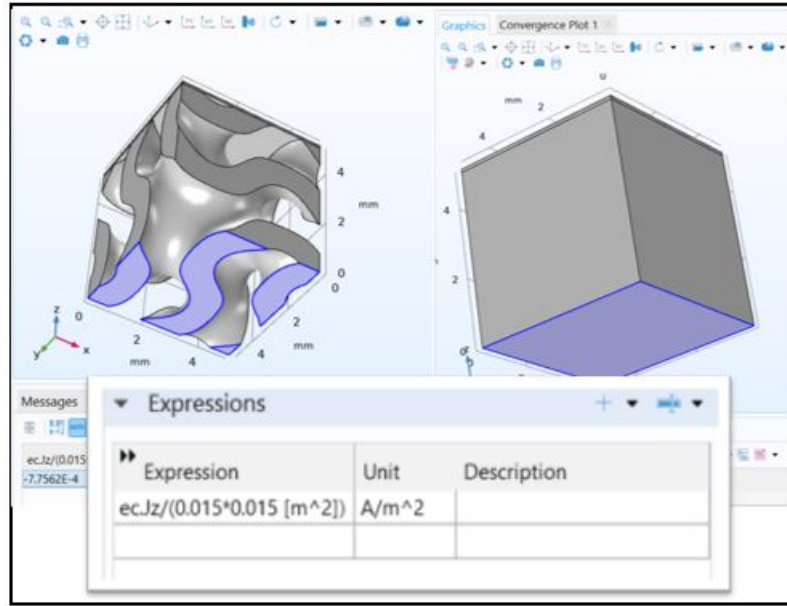


Figure 3.8 Expression and surface used in COMSOL for the effective final conductivity  $\sigma_f$  extraction of a gyroid unit cell model used for validation of the homogenized elastoresistivity,  $m$ .



### 3.2 Topology Optimization

In this section we provide the methodology and implementation details of the developed TO models which relate to the second module of the proposed TO-based design scheme shown in Fig. 3.1 which is implemented to the design of PR pressure sensor targeting maximum sensitivity. The details of the first module, where necessary material models are developed are discussed in Section 3.1.

Before running the developed TO based design framework scheme for its actual purpose of designing the sensor with respect to both the mechanical and electrical performance in an integrated multi-physics model, first the TO scheme is applied to two other problem sets where mechanical stiffness/compliance or electrical conductivity based sensitivity is targeted separately. The design steps and definition of the respective optimization models in these two categories are provided in the respective flowcharts in Fig. 3.10 and Fig. 3.12, for the mechanical compliance vs. electrical conductivity based TO sub-set of problems. Both of these design sub-problems are used as reference designs before combining the mechanical and electrical objective functions in a multi-criteria setting following the Multi-Criteria Design Optimization Flowchart in Fig. 3.14 which constitutes the third category of design case studies.

Also, the first two TO problem groups focusing on a single discipline target only and their corresponding results assisted us in the tuning of the multi-criteria optimization model as well as the interpretation of the results of the combined problem. The first problem of the TO based design focusing only on the mechanical compliance also provides a qualitative validation basis for the developed framework to be compared with one of the mechanical benchmark problems. It is also noted that the last step of the design cycle as apparent in the respective flowcharts constitute the gyroid mapping step after finding the optimal topologies in the form of optimized density distributions. Although this last step of reconstruction is needed to transform the density distributions to graded gyroid structures, it was not pursued within the scope of the thesis.

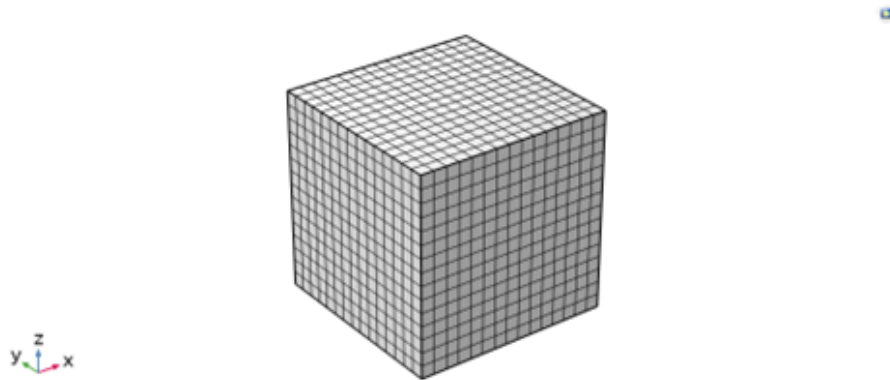
### 3.2.1 Common Properties of the Optimization Models

In all optimization models of all three design categories, the design space is defined as a  $15 \times 15 \times 15 \text{ mm}^3$  cubic design domain to represent the PR pressure sensor. As mentioned in the introduction, the decisive pressure for bedsores is 35 mmHg which is approximately 4666 Pa (Misaki et al., 2014). Consequently, the boundary load applied during optimization is 4666 Pa. The electrical boundary conditions change depending on the model, so they will be noted for every model separately. In the developed models, *Solid Mechanics*, *Electric Currents*, and *Piezoresistive Effect Domain Currents* physics are enabled via COMSOL user interface for all models to incorporate the necessary solution of the relevant governing equations for linear elasticity, electrostatics, and piezoresistive coupling, respectively because relative change in resistivity is calculated in all TO design cases even if it's not optimized for in the first or second category of the design categories. Similarly, all material properties necessary for the simulation of a pressure sensor are calculated using their corresponding modified SIMP models of all three material properties even though they are not directly linked to the optimization model's design objective or constraint.

The material properties assigned to the design space rely on the modified SIMP functions determined in the homogenization stage as presented earlier in Table 2.1. In other words, Young's Modulus, initial conductivity and elastoresistivity component depend on the relative density of the unit cells in all models. TO is implemented using the *General Optimization* module of COMSOL Multiphysics ver. 6.2 and solved using the Method of Moving Asymptotes (MMA) (Stolpe & Svanberg, 2001) and

sensitivity analysis was performed using Adjoint based sensitivity method which is available as a built-in sensitivity tool in COMSOL Multiphysics. All models are meshed using a hexahedral mesh of 4096 quadratic serendipity type elements. The design domain space of  $15 \times 15 \times 15 \text{ mm}^3$  cubic domain is divided into  $1 \times 1 \times 1 \text{ mm}^3$  FE design cells (Fig 3.9).

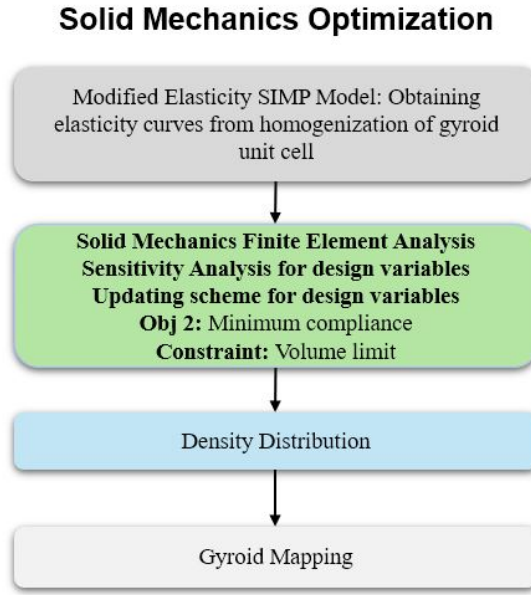
Figure 3.9 Mesh used in all Topology optimization case studies



### 3.2.2 Design Framework for Solid Mechanics Based Topology Optimization

The steps followed for the first category of design problem, namely the Solid Mechanics based TO, which is applied in this thesis to the minimum compliance of a compression cube are shown in the flowchart given in Fig. 3.10.

Figure 3.10 Design Flowchart of Solid Mechanics Based Topology Optimization



Definition of the optimization model solved for the compliance minimization is as follows:

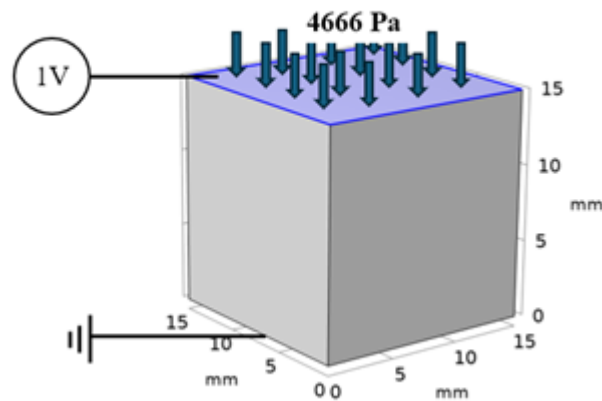
$$\begin{aligned}
 \mathbf{min.} \quad & W_s = U^T K U \\
 \mathbf{s.t.} \quad & F = K U \\
 & 0.1 < \rho_e < 0.6 \\
 & \int_{\Omega} \rho_e dV < 0.5
 \end{aligned}$$

where  $W_s$  represents the total strain energy or compliance and  $F = K U$  are the discretized system equations that are solved using FEM and represent governing equations of solid mechanics, which are assumed to obey linear elasticity.  $\rho_e$  represents the volume fraction of the  $e^{th}$  design cell and refer to the design variables of a TO problem. The integral computes the total volume of the design domain which is set in this problem to be kept below 50 % of the entire total volume. The relative density lower and upper bounds are set to 0.1 and 0.6, respectively.

It is noted that in addition to the pressure applied to the pressure sensor model that the solution of the system equations are based on in conducting the compliance based TO, a potential excitation of 1V is applied to the top of the sensor model surface keeping the bottom surface grounded (Fig. 3.11). All materials that comprise the design space are defined as a piezoresistive material even though the mechanical property is the only material property that is optimized for in the solid mechanics based TO problem using the calculated modified SIMP based material model for Young's modulus via homogenization as discussed in Section 3.1.1. The piezoresistive material assignment is necessary to model the pressure sensor and to evaluate

the piezoresistive behavior in terms of its electrical performance for varying material distributions that the compliance based TO problem will result in. For the sake of this evaluation, it is noted that the initial design of a homogeneous cube with 0.5 volume fraction yields an initial reference value of relative change in resistivity of 4.81%.

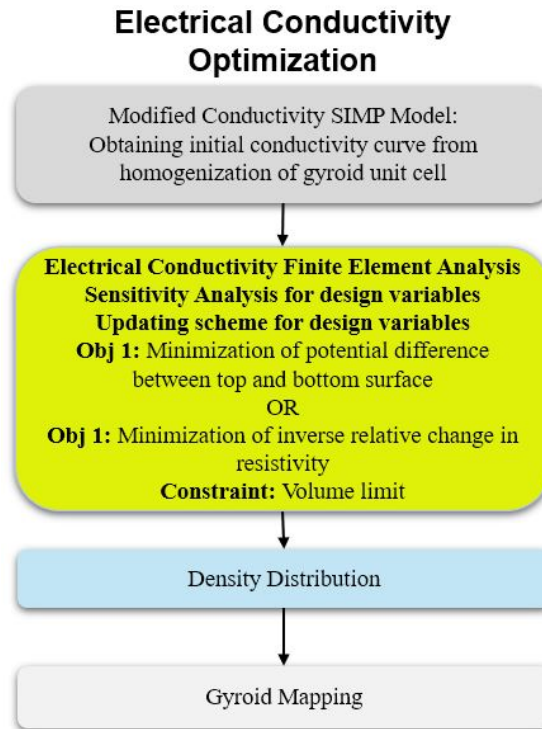
Figure 3.11 Boundary conditions applied on design domain used for solid mechanics based TO case study targeting minimum compliance



### 3.2.3 Design Framework for Electrical Conductivity Based Topology Optimization

The steps followed for the second category of design problems, namely the electrical conductivity based TO, which is applied in this thesis targeting maximum sensitivity via different optimization models are shown in the flowchart given in Fig. 3.12.

Figure 3.12 Design Flowchart used for Electrical Conductivity based Topology Optimization Studies



Compliance optimization problem is one of the mostly studied structural optimization problems in literature, and therefore the model definition with appropriate application of boundary conditions and the definition of a suitable objective function as well as implementation is straightforward. However, topology optimization of 3D piezoresistive pressure sensors remain relatively unexplored as discussed in Chapter 1. In this section, we first adopt the TO using different objective functions for getting the best sensitivity (Table 3.6) and later in the next section integrate it to target improvements in both the solid mechanics as well as electrical sensitivity behavior. Here, we use the modified SIMP model for (initial) conductivity with relative density values of design cells restricted to the working range of  $\rho = 0.1$  to  $\rho = 0.6$ . These bounds apply to all case studies presented in all three categories to which the graded TO framework was applied. Also, Hooke's Law and Ohm's law are used for modeling all case studies listed in this second category here for electrical conductivity based TO. In Chapter 4, we present and compare their resulting change in relative resistivity values of all case studies.

A total of 3 case studies are conducted in this category. For the case study 1, the objective was to minimize the final potential difference between the bottom ground and the top plane comprising the sensor (Fig. 3.13). For increasing sensitivity, conductivity must be as high as possible. Therefore, minimizing the potential difference

between the plates is one way to achieve maximum sensitivity. Since the potential difference is targeted, the model is excited with a  $1 A/m^2$  current density applied from the top surface, rather than the application of the electric potential. The bottom is grounded, and similar to the problem presented in the first category of the minimum compliance problem, 4666 Pa pressure is applied from the top. Total average volume is constrained to 0.5 of the total volume.

The objective function of case study 2 is more intuitive. The actual target of maximum sensitivity is defined directly as the objective function. Namely, the inverse of change in relative resistivity is set to be minimized. In this case study, similar to the models used for numerical homogenization of conductivity, a potential of 1V is applied from the top, and the bottom is grounded. Finally, for the case study 3, the electric potential at the top surface is assigned a  $1 A/m^2$  current density excitation similar to the boundary loading condition of case study 1.

Figure 3.13 Boundary Conditions applied on design domain used for electrical conductivity based TO case study 1 and 3 (left) and case study 2 (right)

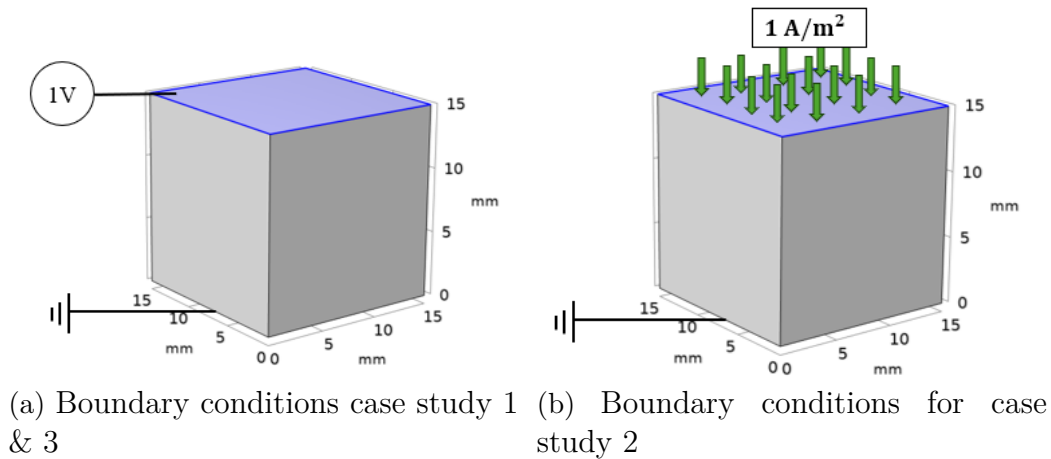


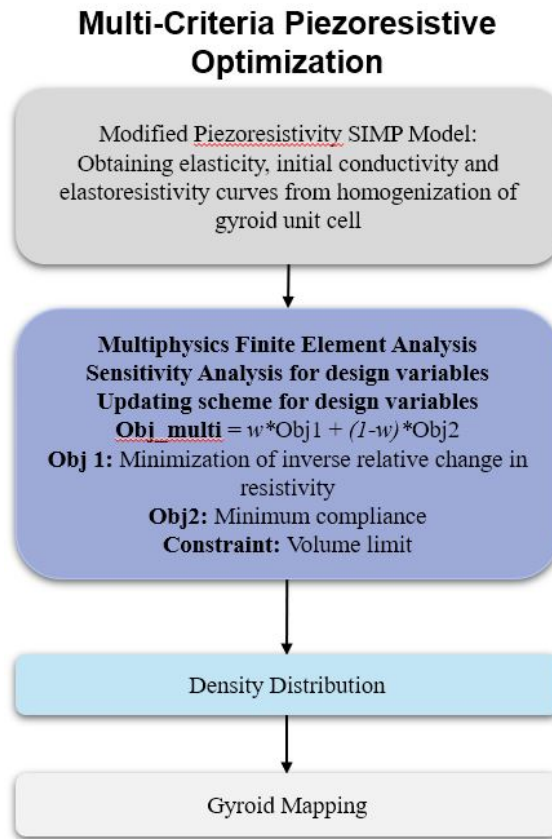
Table 3.6 Properties and objective functions of electrical conductivity based TO cases targeting maximum sensitivity

Case Study No.	Objective function	Objective function type	Boundary Conditions
1	Min. $\Phi_{top} - \Phi_{top}$	Global	$1A/m^2$ at top
2	Min. $\rho_0/\Delta\rho$	Integral	1V at top
3	Min. $\Phi_{top} - \Phi_{top}$	Global	$1A/m^2$ at top

For the sake of further evaluation to be carried out in Chapter 4, it is noted that the initial design of a homogeneous cube with 0.6 volume fraction yields an initial reference value of relative change in resistivity of 3.78%.

### 3.2.4 Design Framework for Piezoresistivity based Multi-Criteria Topology Optimization

Figure 3.14 Design Flowchart for Piezoresistivity Based Multi-Criteria Topology Optimization Studies



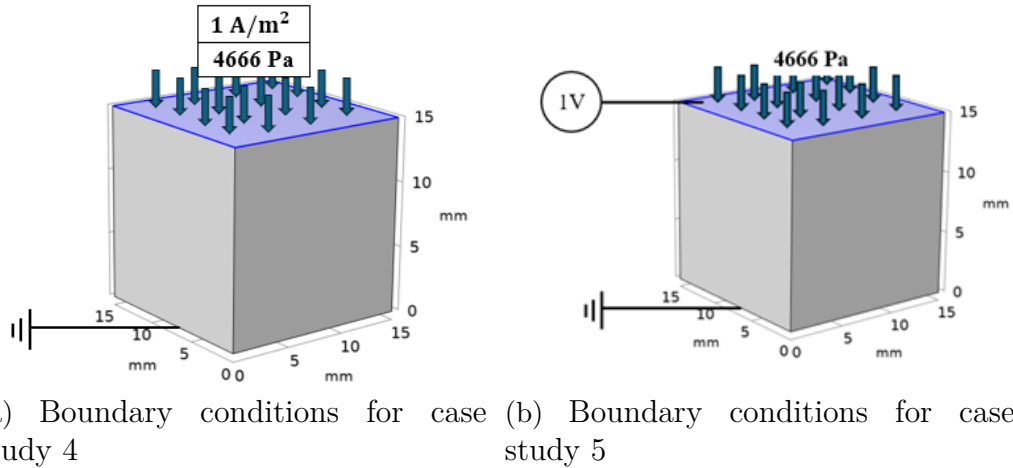
In order to design a sensor with maximum sensitivity performance, we mainly try to redistribute the material topology to increase relative change in resistivity at the pressure value that the sensor will work at. Relying only on an optimization model incorporating only its electrical performance, i.e. the sensitivity may lead to designs that present itself with no structural integrity nor the desired deformability of the sensor which are inherently linked to the mechanical performance of the deformable sensor. Therefore, in the third category of the TO case studies we focus on the multi-physics design requirements (Fig. 3.14, rather than a single objective pursued in the previous two categories. Towards that objective, we adopt the TO based design framework towards a multi-objective optimization model. Influenced by existing work and its well-defined TO settings and solutions, we chose to keep the mechanical design counterpart as the structural stiffness requirement of the sensor that is defined with a well-known objective function for minimization of total strain energy. Other alternatives such as required total displacement of minimum stiffness

to achieve the maximum deformation ability of the sensor could be applied but is not pursued here mainly to keep the focus of thesis on the piezoresistivity of the sensor which constitutes the novelty of the thesis. Also, the choice of a PDMS material for the sensor with a relatively low Young's modulus should allow for the desired deformability behavior for the target application of bedsores detection.

Table 3.7 Boundary conditions and objective functions of piezoresistivity based multi-criteria TO cases

Case Study No.	Mechanical Objective Function	Electrical Objective Function	Boundary Condition
4	Min. $U^T KU$	Min. $\Phi_{top} - \Phi_{bottom}$	$1 A/m^2$ at top
5	Min. $U^T KU$	Min. $\rho/\Delta\rho$	$1 V$ at top

Figure 3.15 Boundary conditions applied on the design domain used for multi-criteria based TO case study 4 (left) and case study 5 (right)



For the first problem in this category, referred to as case study 4, the objective function responsible of the desired electrical performance is chosen to be the potential difference. Potential difference and the integral of strain energy density are defined as separate global objective functions under *General Optimization* (Fig. 3.16) because potential difference itself is the function of choice to be minimized, whereas strain energy density needs to be integrated over the design domain to evaluate the total strain energy that is set as the mechanical objective function to be minimized. Instead of a multi-objective optimization study, for all case studies presented, the weighted sum approach is used for the solution of an equivalent single objective optimization model. That is both objective functions are summed to define the resulting aggregate objective function which is implemented in COMSOL under the

Study tool by choosing “Minimization” for the Type and “Sum of objectives” for Solution as shown in Fig 3.17.

Figure 3.16 Screenshot of objective function definitions in the multi-criteria based TO case studies using global objective feature of the general optimization module in COMSOL.

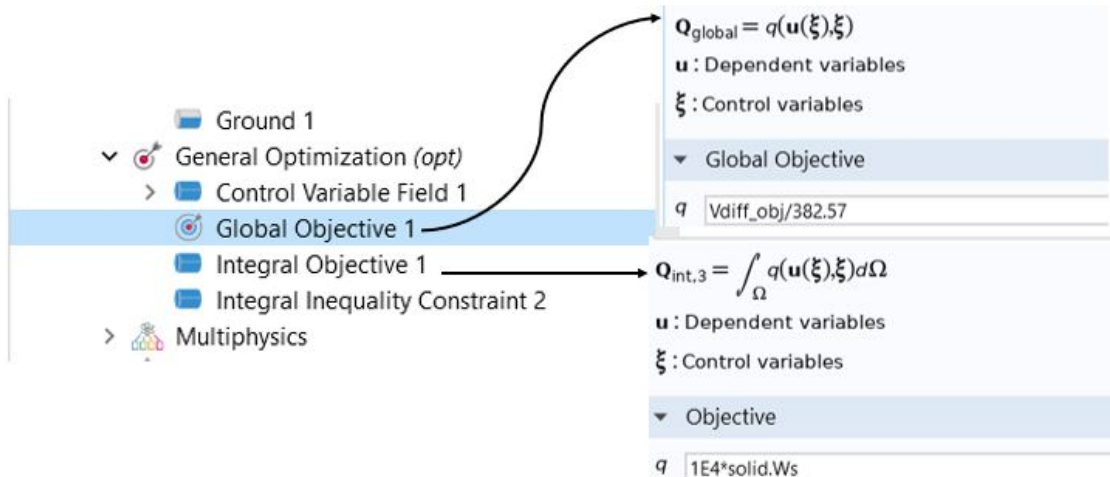
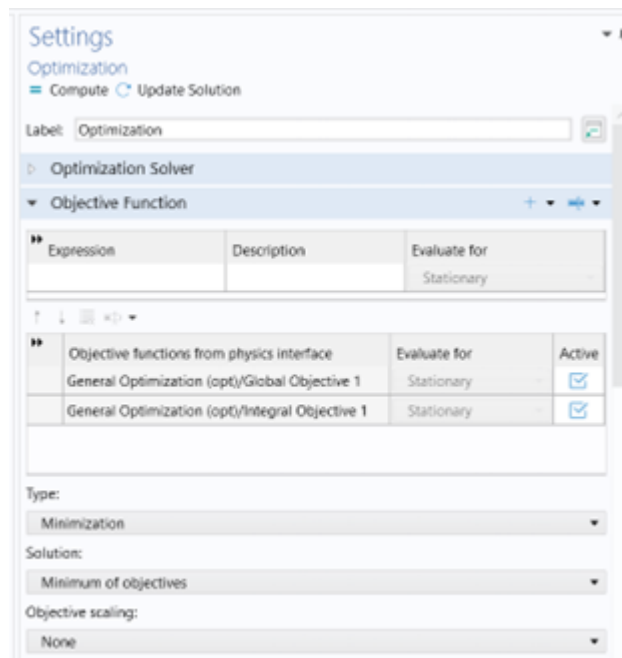


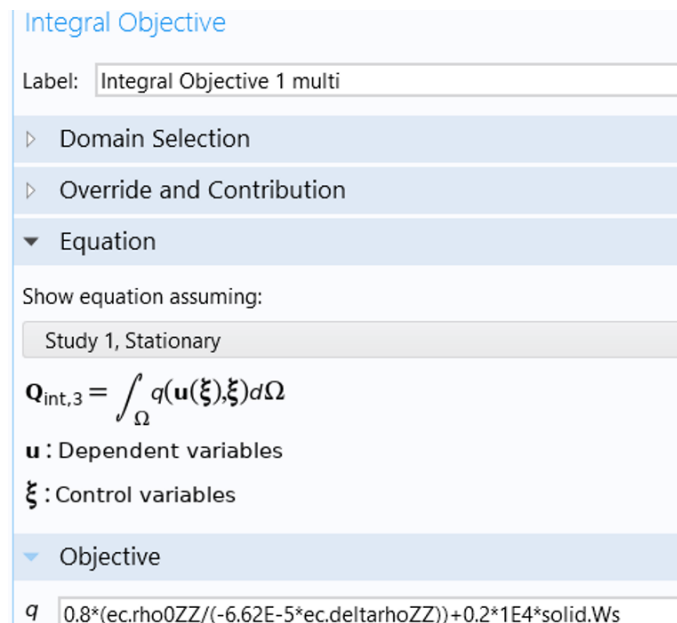
Figure 3.17 Screenshot of optimization Settings used in the multi-criteria based TO case studies using global objective feature of the general optimization module in COMSOL.



In the second model presented within the third category of the multi-physics TO framework, referred to as the case study 5, one of the objective functions is defined

as  $\rho_0/\Delta\rho$  and the second refers to the integral of the strain energy density ( $U^T KU$ ). Since both elements are integrated, they are combined under a single Integral Objective definition in the General Optimization module available in COMSOL (Fig. 3.18). The first trial of equal weighted objective functions prompted for the mechanical component dominantly governing the optimization solution. Therefore, the objective function representing the electrical performance was assigned a higher value to its weight in the weighted sum of the single objective model. More specifically, for the case study 5, for which the results are presented in Chapter 4, the electrical objective function weighting function was assigned as 0.8 compared to its mechanical counterpart which was assigned a weighting function of 0.2. Fig. 4.23 shows the results of case study 5 with a multi-criteria function defined as  $0.8 \cdot \rho_0/\Delta\rho + 0.2 \cdot U^T KU$ . Due to space limitations, results of optimization models with different objective function weights are shown in Appendix .2 shows. Additionally, to prevent the model from converging to design solutions demanding completely closed or too thin gyroid equivalents in the reconstruction step not performed in this thesis, the relative density values of FE cells were restricted between 0.3 and 0.6 and the total volume constraint was limited by 30% at the lower limit and 60 % at the upper limit.

Figure 3.18 Screenshot of the weighted multi-criteria function definition in the multi-criteria based TO case studies using the integral objective feature of the general optimization module in COMSOL.



## 4. Results and Discussion

In this chapter results of the numerical simulation studies are presented and discussed first for the numerical homogenization of all three material properties with their corresponding validation studies. Next topology optimization design results are presented for the following case studies:

1. Case: Solid mechanics based TO, minimum compliance of a compression cube
2. Case 1: Electrical conductivity based TO targeting maximum sensitivity with objective of minimum potential difference
3. Case 2: Electrical conductivity based TO targeting maximum sensitivity with objective of minimum total inverse relative change in resistivity with electrical potential boundary condition
4. Case 3: Electrical conductivity based TO targeting maximum sensitivity with objective of minimum total inverse relative change in resistivity with current density boundary condition
5. Case 4: Multi-criteria optimization with compliance and potential difference as the optimization criteria
6. Case 5: Multi-criteria optimization with compliance and total inverse relative change in resistivity as the optimization criteria

All simulations were run on a Intel Xeon workstation with 128 GB RAM and dual Gold 6136 processor of 3GHz CPU.

## 4.1 Results of Homogenization Models and Validations

### 4.1.1 SIMP Model and Validation of Young's Modulus

The results for Young's Modulus homogenization are listed in Table 4.1. The extracted stiffness matrix components  $C_{11}$  and  $C_{12}$ , and calculated effective Young's Modulus,  $E_{latt}$ , and the corresponding normalized effective Young's Modulus  $E^*$  values are also given.

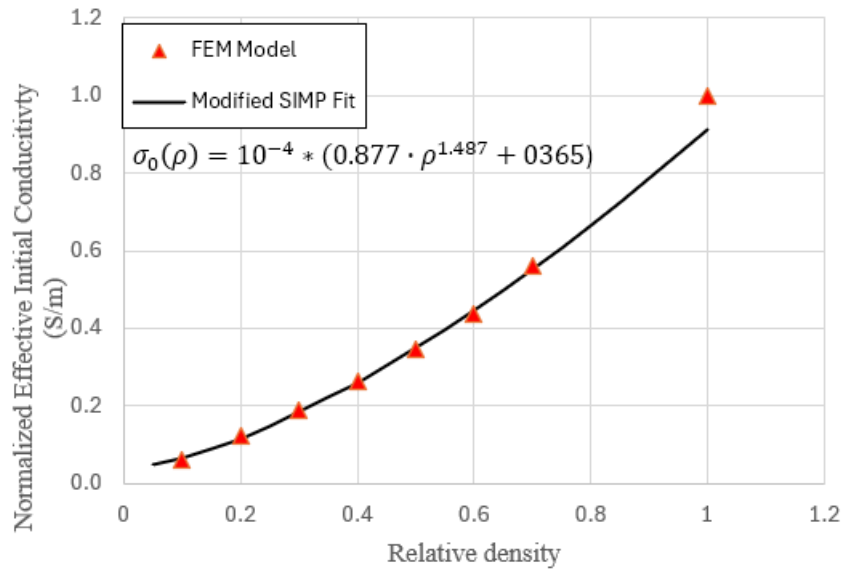
Table 4.1 Homogenized Young's modulus results of fitted modified SIMP function and comparison with calculated FE model value of gyroid unit cell

<b>Volume Fraction</b>	$C_{11}$ (Pa)	$C_{12}$ (Pa)	$E_{latt}$ (Pa)	$E^* = E_{latt}/E_{sol}$	<b>Fit Function</b>	<b>Error (%)</b>
<b>0.1</b>	0.0772	0.0369	0.0533	0.0267	0.0150	43.64
<b>0.2</b>	0.1757	0.0912	0.1133	0.0567	0.0503	11.23
<b>0.3</b>	0.3297	0.1672	0.2171	0.1086	0.1020	6.036
<b>0.4</b>	0.5140	0.2661	0.3325	0.1663	0.1684	1.310
<b>0.5</b>	0.7600	0.4083	0.4747	0.2373	0.2485	4.719
<b>0.6</b>	1.1411	0.6501	0.6692	0.3346	0.3415	2.076
<b>0.7</b>	1.7559	1.1128	0.8926	0.4463	0.4468	0.121

The resulting interpolation resulted in the modified SIMP model  $E(\rho_e) = 0.83213 \cdot \rho_e^{1.7434}$  for the calculation of the normalized Young's modulus scaled with the solid material's Young's Modulus,  $E_{sol}$ , with a value of 2 MPa. Fig. 4.1 shows the fitted function and the values as calculated by the FEM model that were used in fitting the function. The error is calculated using the relative percentage error definition. The fitted function closely follow simulated data with an average error of 4% but the relative volume fraction of 0.1 point is an outlier and therefore was not included in the total average error computation. The lower limit of a very thin gyroid with 0.1 relative density has a comparatively higher error which is intuitively expected as thinner curved structures present a meshing challenge when compared to their thicker, higher volume fraction counterparts. This is reflected on the validation results in Fig. 4.2, too. It is noted that the model used is a single unit cell and the imported gyroid model was created with a mesh density of 25866 in MATLAB. Model specific statistics regarding the mesh density used in MATLAB for the CAD

generation as well FEM mesh data and simulation time data of used models are provided in the Appendix .3 (Table .3.1). The rule of thumb for TPMS meshing is that there should be as least three elements across the thinnest walls of the gyroid model. This was not always possible for the models simulated due to hardware limitations, and hence a possible source for a higher relative error. Also, even though symmetry condition is used, analysis of higher number of unit cell repetitions with possibly a higher FE mesh is expected to give more accurate results.

Figure 4.1 Fitted modified SIMP function for Young’s modulus: normalized effective Young’s modulus vs. relative density under 1% strain.



The modified Young’s Modulus evaluated based on the fitted SIMP model and other material properties such as Poisson’s ratio and density are inserted to the homogenized cube model to be compared with the repeated gyroid unit cell model (Table 3.2. Average values of the displacement along z of the top surface where the load is applied are compared. The resulting numerical comparison is provided in detail in Table 4.2 and the corresponding 3D colour coded displacement distributions are shown comparatively in Fig. 4.3 for a gyroid and homogenized cube of 0.5 relative density. The results show an average total error of 15%, which decreases to 8% with the outlier point of relative density of 0.1 excluded.

Figure 4.2 Validation results of homogenized Young's modulus: Displacement (y axis) of 3x3x3 gyroid unit cell with different relative density (x axis) vs. homogenized cube with fitted Young's modulus value under 1 N load.

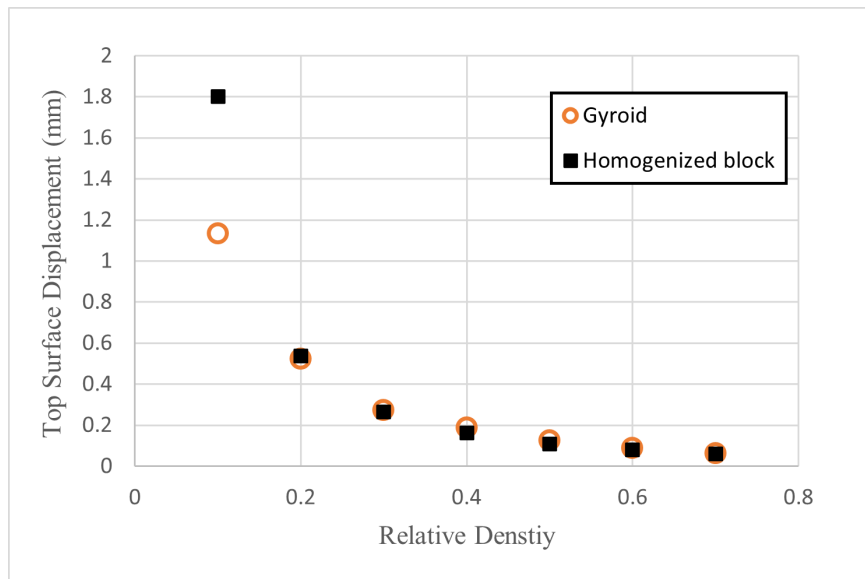
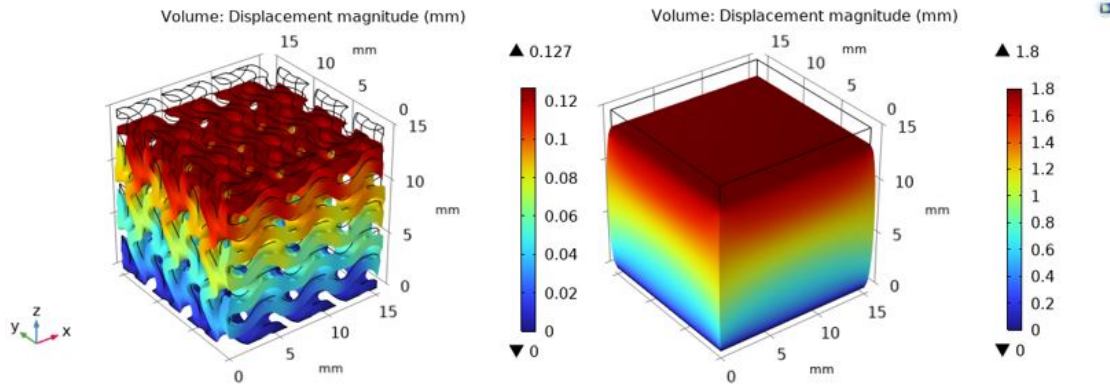


Table 4.2 Top surface z-displacement values of 3x3x3 gyroid unit cell (gyroid) vs. its equivalent homogenized cube model under 1 N load.

<b>VF</b>	<b>Gyroid (mm)</b>	<b>Homogenized cube (mm)</b>	<b>Error (%)</b>
<b>0.1</b>	1.1331	1.8011	58.95
<b>0.2</b>	0.52341	0.53792	2.77
<b>0.3</b>	0.2717	0.26529	2.36
<b>0.4</b>	0.18725	0.16066	14.20
<b>0.5</b>	0.1257	0.10888	13.38
<b>0.6</b>	0.089149	0.079233	11.12
<b>0.7</b>	0.063265	0.060561	4.27

Figure 4.3 Validation of homogenized Young's modulus: displacement distribution (mm) response of 3x3x3 gyroid unit cell (left) and its equivalent homogenized cube (right) under 1N load .



#### 4.1.2 SIMP Model and Validation of Initial Conductivity

Similar to the homogenization of Young's modulus, results for numerical homogenization of the initial conductivity property for different volume fractions are presented here. The resulting homogenized conductivity values  $\sigma_{latt}$  are provided in Table 4.3. Also, the normalized homogenized conductivities,  $\sigma^*$  as well as the error between the fitted function to these values and the relative error of the fitted function value are tabulated. Overall average error of the interpolation is about 5% with outlier trends at the limits of the volume fraction range of 0.1 and 0.7 relative densities, respectively. Similar to the thinnest gyroid mode with volume fraction of 0.1, 0.7 represents the thickest gyroid which geometrically is the limiting point where the surfaces start to close-up due to too thick walls of the lattice geometry. Hence, the relative larger errors of too thin and thick gyroids are numerically expected presenting meshing challenges and hence induce less computational accuracy but could be further improved which is limited by the available computational power of the workstation used for the analysis and the computational time.

Table 4.3 Homogenized initial conductivity results of fitted modified SIMP function and comparison with calculated FE model value of gyroid unit cell under 1V electrical load

<b>VF</b>	$\sigma_{latt}$ (S/m)	$\sigma^* = \sigma_{latt}/\sigma_{sol}$ (S/m)	<b>Fit Function</b>	<b>Error</b> (%)
0.1	5.88E-06	0.0588	0.06511	10.6455
0.2	1.22E-05	0.1223	0.1166	-4.6119
0.3	1.89E-05	0.1891	0.1829	-3.2812
0.4	2.63E-05	0.2626	0.2610	-0.6196
0.5	3.45E-05	0.3446	0.3493	1.3701
0.6	4.36E-05	0.4364	0.4468	2.3658
0.7	5.61E-05	0.5608	0.5520	-1.4846
1	1.00E-04	1.0000	0.9133	-8.6660

Similar to the Young's modulus, calculated normalized homogenized conductivities,  $\sigma^*$  are used to construct a modified SIMP function using MATLAB's curve fitting application (Fig. 4.4). The same fitting application was used for all curve fitting applications in the thesis. One and two term power laws are tested in the application and two term power law was found to have a higher  $R^2$  value, hence the resulting fit was chosen.

Figure 4.4 Screenshot of the MATLAB's curve fitting application used for the construction of the modified SIMP model, shown for conductivity  $\sigma$

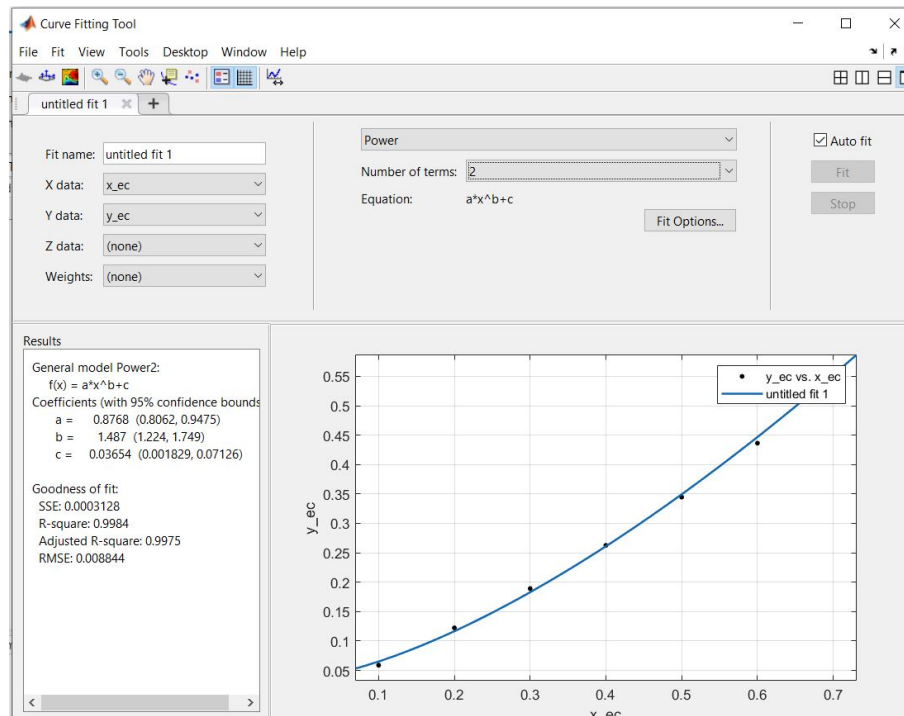
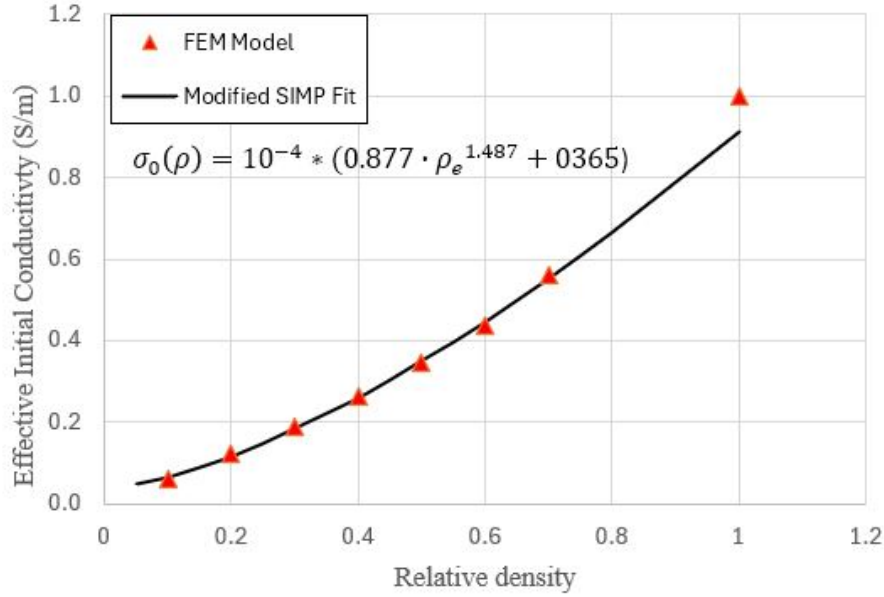


Figure 4.5 Fitted modified SIMP function for initial conductivity: normalized effective initial conductivity (y-axis) vs. relative density (x-axis).



The resulting normalized fitted function is of the following form:  $\sigma_0(\rho) = 0.8768 \cdot \rho^{1.487} + 0.03654$ .

To validate the resulting modified SIMP model, the modified initial conductivity evaluated based on this fitted SIMP model and other material properties such as number density, and electrical permittivity are inserted to the homogenized cube model to be compared with the repeated gyroid unit cell model (Fig. 3.4). Average potential values on the top surface,  $\Phi$ , where  $1A/m^2$  of current density is applied are compared. The resulting numerical comparison is provided in detail in Table 4.4, with the functional plot comparison in Fig.4.6 and the corresponding 3D colour coded voltage distributions are shown comparatively in 4.7 for a gyroid and homogenized cube of 0.5 relative density. The results show an average total error of 6.96% and a standard deviation of 4.9% in the respective potential performance, with individual relative errors mostly below under 10% for most relative density values proving that the derived modified SIMP model is suitable to represent effective initial conductivities for gyroids of different volume fractions with reasonable accuracy.

Table 4.4 Top surface potential values  $\Phi(V)$  of  $3 \times 3 \times 3$  gyroid unit cell (gyroid) vs. its equivalent homogenized cube model under  $1A/m^2$  current density load

<b>VF</b>	$\Phi_{gyroid}(V)$	$\Phi_{h.cube}(V)$	<b>Error (%)</b>
0.1	930.87	767.94	17.50
0.2	422.67	428.74	1.436
0.3	255.68	273.39	6.927
0.4	184.74	191.56	3.692
0.5	157.15	143.13	8.921
0.6	119.87	111.92	6.632
0.7	87.472	90.508	3.471

Figure 4.6 Validation of homogenized initial conductivity: Average potential (y axis) of repeated gyroid model with different relative density (x axis) vs. homogenized cube with fitted initial conductivity value.

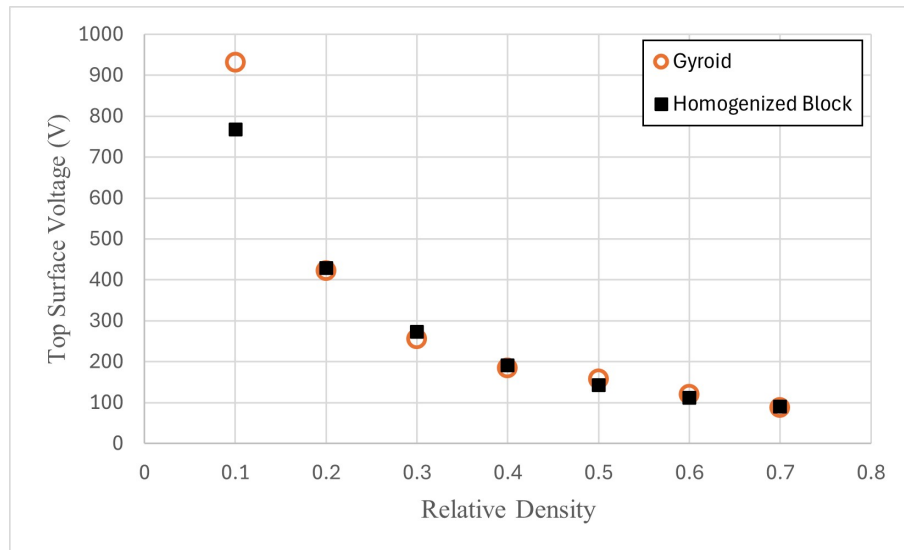
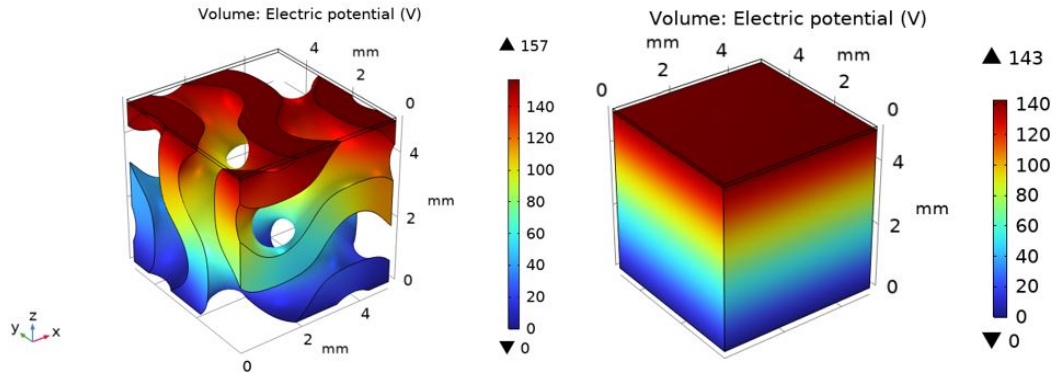


Figure 4.7 Validation of homogenized initial conductivity:electric potential (V) response of 3x3x3 gyroid unit cell (left) and its equivalent homogenized cube under  $1A/m^2$  current density load(right).



#### 4.1.3 SIMP Model and Validation of Elastoresistivity

The homogenization of elastoresistivity material property results follow a similar procedure carried out for Young's modulus and initial conductivity. Per the implementation details in Section 3.1.3, elastoresistivity homogenization simulations are carried out on a multi-physics model solving for both the mechanical as well as the electrical response under applied loading and piezoresistive material coupling of the considered unit cell model, i.e. either the gyroid or the homogenized cube model used for validation. This procedure calls for the calculation of the electrical response under no loading and the calculation of initial conductivities  $\sigma_{latt,0}$ , as well as the electrical response under unit strain,  $\sigma_{latt,F}$ . Using resulting conductivity values, based on the difference of their inverse,  $(\sigma_{latt,F}^{-1} - \sigma_{latt,0}^{-1})$ , the effective resistivity difference is calculated as  $\Delta\rho$ . Finally, the effective elastoresistivity,  $m$ , is calculated based on the ratio with this property and the strain value,  $\varepsilon$ , calculated as a response to the 1% strain and 1 V electric potential applied from the top surface ( $z+$ ) while the bottom ( $z-$ ) is grounded and fixed. All these relevant quantities are needed for the evaluation of the final effective normalized elastoresistivity magnitude,  $|m^*|$  and are given in Table 4.5. Next, the homogenized data is fit to a function of the form  $m(\rho) = a \cdot \rho^n + b$  and the resulting fitted function is shown in Fig. 4.8.

Also, the effective normalized elastoresistivity,  $m^*$ , as well as the the relative error of the fitted function value are tabulated in Table 4.6. Overall, it is observed that the fitted function follows the data of the corresponding homogenization results of the FE gyroid model well. The fit function error is below 5% except 0.5 and 0.6 relative

densities where the error is calculated to be around 13% (Table 4.6). The points with values per the FE model calculated data are observed to fall slightly below the fitted curve data. It can be argued that either there is an accuracy related simulation uncertainty in these specific cases, which is likely since we expect the data to fit power law in the case of TPMS lattices, or else a different interpolation function such as a quadratic fit could reduce the error and track the data values at these points with a better accuracy. The validation results showed reasonably small overall errors as will be discussed next, therefore we chose to continue with the power fit which is also more suitable for the TO based on a modified power law in the case of graded TPMS unit cell geometries as was discussed earlier in Chapter 2.

Table 4.5 Homogenized elastoresistivity results: Effective normalized elastoresistivity,  $m^*$ , unscaled elastoresistivity,  $m$ , calculated based on related electrical response parameters: initial conductivity under no loading  $\sigma_{latt,0}$  and under unit strain,  $\sigma_{latt,F}$  for different volume fractions, VF

<b>VF</b>	$\sigma_{latt,F}$ (S/m)	$\sigma_{latt,0}$ (S/m)	$\Delta\rho =  \sigma_F^{-1} - \sigma_0^{-1} $ ( $\Omega \cdot m$ )	$m = \Delta\rho/\varepsilon$ ( $\Omega$ )	$m^*$ ( $\Omega$ )
<b>0.1</b>	5.965E-06	5.88E-06	2293.38	229338	2.3889
<b>0.2</b>	1.242E-05	1.22E-05	1284.08	128408	1.3376
<b>0.3</b>	1.931E-05	1.89E-05	1098.23	109823	1.1440
<b>0.4</b>	2.695E-05	2.63E-05	970.56	97055	1.0110
<b>0.5</b>	3.450E-05	3.45E-05	794.39	79439	0.8275
<b>0.6</b>	4.511E-05	4.36E-05	746.62	74662	0.7777
<b>0.7</b>	5.894E-05	5.61E-05	867.40	86740	0.9035
<b>1.0</b>	1.106E-04	1.00E-04	958.41	95841	0.9983

To validate the resulting modified SIMP model, the modified elastoresistivity evaluated based on this fitted SIMP model and other material properties such as Young's modulus and initial conductivity are inserted to the homogenized cube model to be compared with the repeated gyroid unit cell model. Average potential current density values on the bottom surface,  $J^*(A/m^2)$  are extracted while 1V of potential is applied to the opposing top surface and compared under constant pressure of 4666 Pa application. The resulting numerical comparison is provided in detail in Table 4.6, with the functional plot comparison in Fig.4.9) for a gyroid and homogenized cube of 0.5 relative density.

The results show an average total error of 2.72% and a standard deviation of 1.93% in the respective current density performance, with individual relative errors all below under 10% for all relative density values proving that the derived modified

SIMP model is suitable to represent effective elastoresistivities for gyroids of different volume fractions with reasonable accuracy.

Figure 4.8 Fitted modified SIMP function for elastoresistivity component: effective elastoresistivity component magnitude (y-axis) vs. relative density (x-axis)

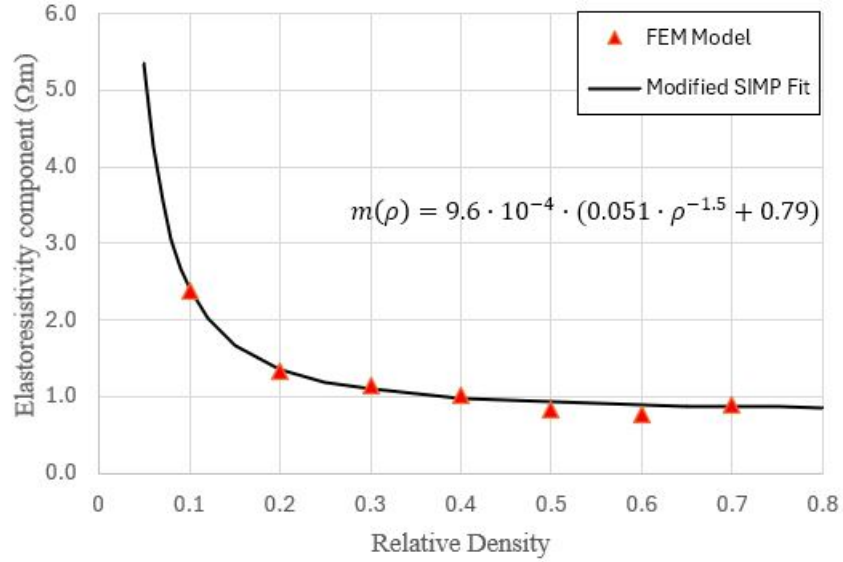
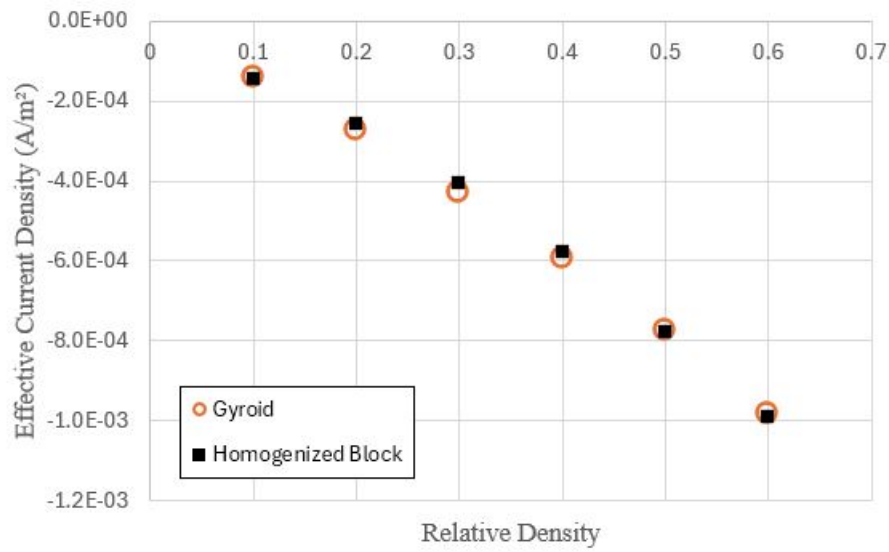


Table 4.6 Effective current density  $J^*$  on the bottom plane of single gyroid unit cell with symmetry vs. its equivalent homogenized cube model under 1V potential and 4666 Pa loading

VF	$m^*$	Fit Function	Error ( %)	$J^*_{gyroid}(A/m^2)$	$J^*_{h.cube}(A/m^2)$	Error ( %)
0.1	2.388	2.402	0.539	-1.42E-04	-1.45E-04	2.05
0.2	1.337	1.357	1.471	-2.72E-04	-2.59E-04	4.71
0.3	1.143	1.097	4.098	-4.31E-04	-4.06E-04	5.70
0.4	1.011	0.988	2.252	-5.96E-04	-5.80E-04	2.67
0.5	0.827	0.931	12.49	-7.76E-045	-7.79E-04	0.39
0.6	0.778	0.896	15.24	-9.85E-04	-9.93E-04	0.82
0.7	0.904	0.874	3.308	-	-	-

Figure 4.9 Validation of homogenized elastoresistivity component: Current density (y axis) of repeated gyroid model with different relative density (x axis) vs. homogenized cube with fitted elastoresistivity component value.

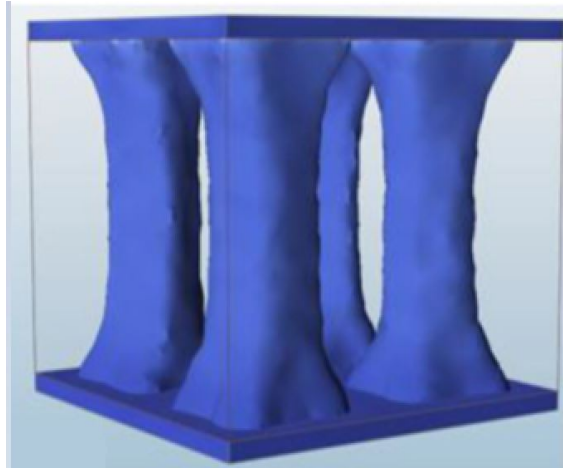


## 4.2 Solid Mechanics Based TO: Minimum Compliance of a Compression

### Cube

As the first example, we apply the developed design framework to a solid mechanics design problem following Fig. 3.10 and present results for the minimum compliance TO problem that corresponds to a well-known benchmark problem (Saadlaoui et al., 2017) with results shown in Fig. 4.10.

Figure 4.10 Design results given by Saadlaoui et al. (2017) for the minimization of compliance problem of a compression cube



A four-legged structure is the result of the benchmark study of a metal cube subjected to a given pressure solved using compliance optimization in COMSOL. Here, we used the modified SIMP model instead of the standard SIMP model and adapted the problem to the material parameters chosen for the pressure sensor. As expected, the TO problem converges in 49 iterations to the results given in Fig.4.11 following the convergence history shown in Fig.4.13, attaining a minimum strain energy density value of  $6.25 \cdot 10^{-5} J/m^3$  attaining the given volume constraint of 0.5. The resulting legs, evident in the resulting optimized relative density distribution of the compression cube, are not as distinct as the results of standard optimization models in literature. However, the resulting topology are similar to the expected solution given the differences of the loading, material properties referring to a softer material of PDMS, the use of a modified SIMP model as well as different upper and lower limits and the modeling differences related to the mesh and element types used here in COMSOL vs. the reference study simulated in Hypermesh Optistruct software.

Figure 4.11 Design results obtained for the minimization of compliance problem of a compression cube: displacement (top left), Young's modulus (top right), strain energy density (lower left) and resistivity change in z direction (lower right). Units are shown in corresponding colour bars

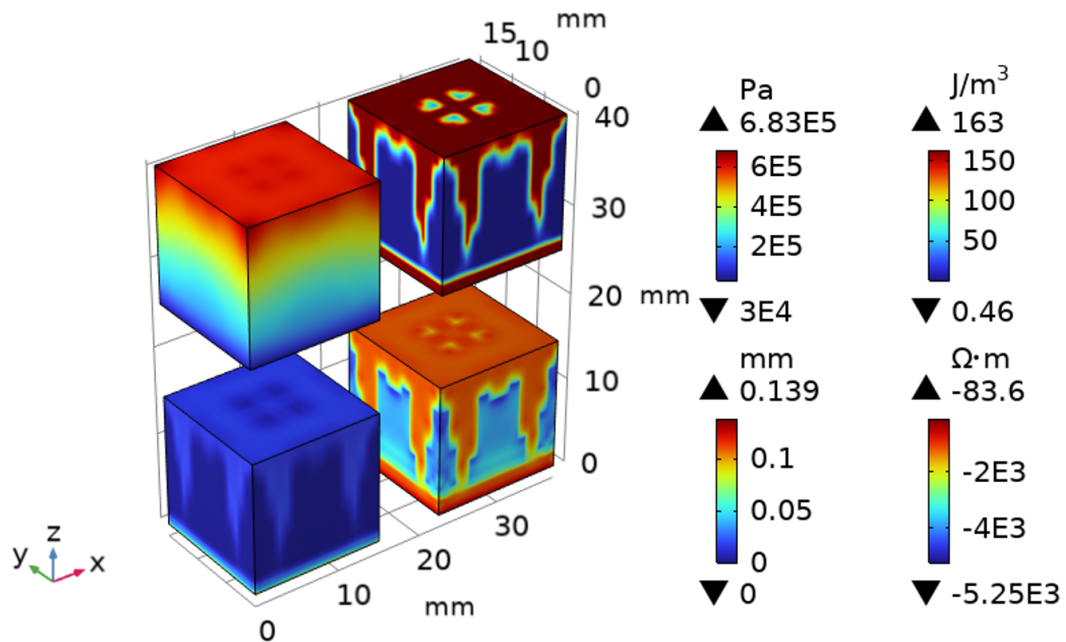
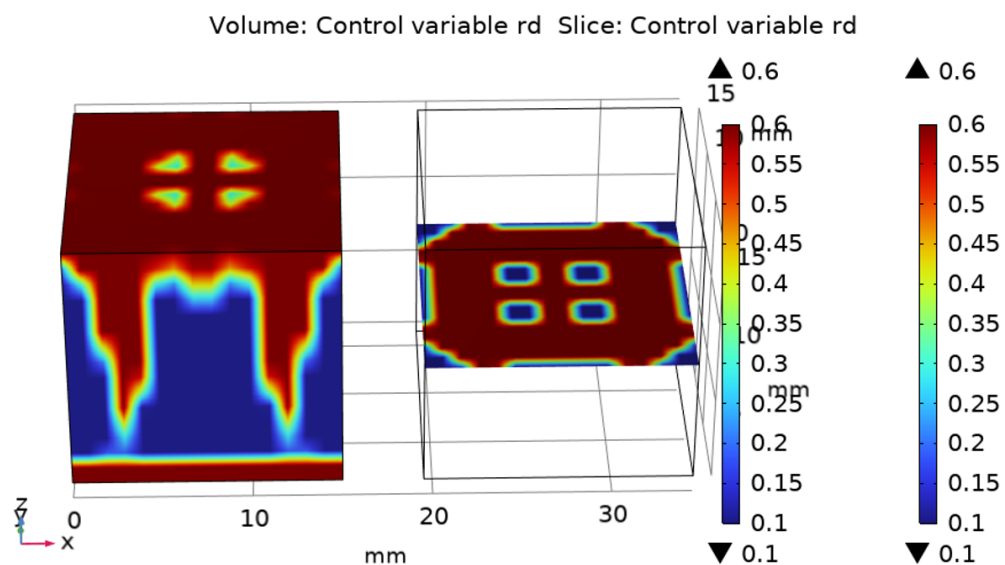


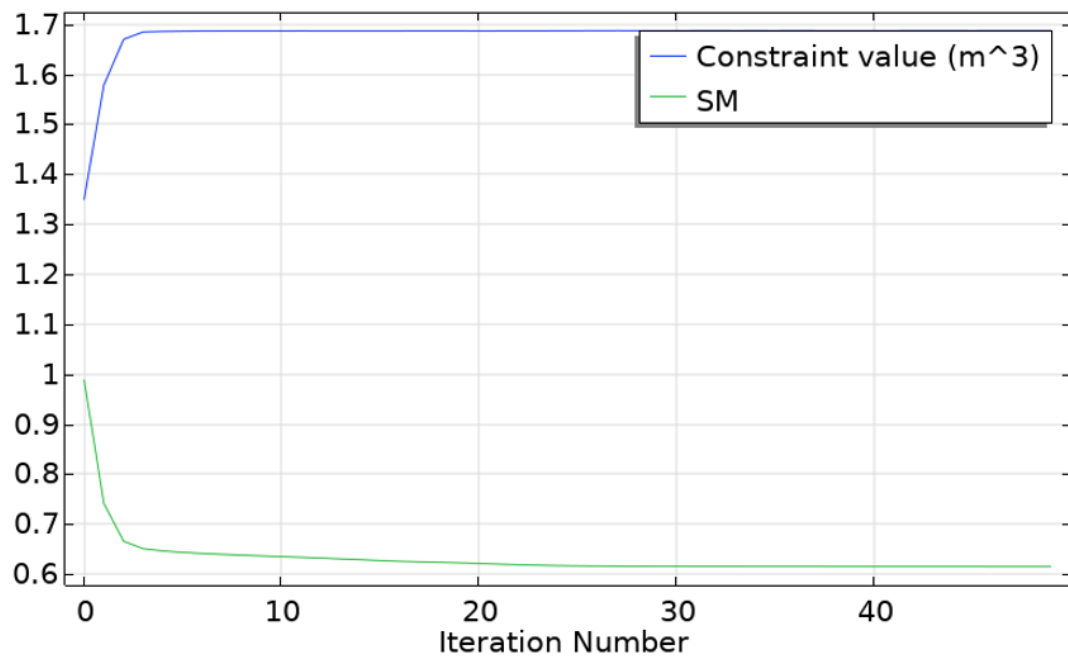
Figure 4.12 Density distribution obtained for the minimization of compliance problem of a compression cube: volumetric distribution (left) vs. cross sectional plot (right)



Although the model doesn't optimize electrical properties, *Electric Currents* physics was enabled in order to examine the effect of the design on piezoresistivity. Since

piezoresistivity is dependent on relative density, a similar mapping of relative density is also observed on change in resistivity. The relative resistivity change for the final geometry without optimizing electrically is 3.96%. This value before optimization when the design space was homogeneously distributed at 0.4 relative density was 4.82%. This means for the case where optimization was pursued based on compliance minimization only, resulting optimal design caused a decrease of its electrical performance. This result is expected since a stiffer structure means less displacement throughout the design space which results in less connection points and pathways for electrical conduction. The simulation model converged at 49 iterations to 0.615 normalized compliance, down from an initial value of 0.98. The simulation took 781 s to converge.

Figure 4.13 Solid based TO case studies 2 and 3 targeting maximum sensitivity: Convergence of objective value (blue), average volume constraint (green).



### 4.3 Electrical Conductivity Based TO Targeting Maximum Sensitivity

All cases presented in this section are divided to the same applied pressure for calculating the final sensitivity of the designed sensors using TO based on the electrical

performance alone without considering any solid mechanics performance metric such as the compliance. It is noted that the a pressure load is still applied and a a multi-physics based FE model is used to solve the pressure sensor design problem via the use of the modified SIMP for the initial conductivity. Accordingly, since the denominators of the sensitivity calculations are the same, only the relative change in resistivity  $\Delta\rho/\rho_0$  is calculated for a one-to-one comparison of the resulting optimized topologies of all three optimization cases solved for. These cases either differ in the objective functions and/or boundary conditions as shown in detail in Table 4.7. More specifically, case 1 is solved with an objective function targeting minimum potential difference, whereas case 2 and case 3 target maximum sensitivity in the form of an equivalent minimization function.

The results show that case 2 and 3 show the best relative change in resistivity (Table. 4.7). Both are implemented using inverse relative change in resistivity definition for the objective function. Their electrical loading, i.e boundary conditions, are different, but the results show that the change of the loading type either in the form of a current density or potential doesn't affect the resulting objective function of the TO problem.

Table 4.7 Properties and results of electrical conductivity based TO cases targeting maximum sensitivity

Case Study No.	Objective Function	Boundary Conditions	$\Delta\rho/\rho_0$
1	Min. $\Phi_{top} - \Phi_{bottom}$	1 $A/m^2$ at top	2.99
2	Min. $\rho/\Delta\rho$	1 $A/m^2$ at top	6.73
3	Min. $\rho/\Delta\rho$	1 $V$ at top	6.73

#### 4.3.1 Case Study 1 With Objective: Minimum Potential Difference

Design results obtained for TO design case 1 are shown in 4.14 with relative density distributions and corresponding effective initial conductivity distributions as well as the performance response distributions attained with the optimized topology such as vertical displacement, potential difference, current density and change in resistivity. The TO model converged to the optimized relative sensitivity of 2.99 following the convergence history shown in (Fig. 4.15). At 25<sup>th</sup> iteration, however, slight unusual oscillations are observed in the objective function value. Also from the resulting topology and the final attained volume fraction of 23%, it can be seen that the

algorithm attempted to empty the design volume as much as possible. Although the final relative change in resistivity is 2.99%, based on the oscillatory convergence graph, if the simulation results are based on iteration 25, then the relative change in resistivity would be 15% which points for future analysis of the optimization model definition and its convergence behavior. However, based on the results of cases 2 and 3 where the objective function produced smoother convergence with larger improvements in sensitivity of the final design, the sensitivity based objective function model was chosen for further TO design studies.

Figure 4.14 Design results obtained for TO design case study 1: relative density (top left), displacement (top center), electrical potential (top right), current density (bottom left), initial conductivity (bottom center), and change in resistivity (bottom right). Units are shown in corresponding colour bars

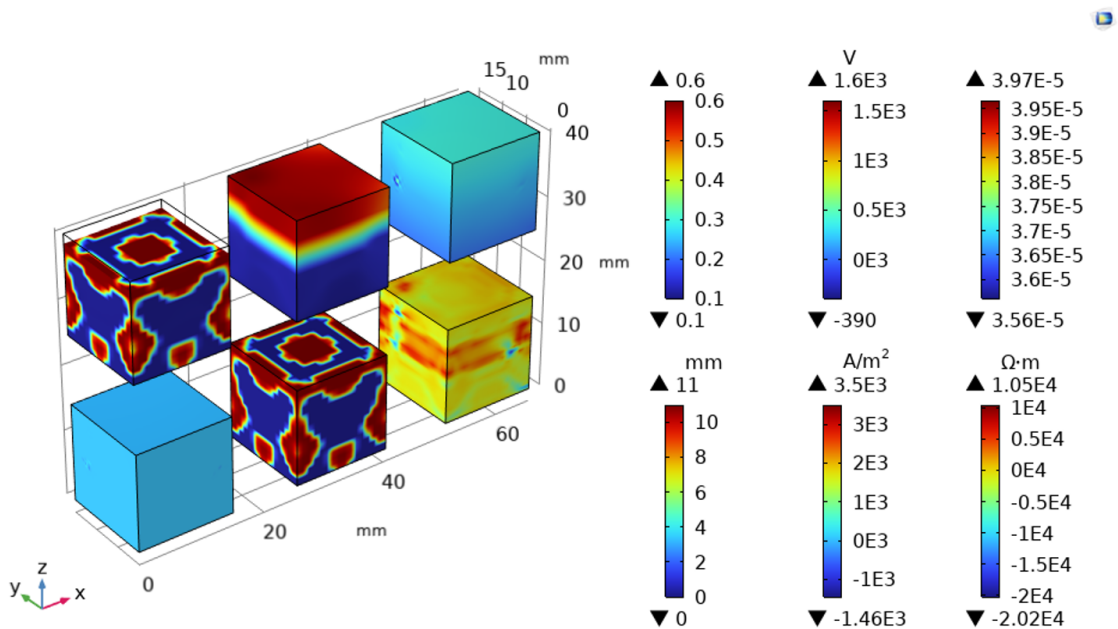
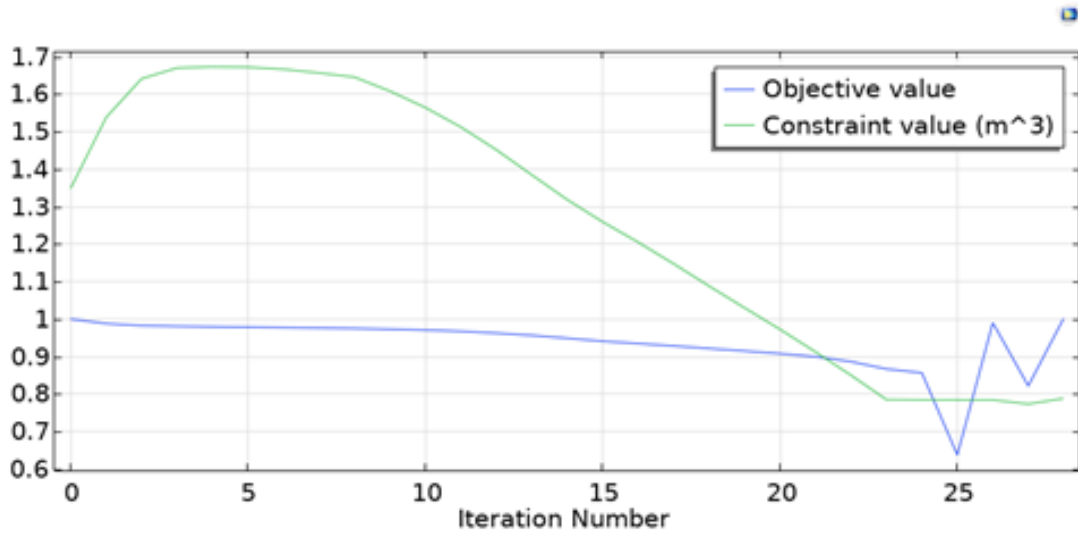


Figure 4.15 Convergence history of objective function and VF constraint of TO case study 1



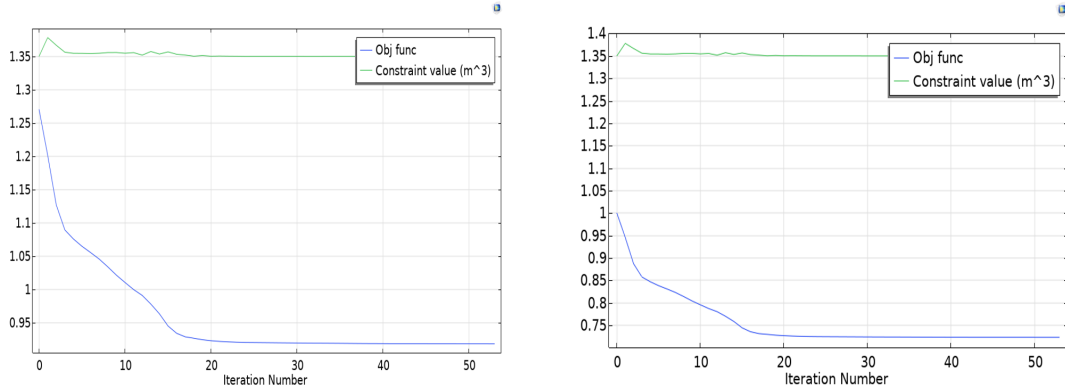
### 4.3.2 Case Study 2 and Case Study 3 with Objective of Relative Resistivity Change - Effect of BC

Design results obtained for TO design case 2 and case 3 are shown in Fig. 4.17, and Fig. 4.19, respectively with relative density distributions and corresponding effective initial conductivity distributions as well as the performance response distributions attained with the optimized topology such as vertical displacement, potential difference, current density and change in resistivity. For a better interpretation of the resulting topologies, cross section views of the resulting topologies are shown for case 2 and case 3 in 4.18, 4.20, respectively.

Convergence history of case 2 and 3 is shown in 4.16, on left and right respectively. The results of the TO studies directly targeting the relative resistivity based norm to increase sensitivity in both cases of case study 2 and case study 3 gave very similar results despite the difference in their electrical loading. Objective functions in both cases decrease steadily and converge at around 20<sup>th</sup> iteration. Both models improve the objective function by 25%. The relative change in resistivity output is 6.73%. This is an improvement of the final sensitivity of the sensor design when compared to the results of case study 1 not only in terms of the resulting resistivity change that was directly considered in the optimization model but also in terms of the strain energy density that was simply evaluated as the resulting mechanical performance of the sensor. More specifically, strain energy density values in case study 2 and

case study 3 are calculated as  $76.41 J/m^3$  while for the resulting topology of case study 1 the resulting strain energy density is calculated as  $1 W_s = 271.92 J/m^3$ .

Figure 4.16 Electrical based TO case studies 2 and 3 targeting maximum sensitivity: Convergence of objective value (blue), average volume constraint (green).



(a) Model 2

(b) Model 3

Based on these results, it can be concluded that change of the electrical input in terms of the relevant boundary condition seem not to affect the resulting solution of the TO problem. Compared with the first case study, the objective function has a more dominant effect. It is also observed that, as would be expected, the resulting optimized topologies targeting maximum sensitivity differ significantly from the minimum compliance TO solution. The resulting material distribution obtained for the conductivity based TO delivering optimal sensitivity is very concentrated at specific regions, where the top is very dense while the bottom is almost completely empty. To investigate the combined effect of both the mechanical and electrical design requirements of a pressure sensor, their combined effect is analyzed in the next case study via a multi-criteria optimization model.

Figure 4.17 Design results obtained for electrical TO design case 2: relative density (top left), displacement (top center), electrical potential (top right), current density (bottom left), initial conductivity (bottom center), and change in resistivity (bottom right). Units are shown in corresponding colour bars

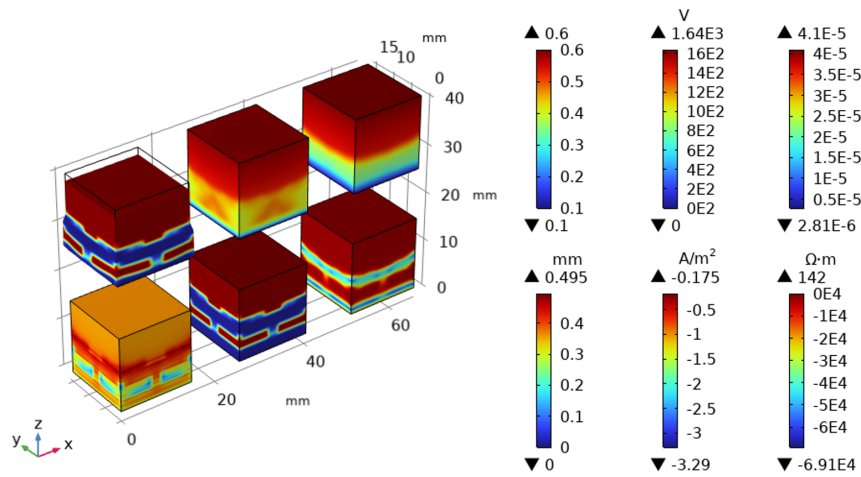


Figure 4.18 Density distribution obtained for the minimization of electrical TO design case 2: volumetric distribution (left) vs. cross sectional plot on xy plane (center) and cross sectional plot on xz plane (right)

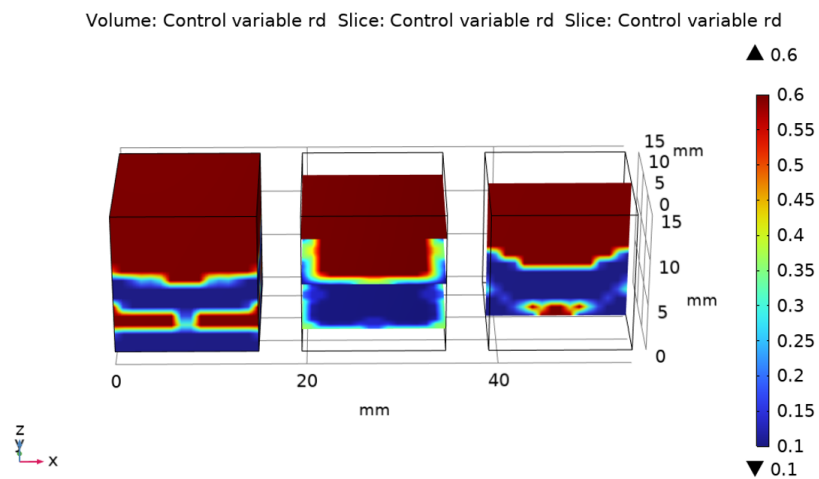


Figure 4.19 Design results obtained for electrical TO design case 3: relative density (top left), displacement (top center), electrical potential (top right), current density (bottom left), initial conductivity (bottom center), and change in resistivity (bottom right). Units are shown in corresponding colour bars.

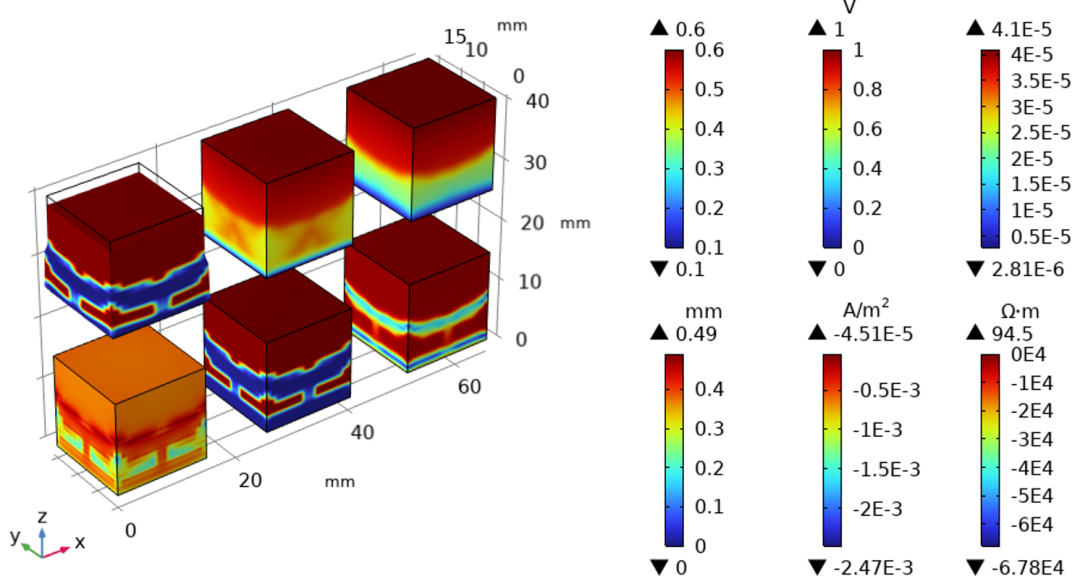
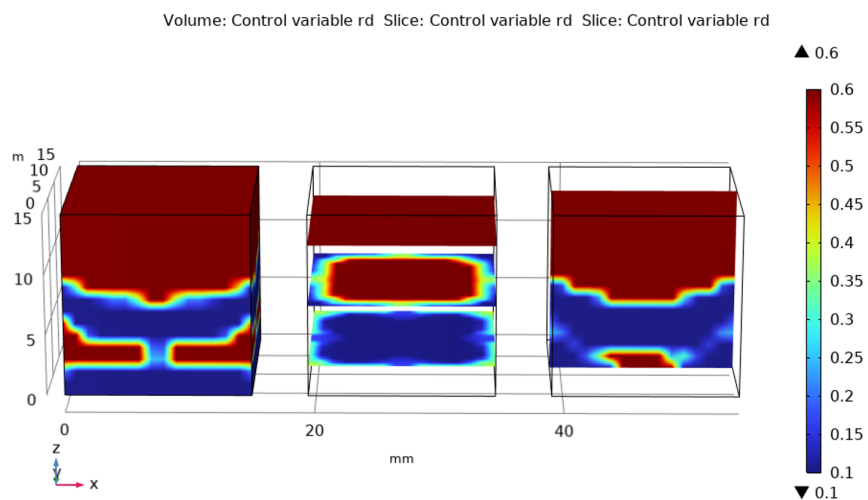


Figure 4.20 Density distribution obtained for the the minimization of electrical TO design case 3: volumetric distribution (left) vs. cross sectional plot on xy plane (center) and cross sectional plot on xz plane (right)



## 4.4 Piezoresistivity Based TO Targeting Maximum Sensitivity and

### Compliance: Multi-Criteria Optimization

In this section two case studies, referred to case study 4 and case study 5 are presented where the TO design approach is applied targeting both maximum sensitivity and minimum compliance simultaneously with optimization model details as given in Table 4.8. The multi-criteria design problem was formulated and solved in all cases with a weighted sum objective incorporating both design objectives into a single weighted objective function (Fig 3.17). Resulting values of both metrics that the case studies converged to are also given. Appendix .2 shows results of different objective functions with different weights for case 5. The presented weight choice for case study 5 is 0.8 weight on the electrical objective function and 0.2 on the mechanical objective function (Fig. 4.23). It is noted that in both case studies, the same objective function for the mechanical compliance is used and therefore was not specified in Table 4.8. Similar to earlier results presented for case study 1-3, where only the electrical performance metric was incorporated as the chosen objective function, here, for the case study 5, with the objective function of sensitivity, the resulting sensitivity was higher than that of case 4 where the objective function was assigned as the minimization of potential difference. However, regarding the strain density values, case study 4 converged to a lower compliance of  $18.88 J/m^3$  when compared to case study 5, which attained a higher value of  $47.048 J/m^3$ .

Table 4.8 Properties and results of PR based TO cases targeting maximum sensitivity and compliance via multi-criteria optimization

Case Study No.	Electrical Objective Function	Boundary Conditions	$\Delta\rho/\rho_0$	Strain Energy Density ( $J/m^3$ )
4	Min. $\Phi_{diff} = \Phi_{top} - \Phi_{bottom}$	1 $A/m^2$ at top	2.3419	18.88
5	Min. $\rho/\Delta\rho$	1 $V$ at top	7.4239	47.048

Design results obtained for TO design case 4 and case 5 are shown in 4.21, 4.23, respectively with relative density distributions and corresponding effective initial conductivity distributions as well as the performance response distributions attained with the optimized topology such as vertical displacement, potential difference, current density and change in resistivity. For a better interpretation of the resulting topologies, cross section views of the resulting topology for case 5 is also shown in Fig. 4.24, respectively.

Convergence history of case 4 is shown in Fig. 4.22 and for case 5, it is shown in Fig. 4.25, respectively.

Based on the optimal density distribution that case study 4 converged to in Fig. 4.21, it is observed that there is a direct similarity with the results of the TO for minimum compliance in Fig. 4.12 where no electrical performance metric was targeted but only standard mechanical TO was repeated for the modified SIMP model developed in this thesis. Therefore, it can be argued that the mechanical component of the multi-criteria TO in case of the potential difference minimization targeted minimization design case 4, the mechanical performance metric of minimum compliance is more dominantly determining the final material distribution of the sensor. This is also supported by comparing the convergence performance of both objective functions in Fig. 4.22 that shows that the potential difference,  $\Phi_{diff}$ , barely decreases over the iterations. On the other hand, the resulting compliance is significantly reduced supporting that the mechanical objective function component of the design study overweighs its electrical objective function .

Figure 4.21 Design results obtained for PR based TO design case 4: relative density (top left), displacement (top center), electrical potential (top right), current density (bottom left), initial conductivity (bottom center), and change in resistivity (bottom right). Units are shown in corresponding colour bars.

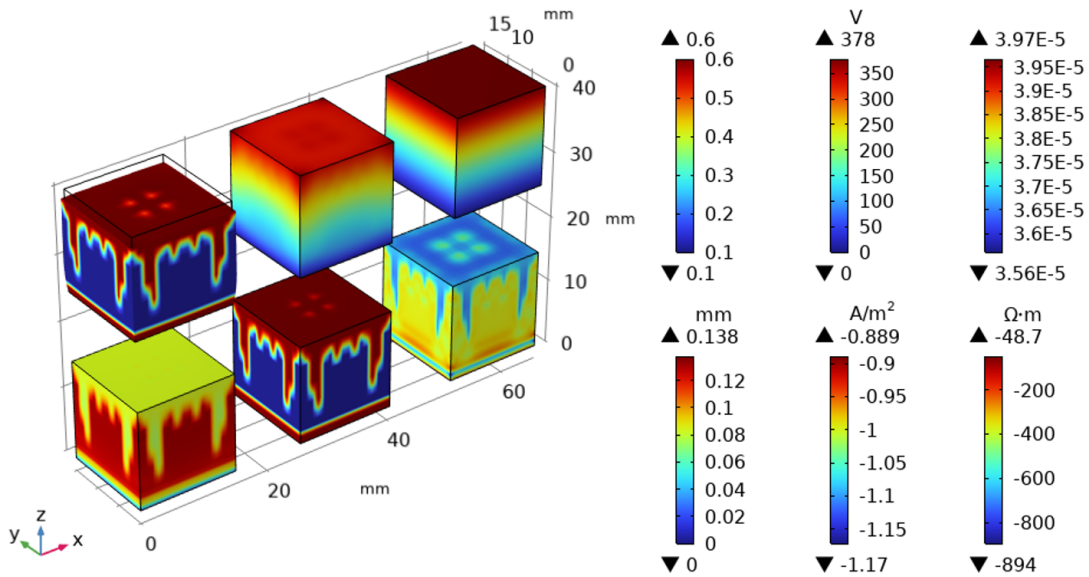
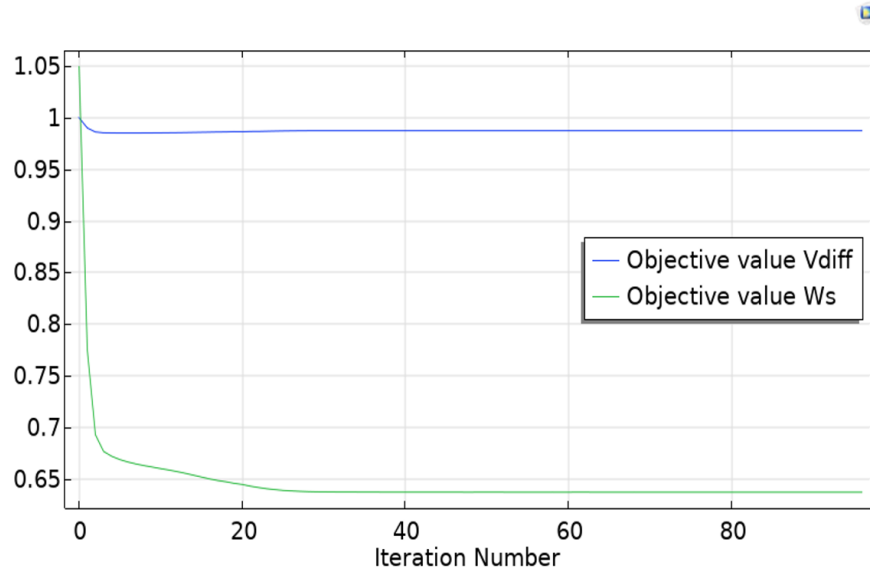
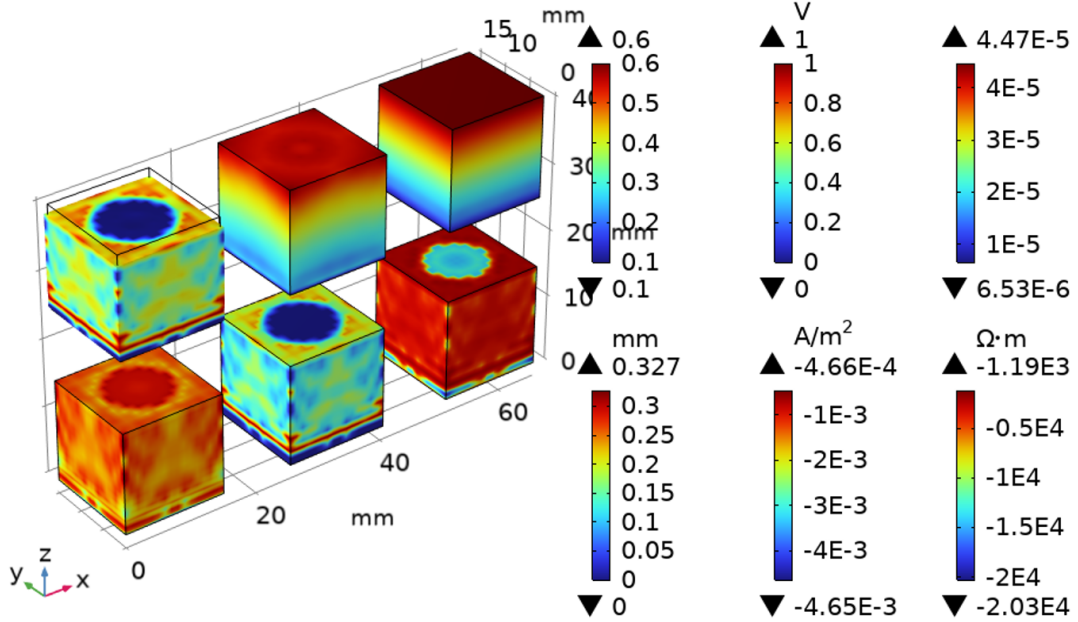


Figure 4.22 PR based TO case number 4 targeting maximum sensitivity and minimum compliance: Convergence of objective value (blue) and average volume constraint (green).



The design case 5 where instead of the potential difference minimization for the electrical design component the maximization of the relative change was targeted, the convergence history graph in (Fig. 4.25) displayed a more balanced scenario with about 13% improvement in the sensitivity starting from 6.61% relative change in resistivity and converging to 7.42% and with a trade of in compliance performance. In terms of the resulting optimal material distribution shown in Fig. 4.24, case 5 converged to a topology with some common characteristics to the results of TO for in Fig. 4.12 where no electrical performance metric was targeted. The resemblance lies in that both topologies demand removal of material in the central part with denser/more solid material on the sides. However, there is no exact similarity to suggest that the optimization process is driven by the mechanical component of the design objectives dominant. When the resulting topology for case 5 is compared to the optimized density distributions obtained for the electrical conductivity TO designs of case 2 or case 3 in Fig. 4.17 and Fig. 4.19, some similarities also exist here where the low-density regions exist closer to the bottom part of the resulting sensor topologies in both cases, namely 5 and 3.

Figure 4.23 Design results obtained for PR based TO design case 5: relative density (top left), displacement (top center), electrical potential (top right), current density (bottom left), initial conductivity (bottom center), and change in resistivity (bottom right). Units are shown in corresponding colour bars.



More specifically, the resulting topology of case 5, resembles a pyramid-like topology apparent as the mid-range/yellow material shades existing throughout the volume, which could be argued to serve for increasing the stiffness of the sensor keeping its structural integrity (Fig. 4.24). Also close to the top and bottom locations of the sensor design, the material density is higher towards the edges in these cross sections. This should result in an uneven distribution of the applied pressure throughout the top and bottom cross-sections with less dense regions at the central regions .

Figure 4.24 Density distribution obtained for PR based TO case number 5 targeting maximum sensitivity and compliance (Case 5): volumetric distribution (left) vs. cross sectional plot on xy plane (center) and cross sectional plot on xz plane (right)

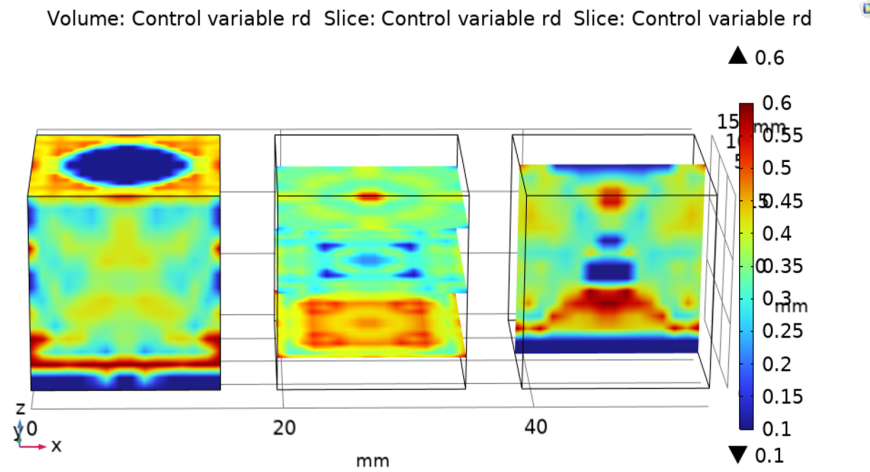
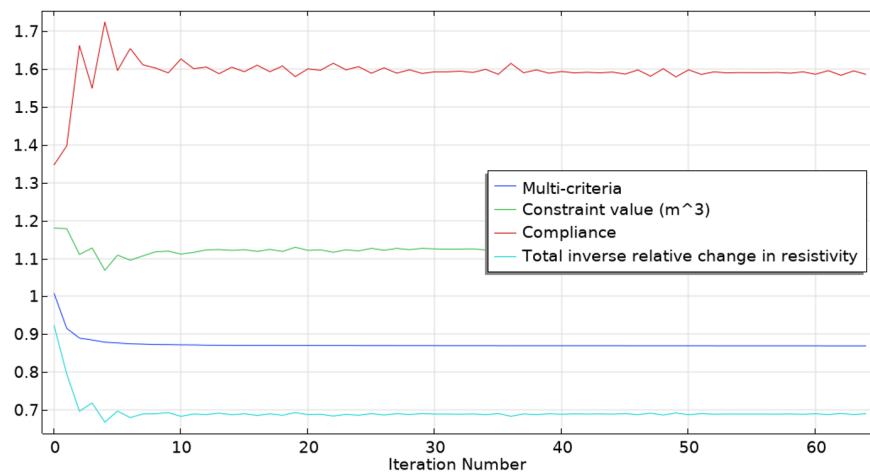


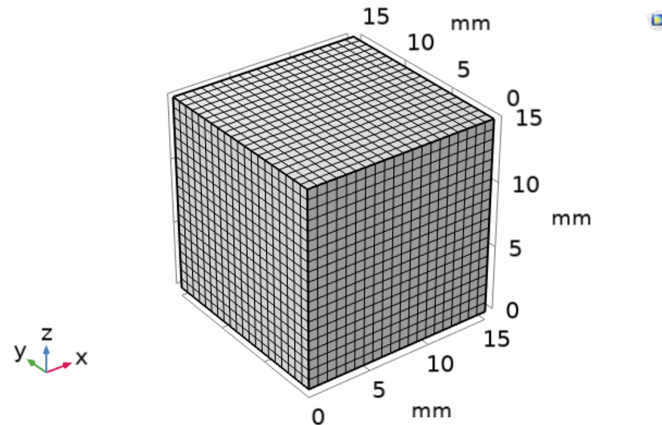
Figure 4.25 PR based TO case number 5 targeting maximum sensitivity and minimum compliance: Convergence of multi-criteria objective value (blue), average volume constraint (green), compliance (red), and Total inverse relative change in resistivity (cyan).



As a follow-up study, the TO design of case study 5 was re-simulated with a higher mesh to examine the mesh effect on the resulting topology and performance improvements of the objective functions. TO of case study 5 FE model relied on a hexahedral mesh with a mesh density of 15 FE/edge length, where the edge length is 15 mm, in all primary directions of the design domain as shown in (Fig. 3.9. The finer meshed follow-up model of case 5 is meshed into 20 FE/edge length FEs constituting 8000 design cells as shown in (Fig. 4.26 of the TO design with the

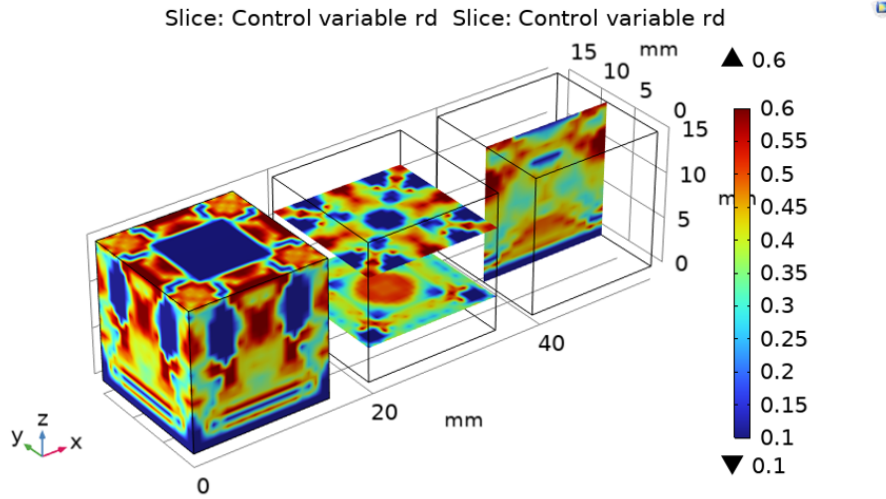
same model properties as shown in Table. 4.7 . Hence, the number of design cells increased from 3375 to to 8000 and the TO was repeated.

Figure 4.26 Denser mesh with 8000 elements



The TO study with the finer mesh follow-up model of case study 5 converged to the material distribution shown in (Fig. 4.27) with  $47.8 J/m^3$  strain energy density and 7.61% inverse relative change in resistivity values. This prompts for a slight improvement of the relative change in resistivity by 2.5% using a finer mesh FE model, however, requiring a longer computational design time until convergence mainly due to increased number of 176084 DOF of the finer mesh vs. the original rough mesh of case study 5 with 76639 DOF. The actual computation time difference was half an hour for the entire design cycle. Although no significant improvement was obtained in terms of the desired relative change in resistivity, certainly the resulting optimal sensor topology displays more intricate structural details in the case of the finer mesh model (Fig. 4.27) when compared to the original case study 5 topology in (Fig. 4.24) .

Figure 4.27 Density distribution obtained for PR based TO case number 5 with a denser mesh targeting maximum sensitivity and compliance (Case 5): volumetric distribution (left) vs. cross sectional plot on xy plane (center) and cross sectional plot on xz plane (right)



## 4.5 Discussion

The results presented in the first part comprise the numerical homogenization of three material properties, namely Young's modulus, initial conductivity and elastoresistivities as well as their validation studies. Overall, for all three material properties, results show an average total error below 10% for majority of relative density values proving that the derived modified SIMP models are suitable to represent effective models for gyroids of different volume fractions with reasonable accuracy.

A common observation for the homogenization analysis were related to the comparative higher error values at the extreme relative density points. Although the fitted functions closely followed simulated data with an average acceptable error, the relative volume fraction of 0.1 point was an outlier for the majority of the homogenization calculations. The lower limit of a very thin gyroid with 0.1 relative density has a comparatively higher error and intuitively is expected as thinner curved structures present a meshing challenge when compared to their thicker, higher volume fraction counterparts. This behavior is also reflected on the validation results of the constructed modified SIMP models. In the case of numerical homogenization, possible errors could be also attributed to the use of a single unit cell and the need

to increase the mesh density of the imported gyroid model when exported as an .stl file from MATLAB. Also, the rule of thumb for TPMS lattice meshing is that there should be at least three elements across the thinnest walls of the gyroid model. This was not always possible for the models simulated in this thesis, and hence a possible source for a higher relative, yet acceptable overall error. Another approximation and possible cause of inaccuracy related to the use of symmetry boundary condition to represent periodic repetition of gyroid unit cells as required by the theory of homogenization. To increase the analysis accuracy further, of higher number of unit cell repetitions with possibly a higher FE mesh is needed but practically limited by the available computational power and prohibitive time spans.

Similar to the thinnest gyroid model with volume fraction of 0.1, 0.7 represents the thickest gyroid which geometrically is the limiting point where the surfaces start to close-up due to too thick walls of the lattice geometry. Hence, higher relative errors observed are related to the representation challenge of too thin as well as thick gyroids.

Results of the second part of this chapter proved the applicability of the developed homogenization based TO design scheme to various design case studies targeting either only the solid mechanics related or the electrical performance of a sensor or both at the same time. The first case study results prove the applicability of the developed design scheme to a minimum compliance TO benchmark problem delivering a similar four-legged optimal topology with reduction in compliance. The second class of designs where different objective functions and boundary loading conditions are tested, namely case studies 1-3, present that inverse relative change in resistivity proves to be a more suitable objective function for sensitivity maximization when compared to the minimization of potential difference. Combined with the results of the last category of TO case studies, where mechanical compliance and sensor sensitivity metrics are targeted at the same time, case study 5 with a weighted sum of these aforementioned objective functions delivered the highest overall improvement with a relative change in resistivity of 7.42 %. Since the same pressure was applied to all models, this model also gives the best sensitivity. It can be overall stated, that the developed topology optimization framework based on modified SIMP models of Young's modulus and elastoresistivity for gyroid unit cells has the ability to improve sensitivity of a piezoresistive sensor.

## 5. CONCLUSION AND FUTURE WORK

In this study, we aimed to fill a gap in literature of FEM based topology optimization of 3D piezoresistive sensors, in particular relying on graded TPMS lattices, to maximize sensitivity. For this purpose, a topology optimization framework based on homogenization of Young's modulus, initial conductivity and elastoresistivity was developed. The sensor was designed to reach max sensitivity at 4666 Pa as it was planned to be useful for pressure ulcer detection targeting bedsores prevention. Gyroid unit cell's Young's modulus, initial conductivity and elastoresistivity material properties were homogenized and integrated to the topology optimization framework as modified SIMP material models. The simulation framework was applied to different classes of optimization problems initially focusing on the mechanical and electrical optimization studies separately and then presenting integrated design studies with simultaneous consideration of both performance metrics in a multi-criteria optimization setting. Under these categories, studies were presented for different objective functions and compared within the electrical response based and multi-criteria based TO groups. Results showed that maximum improvement was achieved using a PR based multi-criteria TO with a weighted sum incorporating both maximum sensitivity and minimum compliance design requirements. Based on the results it can be stated that the sensitivity improvement of a piezoresistive sensor can be achieved with the developed topology optimization based on gyroid based homogenization.

Improvement of the presented design framework include the addition of the reconstruction and validation phase of the presented final optimization results. After a possible virtual validation comparing the compliance and sensitivity of the optimized TO presented here with the performance of the reconstructed gyroid counterparts, these models could be fabricated using the lost mold technique and tested. The feasibility of manufacturing TPMS based sensors was tested in our research group experimentally (Erulker et al., 2022) for which the basis steps are provided in Fig. 2.3 and could be followed. Main future work regarding the design framework comprises integration of anisotropic material models of the material matrices, extension

of the material models to non-linear elastic behavior and addition of other desired metrics such as flexibility as well as the incorporation of an empirical elastoresistivity material model.

## BIBLIOGRAPHY

- Al-Ketan, O., Lee, D.-W., Rowshan, R., & Abu Al-Rub, R. K. (2020). Functionally graded and multi-morphology sheet tpms lattices: Design, manufacturing, and mechanical properties. *Journal of the Mechanical Behavior of Biomedical Materials*, *102*, 103520.
- Babuška, I. (1976). Homogenization and its application. mathematical and computational problems. In B. HUBBARD (Ed.), *Numerical Solution of Partial Differential Equations–III* (pp. 89–116). Academic Press.
- Bendsøe, M. P. & Kikuchi, N. (1988). Generating optimal topologies in structural design using a homogenization method. *Comput Methods Appl Mech Eng*, *71*, 197–224.
- Bendsøe, M. P. & Sigmund, O. (2003). *Topology optimization: Theory, methods and applications*. Berlin: Springer-Verlag.
- Bensoussan, A., Lions, J., & Papanicolaou, G. (2011). *Asymptotic analysis for periodic structures*. Providence, RI: American Mathematical Society.
- Chatzigeorgiou, C., Piotrowski, B., Chemisky, Y., Laheurte, P., & Meraghni, F. (2022). Numerical investigation of the effective mechanical properties and local stress distributions of tpms-based and strut-based lattices for biomedical applications. *Journal of the Mechanical Behavior of Biomedical Materials*, *126*, 105025.
- Chen, S., Zhu, M. Q., Ma, B. H., & Yuan, W. Z. (2008). Design and optimization of a micro piezoresistive pressure sensor.
- Cui, X., Huang, F., Zhang, X., Song, P., Zheng, H., Chevali, V., Wang, H., & Xu, Z. (2022). Flexible pressure sensors via engineering microstructures for wearable human-machine interaction and health monitoring applications. *iScience*, *25*(4), 104148.
- Das, S. & Sutradhar, A. (2020). Multi-physics topology optimization of functionally graded controllable porous structures: Application to heat dissipating problems. *Materials and Design*, *193*, 108775.
- Davoodi, E., Montazerian, H., Haghniaz, R., Rashidi, A., Ahadian, S., Sheikhi, A., Chen, J., Khademhosseini, A., Milani, A. S., Hoorfar, M., & Toyserkani, E. (2020). 3D-Printed Ultra-Robust Surface-Doped Porous Silicone Sensors for Wearable Biomonitoring. *ACS Nano*, *14*(2), 1520–1532.
- Definition, M. (2013). Piezoresistive Pressure Sensor , Shell.
- Duan, L., D’hooge, D. R., & Cardon, L. (2020). Recent progress on flexible and stretchable piezoresistive strain sensors: From design to application. *Progress in Materials Science*, *114* (January 2018), 100617.
- Erulker, E. N., Ece, T., Ekicioglu, A., Can, F., Kiziltas Sendur, G., & Ince, G. (2022). Simulation based design and fabrication of a ppy coated pdms based pressure sensor. Paper presented at the NANO-TR 16.
- Feng, J., Fu, J., Yao, X., & He, Y. (2022). Triply periodic minimal surface (TPMS) porous structures: From multi-scale design, precise additive manufacturing to multidisciplinary applications. *International Journal of Extreme Manufacturing*, *4*(2).
- Gibson, L. & Ashby, M. (1997). *Cellular Solids: Structure and Properties* (2 ed.).

- Cambridge: Cambridge University Press.
- Giusti, S. M., Mello, L. A., & Silva, E. C. (2014). Piezoresistive device optimization using topological derivative concepts. *Structural and Multidisciplinary Optimization*, *50*(3), 453–464.
- Gridchin, A. V. & Gridchin, V. A. (1997). The four-terminal piezotransducer: Theory and comparison with piezoresistive bridge. *Sensors and Actuators, A: Physical*, *58*(3), 219–223.
- Guo, X., Zhang, W., & Zhong, W. (2014). Doing Topology Optimization Explicitly and Geometrically—A New Moving Morphable Components Based Framework. *Journal of Applied Mechanics*, *81*(8), 081009.
- Hassani, B. & Hinton, E. (1998). A review of homogenization and topology optimization i—homogenization theory for media with periodic structure. *Computers & Structures*, *69*, 707–717.
- Imanian, M. E., Kardan-Halvaei, M., Nasrollahi, F., Imanian, A., Montazerian, H., & Nasrollahi, V. (2023). 3D printed flexible wearable sensors based on triply periodic minimal surface structures for biomonitoring applications. *Smart Materials and Structures*, *32*(1).
- Kalantari, M., Dargahi, J., Kövecses, J., Mardasi, M. G., & Nouri, S. (2012). A new approach for modeling piezoresistive force sensors based on semiconductive polymer composites. *IEEE/ASME Transactions on Mechatronics*, *17*(3), 572–581.
- Khalili, N., Shen, X., & Naguib, H. E. (2018). An interlocked flexible piezoresistive sensor with 3D micropyramidal structures for electronic skin applications. *Soft Matter*, *14*(33), 6912–6920.
- Li, D., Dai, N., Tang, Y., Dong, G., & Zhao, Y. F. (2019). Design and Optimization of Graded Cellular Structures with Triply Periodic Level Surface-Based Topological Shapes. *Journal of Mechanical Design*, *141*(7).
- Lu, Y., Zhao, W., Cui, Z., Zhu, H., & Wu, C. (2019). The anisotropic elastic behavior of the widely-used triply-periodic minimal surface based scaffolds. *Journal of the Mechanical Behavior of Biomedical Materials*, *99*, 56–65.
- Maskery, I., Aremu, A. O., Parry, L., Wildman, R. D., Tuck, C. J., & Ashcroft, I. A. (2018). Effective design and simulation of surface-based lattice structures featuring volume fraction and cell type grading. *Materials and Design*, *155*, 220–232.
- Mello, L. A., Takezawa, A., & Silva, E. C. (2012). Designing piezoresistive plate-based sensors with distribution of piezoresistive material using topology optimization. *Smart Materials and Structures*, *21*(8).
- Misaki, A., Imanishi, K., Takasugi, S. I., Wada, M., Fukagawa, S., & Furue, M. (2014). Body pressure sensing mattress for bedsore prevention. *SEI Technical Review*, (78), 95–99.
- Mitrakos, V. (2014). *Design , Development and Characterisation of Piezoresistive and Capacitive Polymeric Pressure Sensors for use in Compression Hosiery*. PhD thesis, Heriot-Watt University School.
- Modrek, M., Viswanath, A., Khan, K. A., Hassan Ali, M. I., & Abu Al-Rub, R. K. (2023). Multi-objective topology optimization of passive heat sinks including self-weight based on triply periodic minimal surface lattices. *Case Studies in Thermal Engineering*, *42*(December 2022), 102684.
- Moučka, R., Sedláčik, M., Osička, J., & Pata, V. (2021). Mechanical properties of

- bulk Sylgard 184 and its extension with silicone oil. *Scientific Reports*, 11(1), 1–9.
- Newman, T. S. & Yi, H. (2006). A survey of the marching cubes algorithm. *Computers & Graphics*, 30(5), 854–879.
- Oh, J., Kim, J. O., Kim, Y., Choi, H. B., Yang, J. C., Lee, S., Pyatykh, M., Kim, J., Sim, J. Y., & Park, S. (2019). Highly Uniform and Low Hysteresis Piezoresistive Pressure Sensors Based on Chemical Grafting of Polypyrrole on Elastomer Template with Uniform Pore Size. *Small*, 15(33), 1–8.
- Ozdilek, E. E., Ozcakar, E., Muhtaroglu, N., Simsek, U., Gulcan, O., & Sendur, G. K. (2024). A finite element based homogenization code in python: HomPy. *Advances in Engineering Software*, 194.
- Panesar, A., Abdi, M., Hickman, D., & Ashcroft, I. (2018). Strategies for functionally graded lattice structures derived using topology optimisation for additive manufacturing. *Additive Manufacturing*, 19, 81–94.
- Pedersen, N. L. (2004). On optimization of bio-probes. *International Journal for Numerical Methods in Engineering*, 61(6), 791–806.
- Rasiya, G., Shukla, A., & Saran, K. (2020). Additive Manufacturing-A Review. *Materials Today: Proceedings*, 47, 6896–6901.
- Rubio, W. M., Silva, E. C., & Nishiwaki, S. (2008). Piezoresistive sensor design using topology optimization. *Structural and Multidisciplinary Optimization*, 36(6), 571–583.
- Saadlaoui, Y., Milan, J. L., Rossi, J. M., & Chabrand, P. (2017). Topology optimization and additive manufacturing: Comparison of conception methods using industrial codes. *Journal of Manufacturing Systems*, 43, 178–186.
- Seesaard, T. & Wongchoosuk, C. (2023). Flexible and Stretchable Pressure Sensors: From Basic Principles to State-of-the-Art Applications. *Micromachines*, 14(8), 1–35.
- Sigmund, O. (1994). Materials with prescribed constitutive parameters: an inverse homogenization problem. *International Journal of Solids and Structures*, 31, 2313–2329.
- Simsek, U., Gayir, C. E., Kiziltas, G., & Sendur, P. (2020). An integrated homogenization-based topology optimization via RBF mapping strategies for additively manufactured FGLS and its application to bandgap structures. *International Journal of Advanced Manufacturing Technology*, 111(5-6), 1361–1374.
- Sixt, J., Davoodi, E., Salehian, A., & Toyserkani, E. (2023). Characterization and optimization of 3D-printed, flexible vibration strain sensors with triply periodic minimal surfaces. *Additive Manufacturing*, 61(November 2022), 103274.
- Stolpe, M. & Svanberg, K. (2001). An alternative interpolation scheme for minimum compliance topology optimization. *Structural and Multidisciplinary Optimization*, 22, 116–124.
- Takezawa, A., Nishiwaki, S., & Kitamura, M. (2010). Shape and topology optimization based on the phase field method and sensitivity analysis. *J Comput Phys*, 229, 2697–2718.
- Tang, R., Lu, F., Liu, L., Yan, Y., Du, Q., Zhang, B., Zhou, T., & Fu, H. (2021). Flexible pressure sensors with microstructures. *Nano Select*, 2(10), 1874–1901.
- Wang, K., Cai, M., Zhou, P., & Hu, G. (2021). Homogenization in a simpler way: analysis and optimization of periodic unit cells with cauchy-born hypothesis.

- Structural and Multidisciplinary Optimization*, 64, 3911–3935.
- Wang, M. Y., Wang, X., & Guo, D. (2003). A level set method for structural topology optimization. *Comput Methods Appl Mech Eng*, 192, 227–246.
- Wymysłowski, A., Santo-Zarnik, M., Friedel, K., & Belavič, D. (2004). Numerical simulation and experimental verification of the piezoresistivity phenomenon for the printed thick-film piezoresistors.
- Xia, L., Xia, Q., Huang, X., & Xie, Y. (2018). Bi-directional evolutionary structural optimization on advanced structures and materials: a comprehensive review. *Archives of Computational Methods In Engineering*, 25, 437–478.
- Xie, Y. M. & Steven, G. P. (1993). A simple evolutionary procedure for structural optimization. *Comput Struct*, 49, 885–969.
- Yamada, T., Hayamizu, Y., Yamamoto, Y., Yomogida, Y., Izadi-Najafabadi, A., Futaba, D. N., & Hata, K. (2011). A stretchable carbon nanotube strain sensor for human-motion detection. *Nature Nanotechnology*, 6(5), 296–301.
- Ye, X. C., Lin, X. C., Xiong, J. Y., Wu, H. H., Zhao, G. W., & Fang, D. (2019). Electrical properties of 3D printed graphite cellular lattice structures with triply periodic minimal surface architectures. *Materials Research Express*, 6(12).
- Zang, Y., Zhang, F., Di, C. A., & Zhu, D. (2015). Advances of flexible pressure sensors toward artificial intelligence and health care applications. *Materials Horizons*, 2(2), 140–156.
- Zhang, Y., Han, F., Hu, Y., Xiong, Y., Gu, H., Zhang, G., Zhu, P., Sun, R., & Wong, C. P. (2020). Flexible and Highly Sensitive Pressure Sensors with Surface Discrete Microdomes Made from Self-Assembled Polymer Microspheres Array. *Macromolecular Chemistry and Physics*, 221(11).
- Zhou, M. & Rozvany, G. I. N. (1991). The coc algorithm, part ii: Topological, geometrical and generalized shape optimization. *Comput Methods Appl Mech Eng*, 89, 309–336.
- Zhuang, C., Minami, K., Shiba, K., & Yoshikawa, G. (2023). Topology optimization for piezoresistive nanomechanical surface stress sensors in anisotropic  $\langle 111 \rangle$  orientations. *Nano Express*, 4(3).

# APPENDICES

## .1. Gyroid Implementation in COMSOL

In this section numerical implementation of homogenization will be shown with screenshots from COMSOL Multiphysics 6.2.

Figure .1.1 Creating the CAD file in MATLAB in .STL format

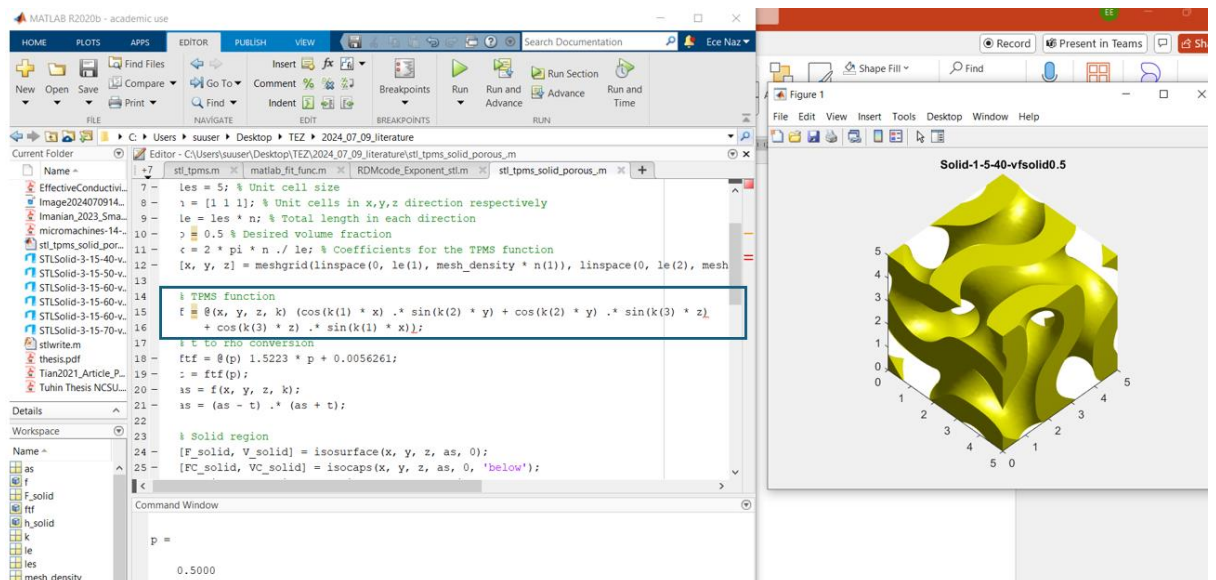


Figure .1.2 Importing the STL file to COMSOL form Mesh Parts

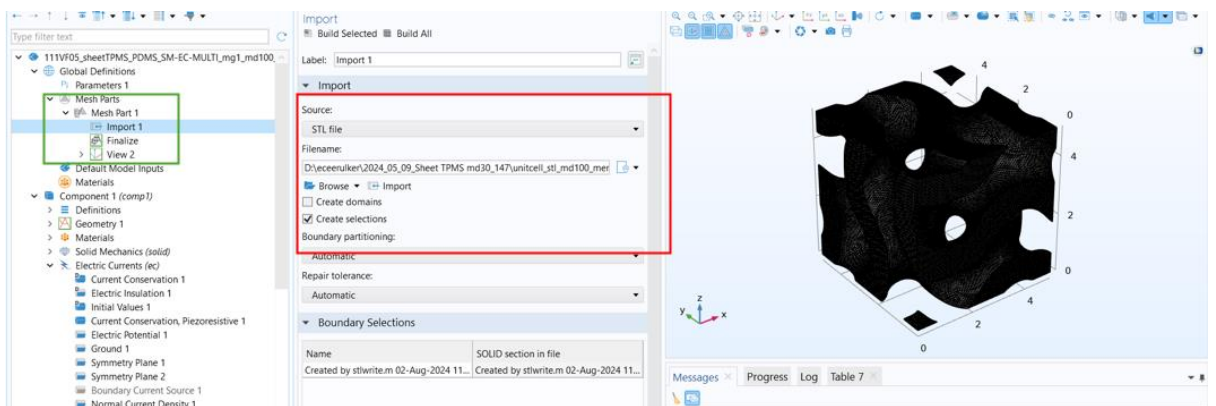


Figure .1.3 Importing geometry under Geomety tab of Component and build

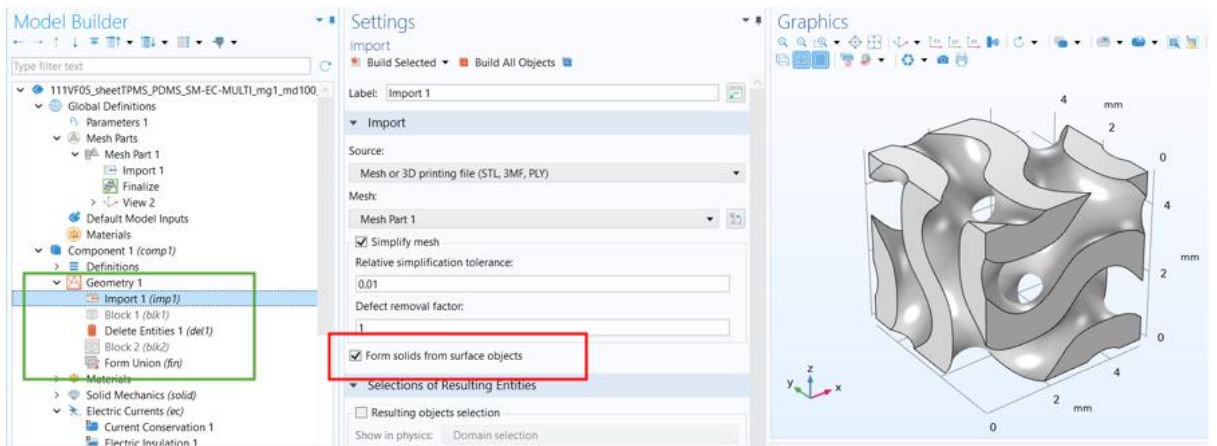


Figure .1.4 Defining the values to be extracted

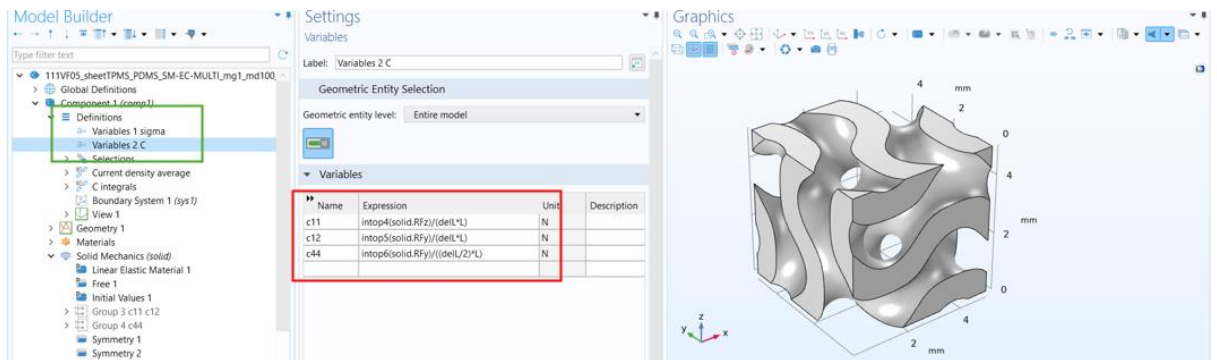


Figure .1.5 Defining governing physics and boundary conditions

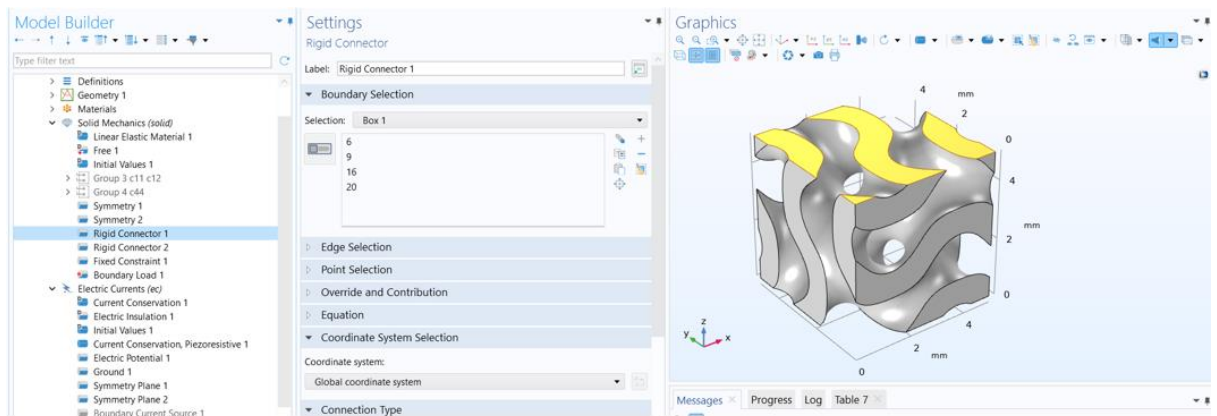


Figure .1.6 Tetrahedral meshing the geometry

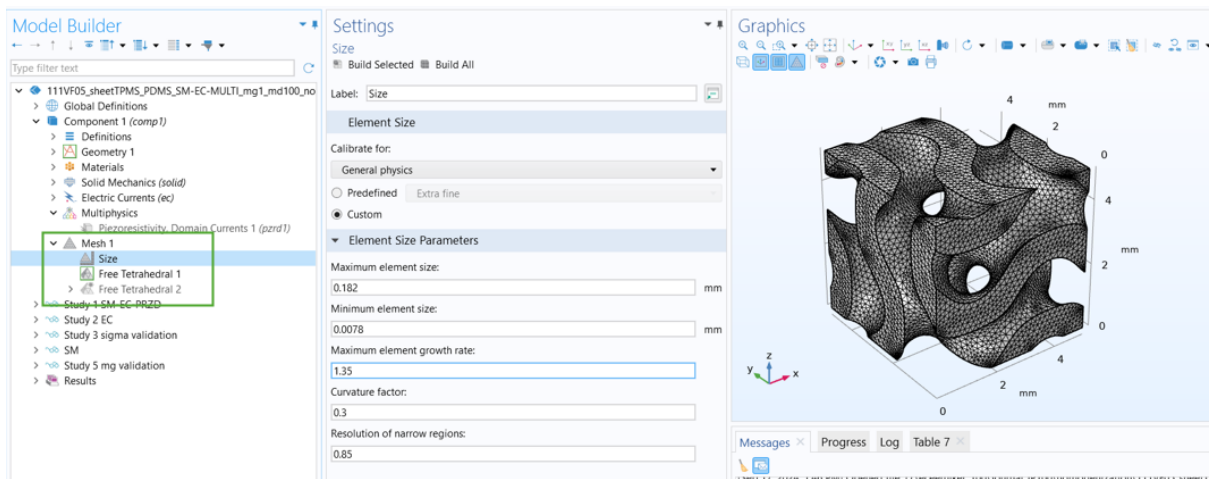
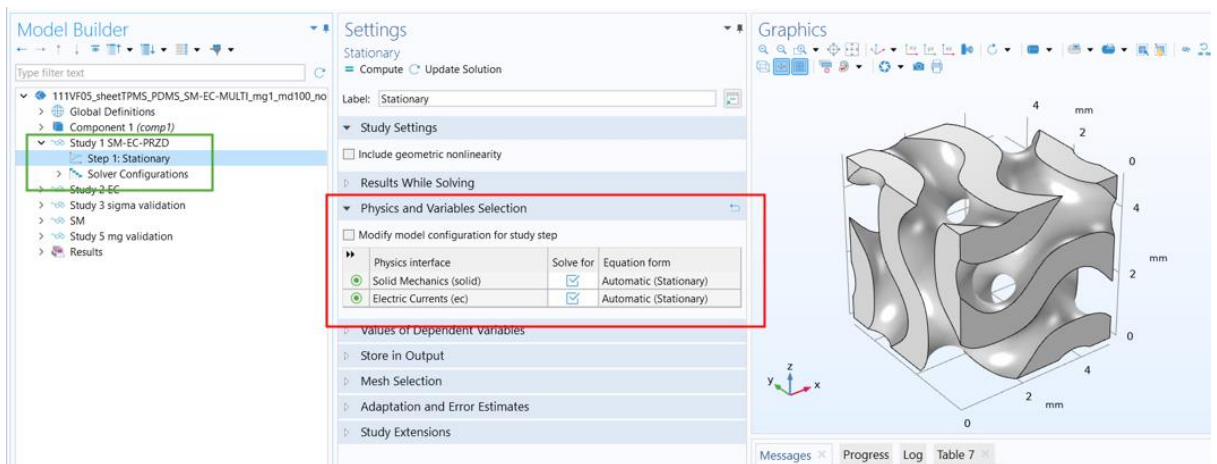


Figure .1.7 Enabling the active physics and running the study



## .2 Comparison of Multi-Criteria Functions with Different Weights

Figure .2.1 0.5 weight on electrical and 0.5 weight on mechanical objective function

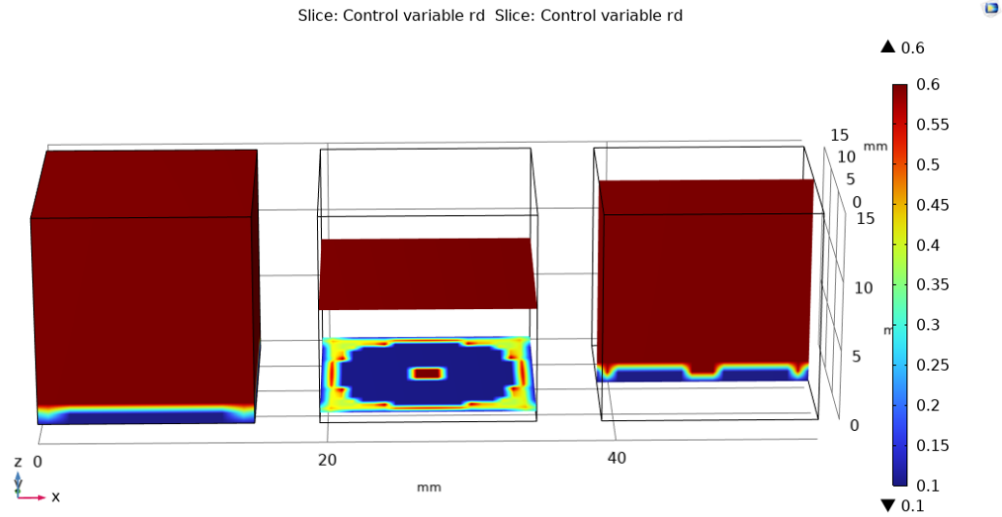


Figure .2.2 0.6 weight on electrical and 0.4 weight on mechanical objective function

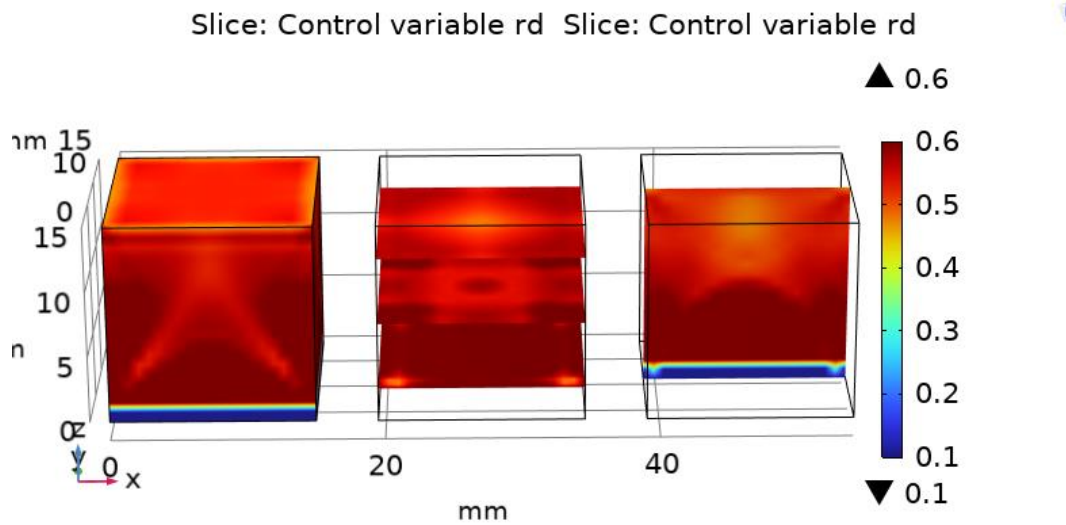


Table .2.1 Optimization with respect to electrical objective function

Model No.	Min. $\rho/\Delta\rho$	$U^T KU$	$\Delta\rho/\rho_0(\%)$
1	0.5	0.5	4.618
2	0.6	0.4	4.890
3	0.8	0.2	7.420

### .3 Simulation Statistis

Table .3.1 Simulation statistics for 1x1x1 sheet gyroid

VF	Repeated UC number	Mesh density (Matlab)	Mesh vertices	DOF	condition no. average element quality
0.1	1	100	25866	190654	0.87
0.2	1	100	46922	338495	0.84
0.3	1	100	70260	524746	0.83
0.4	1	100	90314	703104	0.84
0.5	1	100	36356	807712	0.84
0.6	1	100	77485	402846	0.83
0.7	1	100	27417	182495	0.83
1	1	-	67981	1693407	0.83

Table .3.2 Simulation statistics for 3x3x3 sheet gyroid

VF	Repeated UC number	Mesh density (Matlab)	Mesh vertices	DOF	condition no. average element quality	Computation time (s)
0.1	3	60	182679	3294463	0.86	96
0.2	3	70	80021	1523725	0.82	163
0.3	3	60	21238	386458	0.66	11
0.4	3	90	110270	2253946	0.84	343
0.5	3	60	148668	3119533	0.83	317
0.6	3	60	115183	2400631	0.83	226
0.7	3	60	122559	2511316	0.82	291
1	3	-	7220	83284	0.99	8

## .4 COMSOL Implementation of Material Properties and How They Relate to the Physics Interface

Screenshots from COMSOL Multiphysics ver. 6.2 are given showing the implementation of modified material properties.

Figure .4.1 Linearelastic Material definition in COMSOL

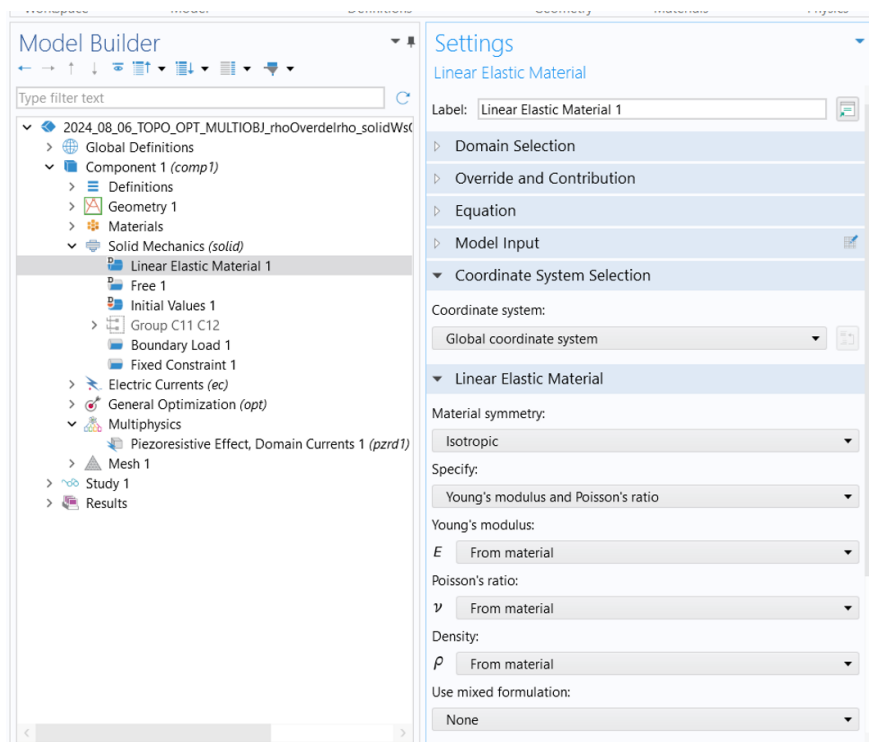


Fig .4.2 Current Conservations, Piezoresistive definition in COMSOL

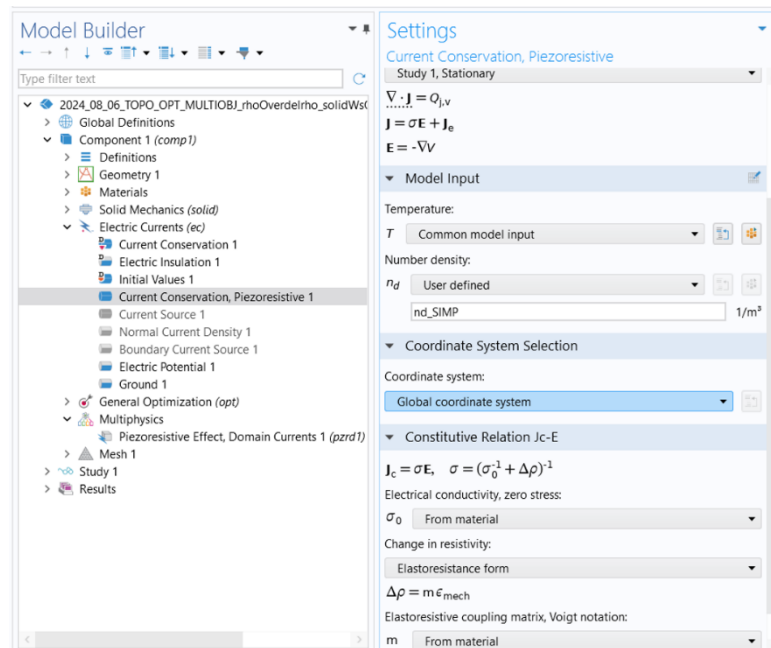


Figure .4.3 Material Properties in COMSOL which are referred in physics modules in Fig. .4.1 and Fig. .4.2

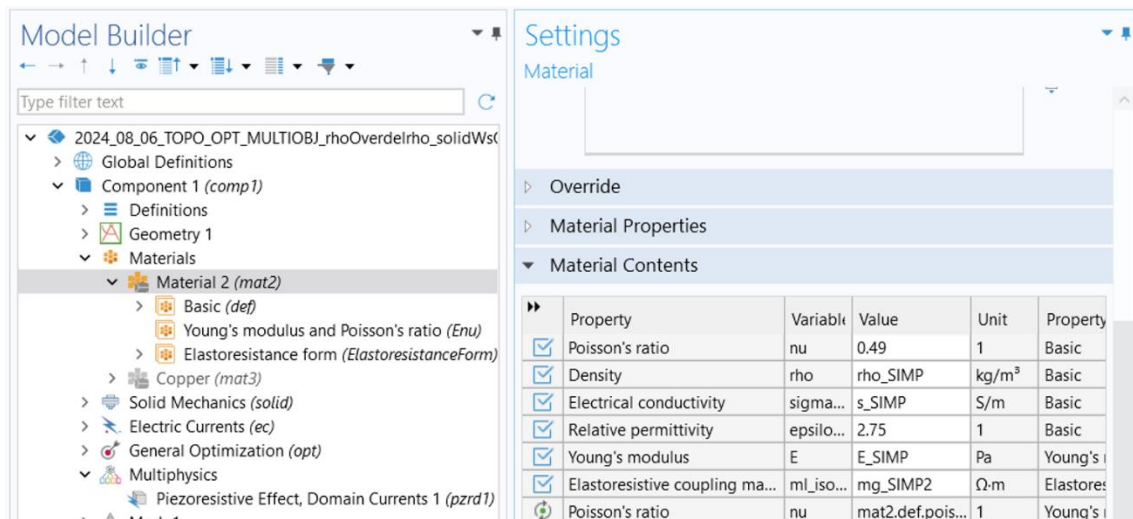


Figure .4.4 Variables in COMSOL: Modified SIMP Formulas

The screenshot shows the COMSOL Multiphysics interface. On the left is the 'Model Builder' tree, and on the right is the 'Settings' window for a variable named 'SIMP'.

**Model Builder Tree:**

- 2024\_08\_06\_TOPO\_OPT\_MULTIOBJ\_rhoOverdelrho\_solid
  - Global Definitions
  - Component 1 (comp1)
    - Definitions
      - Variables 1
        - SIMP
    - Selections
      - Global Variable Probe 1 (var1)
      - Global Variable Probe 2 (var2)
      - Global Variable Probe 3 (var3)
      - Global Variable Probe 4 (var4)
      - Global Variable Probe 5 (var5)
    - Current Density Average
      - Average 4 (aveop4)
    - Boundary System 1 (sys1)
    - View 1
    - Geometry 1

**Settings - Variables:**

Label: SIMP

Geometric Entity Selection

Geometric entity level: Entire model

Name	Expression	Unit	Description
E_SIMP	$2[\text{MPa}] \cdot a_{YM} \cdot rd^{n_{YM}}$	Pa	penalized Youngs mod
s_SIMP	$1E-4 \cdot (a_{ec} \cdot rd^{n_{ec}})$		penalized sigma
rho_SIMP	$980[\text{kg}/\text{m}^3] \cdot rd$	$\text{kg}/\text{m}^3$	
mg_SIMP2	$9.60E+04 \cdot (a_{mg} \cdot rd^{n_{mg}})$		penalized mg
nd_SIMP	$1.3021e+16 \cdot a_{ec} \cdot rd^{n_{ec}}$		penalized numebr density